



NTNU – Trondheim
Norwegian University of
Science and Technology

Modeling of a centrifugal separator for dispersed gas-liquid flows

Gisle Otto Tviberg Monsen

Master of Science in Product Design and Manufacturing

Submission date: June 2012

Supervisor: Maria Fernandino, EPT

Co-supervisor: Carlos Alberto Dorao, EPT

Norwegian University of Science and Technology
Department of Energy and Process Engineering

EPT-M-2012-65

MASTER THESIS

for

Gisle Otto Tviberg Monsen

Spring 2012

Modeling of a centrifugal separator for dispersed gas-liquid flows*Modellering av en sentrifugal separator for dispergerte gass-væske strømninger***Background and objective**

Gas-liquid separation is one of the fundamental steps in the treatment of natural gas. Traditional technologies include vane packs, wire mesh demisters and cyclones. At the same time, there are new emerging technologies that are based on different concepts.

A new separation technology has been developed at the Department of Energy and Process Engineering, NTNU, which combines the best properties of mist eliminators and cyclones and at the same time eliminates the drawbacks of these two.

The goal of this project is to do a basic one-dimensional model of the separator, focusing on the pressure drop and separation efficiency for different design and operating parameters.

The following tasks are to be considered:

1. Literature review on existing traditional and newly developed technologies for gas-liquid separation. Discussion of the applicability and limitations of the new technologies whenever possible.
2. Overview of existing models describing annular flow, pressure drop in porous media and droplet separation in centrifugal fields.
3. One-dimensional model of the centrifugal separator, taking into account the annular flow and the centrifugal regions.
4. Based on the proposed model, analyse pressure loss and separation performance of the separator for different design parameters and operating conditions. Perform a parametric study of the sensitivity of the model for the different parameters involved.

Within 14 days of receiving the written text on the master thesis, the candidate shall submit a research plan for his project to the department.

When the thesis is evaluated, emphasis is put on processing of the results, and that they are presented in tabular and/or graphic form in a clear manner, and that they are analyzed carefully.

The thesis should be formulated as a research report with summary both in English and Norwegian, conclusion, literature references, table of contents etc. During the preparation of the text, the candidate should make an effort to produce a well-structured and easily readable report. In order to ease the evaluation of the thesis, it is important that the cross-references are correct. In the making of the report, strong emphasis should be placed on both a thorough discussion of the results and an orderly presentation.

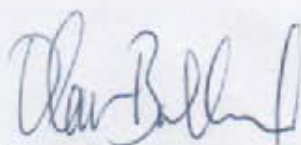
The candidate is requested to initiate and keep close contact with his/her academic supervisor(s) throughout the working period. The candidate must follow the rules and regulations of NTNU as well as passive directions given by the Department of Energy and Process Engineering.

Risk assessment of the candidate's work shall be carried out according to the department's procedures. The risk assessment must be documented and included as part of the final report. Events related to the candidate's work adversely affecting the health, safety or security, must be documented and included as part of the final report.

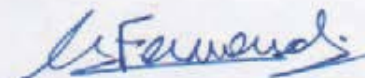
Pursuant to "Regulations concerning the supplementary provisions to the technology study program/Master of Science" at NTNU §20, the Department reserves the permission to utilize all the results and data for teaching and research purposes as well as in future publications.

The final report is to be submitted digitally in DAIM. An executive summary of the thesis including title, student's name, supervisor's name, year, department name, and NTNU's logo and name, shall be submitted to the department as a separate pdf file. Based on an agreement with the supervisor, the final report and other material and documents may be given to the supervisor in digital format.

Department of Energy and Process Engineering, 16. January 2012



Olav Bolland
Department Head



Maria Fernandino
Academic Supervisor

Research Advisors: Carlos A. Dorao

Preface

This thesis is a result of the master project in Engineering Fluid Dynamics TEP 4925 at the Norwegian University of Science and Technology (NTNU). It comprises 30 study points or the work load in the 10th semester of the master's degree in Mechanical engineering.

Acknowledgements

First I would like thank First Amanuensis Maria Fernandino for giving me insight in to their new technology, and for giving me the opportunity to work with this project. This was a great learning experience. Thanks for support, advices and guidance.

I would also like to extend my gratitude to First Amanuensis Carlos A. Dorao for reviewing my work and giving valuable suggestions.

Abstract

Natural gas is a vital component of the world's supply of energy. In Norway all the gas can be found offshore where it needs to be processed before transport. A vital part of the processing is gas and liquid separation.

Current gas-liquid separators are big and expensive, and the offshore industry is looking for more compact separators. One of the more prominent technologies is the NNGLseparator developed at NTNU. To further identify its possibilities, a thorough research program has been started

In this thesis one-dimensional models describing pressure drop and separation performance of the NTNU Natural Gas Liquid Separator (NNGLseparator) for dispersed gas-liquid flows has been studied. Here modeling of separation performance was divided into cyclonic separation and droplet capture by the meshpad, and then combined in sequence. The droplet capture is assumed to occur before cyclonic separation.

To analyze the impact of centrifugal force on droplet capture, the force was included in a previous proposed model describing droplet capture by a single fiber in the meshpad. With this as basis, modeling of total droplet capture for the meshpad was analyzed. Through this analysis we proposed an extension on the existing model for the case of the flow not following the rotation of the meshpad.

The droplets that are not captured are then separated through cyclonic separation. To model this separation mechanism, a modified time of flight model was developed. The modification includes the mesh porosity, and a β -factor describing the droplet's reduced radial velocity due to the obstructing meshpad.

Existing models for pressure drop across fixed porous media were compared to experimental data to identify which model best applies to the meshpad used in the NNGLseparator. How this model performs in describing a rotating porous media was then analyzed for the two scenarios; fully developed flow before mesh entry and developing flow inside a rotating meshpad. Through this analysis an extension to the pressure drop model was proposed, which includes the tangential velocity difference between rotating mesh and gas flow.

A previous proposed model for pressure drop across wet mesh pad was reviewed. This led to a discussion on how liquid hold up differs in the NNGLseparator from conventional fixed meshpads.

The proposed one-dimensional models were then analyzed through a parametric study of the separator performance in terms of pressure drop and efficiency of droplet separation for different flow conditions and geometries.

Sammendrag

Naturgass er en viktig komponent for å forsyne verden energibehov. I Norge befinner all gassen seg offshore hvor den må prosesseres før transport. En viktig del av prosesseringen er gass og væske separasjon.

Dagens gass-væske separatorene er store og dyre, og offshoreindustrien er på jakt etter mer kompakte separatorene. En av de fremtredende teknologiene er NNGL-separatoren utviklet på NTNU. For ytterligere å identifisere separatorens muligheter, har et grundig forskningsprogram blitt igangsatt

I denne avhandlingen er endimensjonale modeller, som beskriver trykkfall og separasjonsytelse av NTNUs Natur Gass Væske Separator (NGL-separator) for dispergerte gass-væske strømninger, blitt studert. Modellering av separasjonsytelse ble delt inn i sentrifugalseparasjon og dråpe fangst av fibernet. Disse separasjonsmekanismene ble deretter kombinert, hvor dråpefangst forutsettes å skje før syklonseparasjon.

For å analysere effekten av sentrifugalkraften på dråpefangsten, ble kraften inkludert i en tidligere foreslått modell som beskriver en enkel fibers dråpefangst. Med dette som basis, ble modellering av total dråpe fangst for fibernet studert. Gjennom denne studien foreslo vi en forlengelse av den eksisterende modellen for tilfellet hvor strømning ikke følger fibernetets rotasjon.

Dråpene som ikke fanges opp blir separert gjennom sentrifugalseparasjon. For å modellere denne separasjonen mekanismen, ble en modifisert flygetid modell utviklet. Modifikasjonen inkluderer filterelementets porøsitet og en β -faktor, som beskriver dråpens redusert radielle hastighet på grunn av fibernetets hindring av dråpens flygebane.

Eksisterende trykkfallmodeller for statiske porøse medier ble sammenlignet med eksperimentelle data, for å identifisere hvilken modell som best beskriver filternettet brukt i NGL-separatoren. Hvordan denne modellen klarer å beskrive roterende porøse medier ble deretter analysert for to scenarier; fullt utviklet strømning før fibernetet og strømning som utvikles inni det roterende fibernetet. Gjennom denne analysen ble det foreslått en modifisering av trykkfallmodellen. Modifiseringen inkluderer den tangentielle hastighetsforskjellen mellom det roterende fibernetet og strømningen.

En tidligere foreslått trykkfallmodell for våte fibernet ble studert. Dette førte til en diskusjon om hvordan væske opphold for NGL-separatoren skiller seg ut fra konvensjonelle statiske fibernet.

De foreslåtte endimensjonale modellene ble deretter analysert gjennom en parametrisk studie for separatorens ytelse i forhold til trykkfall og dråpeseparasjonseffektivitet for ulike strømningsforhold og geometrier

Contents

Preface.....	I
Acknowledgements.....	II
Abstract.....	III
Sammendrag.....	IV
List of figures.....	VII
List of tables.....	XI
Definition of terms.....	XII
Notation.....	XIII
Latin symbols.....	XIII
Greek symbols.....	XV
1 Introduction.....	1
1.1 Background.....	1
1.2 Conventional gas-liquid separators.....	2
1.3 Newer technology.....	4
1.4 Goal and outline.....	6
2 Literature review.....	8
2.1 Introduction.....	8
2.2 Annular flow.....	8
2.2.1 Thin film approximation.....	10
2.2.2 Thick film.....	12
2.2.3 Interfacial waves and three regimes.....	13
2.2.4 Empirical methods for prediction of annular flow.....	14
2.3 Dry flow through porous media.....	17
2.3.1 Pressure drop.....	18
2.4 Porous-continuum equation.....	20
2.5 Droplet separation and flow in centrifugal field.....	21
2.5.1 Time of flight model.....	22
2.5.2 Swirl flow.....	25
3 Modeling.....	27
3.1 Introduction-A complete model for efficiency and pressure drop.....	27

3.2	Droplet separation.....	30
3.2.1	Single target droplet capture	30
3.2.2	Overall droplet capture.....	34
3.2.3	Time of flight model	36
3.2.4	Results and discussion.....	38
3.3	Pressure drop	40
3.3.1	Introduction	40
3.3.2	Dry flow	41
3.3.3	Wet pressure drop.....	50
3.3.4	Results and discussion.....	54
3.4	Meshpad characteristics.....	58
4	Analysis and Parametric study.....	60
4.1	Introduction	60
4.2	Separation performance	62
4.2.1	Analysis.....	62
4.2.2	Plots.....	67
4.3	Pressure drop	74
4.3.1	Results and discussion.....	74
4.3.2	Plots.....	76
4.4	Summary of the proposed models	79
4.4.1	Separation Performance	79
4.4.2	Pressure Drop	80
5	Conclusion	83
5.1	Suggestions for further Work	84
	Appendix A	85
	Appendix B	87
	Appendix C	89
	Bibliography.....	95

List of figures

Figure 1 Illustration of how Oil and Gas are entrapped beneath the earth's crust. Figure taken from American Gas Association	1
Figure 2 A sketch of vertical and horizontal liquid/gas separators	2
Figure 3 Droplet capture in a mesh-type mist eliminator (Amistco, 2004).	3
Figure 4 Droplet capture in a vane type mist eliminator (Sulzer, 2011)	3
Figure 5 Cut-away of an axial flow cyclone (Straub & Collett Jr., 2004)	3
Figure 6 Cross-section of a Twister tube with typical process conditions (Twister BV, 2012)	4
Figure 7 The Rotating Particle Separator (RPS) applied as an in line separator. This version has a swirl generator upstream of the RPS and deswirlers downstream (van Wissen, 2006)	5
Figure 8 Principle sketch of the NNGLseparator	6
Figure 9 Annular flow regime in vertical pipe (Schlumberger, 2011)	8
Figure 10 Relationship between f_{LF} and Re_{LF} for thin-film approximation (Hewitt & Whalley, 1989)	11
Figure 11 Re-entrainment mechanisms (Ishii & Grolmes, 1975)	13
Figure 12 Flow through a porous medium (Holdich, 2002)	17
Figure 13 Evolution from molecular to continuum to porous continuum domain (Lage & Merrikh, 2005).	20
Figure 14 Illustration of the forces acting on a liquid droplet	21
Figure 15 Trajectory of a particle experiencing both centripetal and gravitational force	23
Figure 16 Particle collection efficiency in a centrifuge as a function of particle size normalized to D_{p50} (van Wissen, 2006)	24
Figure 17A, 12B and 12C various vortex forms (Swanborn, 1988).	25
Figure 18 Flowchart of the modeling of pressure drop and efficiency. The color code is explained in the top right corner	27
Figure 19 Simple illustration of the approximation of the NNGLseparator	29
Figure 20 Illustration of the effect of centrifugal forces on inertial impaction	30
Figure 21 A comparison of single target efficiency for different centrifugal acceleration when applying the gas flow	32
Figure 22 Comparison between the analytical approximation by Ranz and Wong to the empirical relation developed by Landhal and Herrmand.	33
Figure 23 Illustration of how Carpenter and Othmer (1955) divided the meshpad. Here the green lines represent the different layers.	34
Figure 24 Illustration of layers in a spinning mesh	35
Figure 25 Illustration how the droplet's flight path with mesh (blue arrow) and without (red arrow).	36
Figure 26 Illustration of single target capturing	38
Figure 27 Comparison of droplet separation efficiency through the time of flight model for different β -factors	39

Figure 28 Droplet separated with 50% efficiency as function of frequency. Droplet capture by mesh with 50% efficiency is inserted as reference (blue line).40

Figure 29 Comparison between the experiment for the use of the meshpad in conventional technologies (a), and experiments of meshpad used in the NNGLseparator with surrounding capturing tank (b).42

Figure 30 Modeling through the Hazen-Dupuit-Darcy equation compared to the experimental data for the conventional separator.43

Figure 31 Experimental results of pressure drop across the NNGLseparator with the inclusion of separating tank, compared to the Hazen-Dupuit-Darcy equation.44

Figure 32 Comparison of modeling by the Blake expression to experimental values. The error bar comes from the uncertainty in the relative density of the mesh.....44

Figure 33 Experimental results of pressure drop across the NNGLseparator with the inclusion of separating tank, compared to the Blake expression.45

Figure 34 The two scenarios applied in the analysis for the Hazen-Dupuit-Darcy equation validation for spinning mesh.45

Figure 35 Illustration between flow in a centrifuge and flow in centrifuging mesh. This comparison is used to show that the pressure drop in axial direction is not affected by the centrifugal effect when the forced vortex assumption is made.48

Figure 36 Illustration of modeling by layers49

Figure 37 Total and dry pressure drop as function of volumetric air flow. The liquid in this example is water52

Figure 38 Drainage area in the NNGLseparator compared to the conventional technologies.....53

Figure 39 Comparison for the Blake expression for 5% relative density to experimental data.....54

Figure 40 tangential velocity profile of combined vortex flow across the meshpad with a 20 Hz spin frequency55

Figure 41 Pressure drop compared for different swirl flows with air at standard atmospheric condition. Mesh spin is 20Hz56

Figure 42 Comparison between experimental data for pressure drop across still and spinning meshpad. The Hazen-Dupuit-Darcy equation is used as reference line.....57

Figure 43 Specific surface area of Duocel metal foams. Graph is taken from ERG Aerospace Corporation (ERG Aerospace, 2011).58

Figure 44 Three different sized meshes used in the analysis of pressure drop and separation performance of the NNGLseparator.....60

Figure 45 Comparison of droplet separation efficiency for different K-factors. Modeled with air and water mix at 15°C and standard atmospheric pressure.67

Figure 46 Droplet size separated with 50% efficiency as a function of the spin frequency for different K-factors. Modeled with Air and Water mix at 15°C and standard atmospheric pressure.67

Figure 47 Droplet size separated with 50% efficiency as a function of the K-factor for different spin frequencies. Modeled with air and water mix at 15°C and standard atmospheric pressure ...68

Figure 48 Droplet size separated with 50% efficiency as a function of the mesh height for different frequencies. Modeled with a 0.5 K-factor, Air and Water mix at 15°C and standard atmospheric pressure68

Figure 49 Droplet size separated with 50% efficiency as a function of the spin frequency for different mesh dimensions. Modeled with a 0.5 K-factor, Air and Water mix at 15°C and standard atmospheric pressure69

Figure 50 Comparison of droplet separation efficiency for different mesh dimensions and spins. Modeled with a 0.5 K-factor, at 15°C and standard atmospheric pressure.69

Figure 51 Comparison of droplet separation efficiency for the components: Air and Water, Natural gas and Oil, SF6 and Exxsol D80. Modeled with a 0.5 superficial gas velocity, 20HZ spin frequency 15°C and standard atmospheric pressure.....70

Figure 52 Comparison of 20 μm droplet separation efficiency for the components: Air and Water, Natural gas and Oil, SF6 and Exxsol D80, plotted against the superficial gas velocity. Modeled with 20 Hz spin frequency, 15°C and standard atmospheric pressure.70

Figure 53 Comparison of droplet separation efficiency for the components: Air and Water and Natural gas and Oil at high pressure. Modeled with 20Hz spin frequency, 5 m/s U_{SUP} and 15°C.71

Figure 54 Comparison of 20 μm droplet separation efficiency for the components: Air-Water at 6 and 80 bar and Natural gas –Oil at 6 and 80 bar, plotted against the superficial gas velocity. Modeled with 20 Hz spin frequency and 15°C.71

Figure 55 Comparison of droplet separation efficiency for the components: Air and Water and Natural gas and Oil at high pressure. Modeled with 20 Hz spin frequency a 0.5 K-factor and 15°C.72

Figure 56 Comparison of 20 μm droplet separation efficiency for the components: Air-Water at 6 and 80 bar and Natural gas –Oil at 6 and 80 bar, plotted against the K-factor. Modeled with 20 Hz spin frequency and 15°C72

Figure 57 Comparison of droplet separation efficiency for different mesh porosities. Modeled with 20Hz spin frequency, a 0.5 K-factor, air and water mix at 15°C and standard atmospheric pressure.....73

Figure 58 Comparison of pressure drop for different mesh dimensions as function of superficial gas velocity. Modeled with air at 15°C and standard atmospheric pressure.76

Figure 59 Comparison of pressure drop for different gas composition as function of superficial gas velocity. Modeled with Mesh A, 15°C and standard atmospheric pressure.76

Figure 60 Comparison of pressure drop for different gas composition and pressure as function of superficial gas velocity. Modeled with Mesh A and 15°C.....77

Figure 61 Comparison of pressure drop for different mesh dimensions as function of superficial gas velocity. Modeled with air at 15°C and standard atmospheric77

Figure 62 Comparison between pressure drop with air and 10 cm mesh height to Natural Gas with 17 cm mesh height. Modeled with air at 15°C and standard atmospheric78

Figure 63 Comparison between the Hazen-Dupuit-Darcy equation and experimental data.....80

Figure 64 Comparison of different swirl flow characteristics on the pressure drop.81
Figure 65 Illustration of the particle trajectory for droplet capture 0% and 100% efficiency89

List of tables

Table 1 Fluid properties at 101.325 kPa	61
Table 2 Fluid properties at 600 kPa	61
Table 3 Fluid properties at 8000 kPa	62
Table 4 Composition of the simplified Oil and Natural Gas.....	62
Table 5 Summary of the mesh dimensions, spin and K-factor proportionality to efficiency	66
Table 6 Proportionality to separation performance for different fluid components.....	66
Table 7 Proportionality in the pressure drop model.....	75
Table 8 Proportionality to pressure drop for different fluid components.....	75

Definition of terms

This thesis may refer to terms which are defined below:

Scrubber – Gas liquid separator removing small amounts of liquid typically below 3-5 volume%

Conventional Gas-Liquid Separator - In this thesis, the term "Conventional Gas-Liquid Separator" is referred to vertical or horizontal separators in which gas and liquid are separated by means of gravity settling with or without a mist eliminating device (demisters).

Capturing Tank – Cylinder surrounding the filter element in the NNGLseparator. The purpose of the tank is to capture the separated liquid, which will then settle in the tank.

Filter element – Refers to the element separating liquid from the gas in the NNGLseparator.

Demister (Mist Eliminator) - A device installed in the top of scrubbers, separators, tray or packed vessels, etc. to remove liquid droplets entrained in a flowing gas stream.

Liquid Holdup – This refer to the liquid accumulating inside the mist eliminator or the filter element

Flooded – If the liquid loading in to the mist eliminator is too high, the eliminator becomes choked with liquid, referred to as flooding.

Re-entrainment – This is the process of separated droplets becoming reintroduced (re-entrained) into the gas flow. This is an undesirable phenomenon

Core – From annular flow theory, referring to the center of the pipe which is only occupied with gas and liquid droplets

Droplet capture – Separation of droplets entrained in the gas flow by hitting the meshpad. Is pressuemd to be the separation mechanism that occur prior to centrifugal separation

Centrifugal separation – Separation of droplet entrained in the gas flow due to centrifugal force caused by the mesh spin. This also referred to as cyclonic separation, as it is the same separation mechanism that occurs in axial cyclones.

Notation

Latin symbols

Symbol	Unit	Description
A	m^2	Cross sectional area
a_c	N	Centripetal acceleration
C_D	-	Drag coefficient
C_P	m^{-1}	Form drag coefficient
c	kg/m^3	concentration of droplets in gas core
D	$\text{kg}/\text{m}^2\text{s}$	Deposition rate
D_p	m	Diameter of liquid droplet sphere
D_h	m	Hydraulic diameter
d_f	mm	Target diameter
E	$\text{kg}/\text{m}^2\text{s}$	Entrainment rate
F_C	N	Centrifugal force
F_D	N	Drag force
F_E	-	Fraction of liquid entrained as drops
f	hz	rotation frequency in revolutions per seconds
f_c	-	Friction factor, single phase in tube
f_{ci}	-	Interfacial friction factor, gas phase
f_{li}	-	Interfacial friction factor, liquid phase
g	m/s^2	Gravitational constant
h	m	Mesh height
K_P	m^2	Specific permeability
K	m/s	Souder Brown Coefficient, equation (4.2.1)
k	m/s	Droplet transfer coefficient

<u>Symbol</u>	<u>Unit</u>	<u>Description</u>
\dot{M}	kg/s	Mass flow
\dot{M}_L	kg/s	Liquid feed
\dot{M}_G	kg/s	Gas feed
\dot{m}	kg/m ² s	Mass flux, mass flow rate over cross sectional area
P	Pa	Pressure
Q_g	m ³ /s	Volumetric gas flow
Q_l	m ³ /s	Volumetric liquid flow
Re	-	Reynolds number
Re_{LF}	-	Liquid film Reynolds number, annular flow
Re_m	-	Modified Reynolds number, for porous media flow
R_w	m	Mesh radius
S_{mesh}	m ² /m ³	Mesh surface area
U	m/s	Gas velocity
U_{eff}	m/s	Effective velocity through wet porous media ($\frac{U_{sup}}{\epsilon_{eff}}$)
U_{por}	m/s	Velocity through porous media ($\frac{U_{sup}}{\epsilon}$)
U_{set}	m/s	Settling velocity
U_{sup}	m/s	Superficial velocity ($\frac{Q_g}{A}$)
u_θ	m/s	Tangential gas velocity
u_r	m/s	Radial gas velocity
u_z	m/s	Axial gas velocity
u^*	m/s	Friction velocity, (m/s)
V	m/s	Liquid velocity

Greek symbols

Symbol	Unit	Description
β	-	Mesh structure coefficient
δ	m	Liquid film thickness
ΔP	Pa	Pressure drop
ε	-	Mesh porosity, $\varepsilon = 1 - \frac{\rho_{rel}}{100\%}$
ε_{eff}	-	Effective mesh porosity
ε_t	m ² /s	Eddy diffusivity
ε_C	-	Fraction of area occupied with gas and liquid drops
ε_D	-	Fraction of cross sectional area occupied with drops
ε_G	-	Fraction of cross sectional area occupied with gas
η_C	-	Cyclonic separation efficiency
η_I	-	Capture efficiency, Inertial impaction, meshpad
η_{I-C}	-	Capture efficiency, including centrifugal force
η_{ST}	-	Capture efficiency, single target, meshpad
η_T	-	Overall separation efficiency, meshpad
μ_E	kg/ms	Effective viscosity
μ_g	kg/ms	Gas viscosity
μ_l	kg/ms	Liquid viscosity
ρ_{rel}	%	Mesh relative density
ρ_g	kg/m ³	Density gas
ρ_l	kg/m ³	Density liquid
σ	N/m	Surface tension
ψ_{I-1}	-	Separation number for inertial impaction
ψ_{I-2}	-	Centrifugal separation number for inertial impaction

τ	N/m^2	Shear stress
ω	rad/s	Meshpad angular velocity

1 Introduction

1.1 Background

Natural gas is a vital component of the world's supply of energy, and one of Norway's major exports. It is found deep underground in porous rock formations or cavities. It can occur alone in separated reservoirs, although it is more common as gas caps entrapped between petroleum and an impervious, capping rock layer in a petroleum reservoir (see Figure 1). In Norway all the reservoirs are off-shore under high pressure. This causes the gas to be mixed with or dissolve in the crude oil (Medici, 1974).

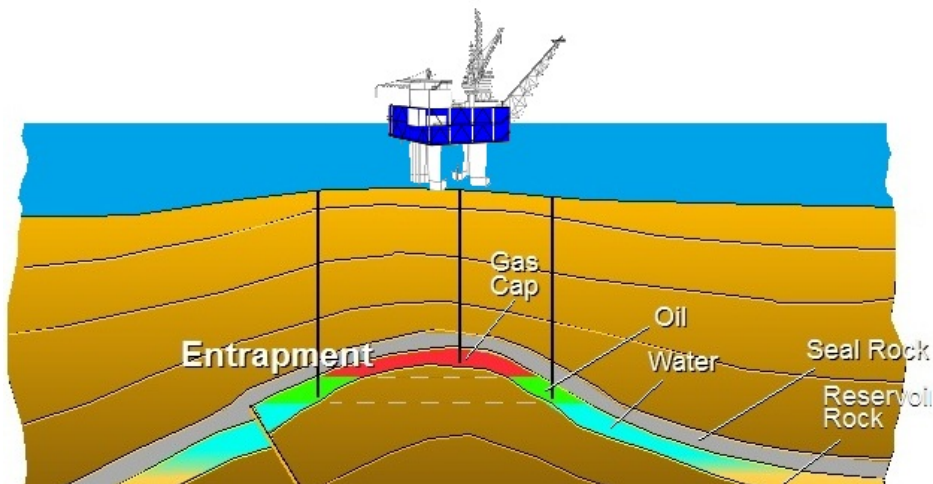


Figure 1 Illustration of how Oil and Gas are entrapped beneath the earth's crust. **Figure taken from American Gas Association**

The Natural gas which is exported is referred to as sales gas and is almost entirely composed of methane. However the natural gas extracted from reservoirs or wells, although still composed primarily of methane, is by no means pure. It contains oil, liquefied hydrocarbons, produced water, and acid components such as CO_2 and H_2S . The removal of these contaminants is the basis of natural gas processing. To prevent erosion, corrosion and plugging of process equipment the water needs to be removed as early as possible.

The major transportation pipelines and in particular the compressor used to transport the gas to shore, imposes restriction on the amount of contaminants in the gas. To prevent phenomena like scale, hydrate and wax formation to occur during transport the gas needs to be processed. Offshore platforms are therefore built to pre-treat the gas to make pipeline transportation possible. Liquid and gas are separated by gas scrubbers, and is a very important part of a

processing plant. Together with heat exchangers they form the heart of process for obtaining the hydrocarbon dew point specifications in an off-shore plant (Fredheim, 2011).

The conventional separation devices for purifying natural gas are mostly based on gravitational settling, a separation technique that gives large limitations to operation efficiency. With longer exploration of the wells, the amount of liquid in the product stream increases. This requires improvement of current separation equipment. The main problem is the size of currently used separators. Because the separation is based on gravitation, low gas velocities are needed to allow sufficient settling time. As a result these devices are big, heavy and expensive. This again requires heavier and more expensive supporting structures. In some cases, when the contaminant amount in the product stream increases, the exploitation of a well has to be stopped because the current gas treatment techniques are economically not viable. Furthermore, by transferring the separation process subsea exploitation costs are reduced making exploitation of smaller wells economically feasible. When the contaminants are separated downhole, the expensive conventional technique on the platforms becomes redundant. The offshore industry is therefore looking for compact and more efficient gas-liquid separation devices.

1.2 Conventional gas-liquid separators

Before we start exploring newer technologies for gas liquid separation we will take a look at how the separation is obtain in conventional technologies.

The traditional gas-liquid separators can be divided into two main categories, characterized by their orientation as vertical or horizontal (see Figure 2). They have their advantages and disadvantages, but in general the vertical separator is favorable for separating high liquid-gas ratio streams and the horizontal for low ratios.

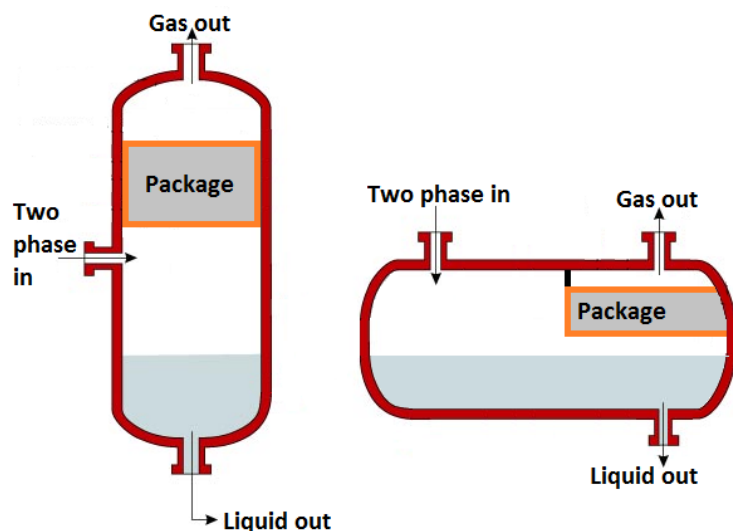


Figure 2 A sketch of vertical and horizontal liquid/gas separators

From Figure 2 the main design features are shown to be the same. Both consist of two phase inlet, section for settling the liquid droplets, liquid outlet at the bottom, gas outlet at the top and a package. The package represents different equipment, referred to as mist eliminators, used for separating entrained liquid droplets from the gas. Because the liquid entrained in the gas consist of a range of droplets sizes, different mist eliminator designs are needed for the separation of large and small droplets. Among the most common mist eliminators are meshpads, axial cyclones and vane packs.

Wire mesh demister or meshpad is a mist eliminator designed to remove small droplets with diameters down to $10\ \mu\text{m}$. It consists of metal or plastic wires with diameters between 0.15 and 0.28 mm knitted in a form resembling a net, or mesh. To eliminate droplets down to $1\ \mu\text{m}$ yarns or plastics can be knitted in to the mesh, referred to as co-knit mesh (Amistco, 2004). It is these wires that enable the liquid to be separated from the gas. When the gas flows through the meshpad droplets strikes the wires, and coalesce to form droplets large enough to trickle down and separate from the gas flow (see Figure 3 for an illustration of the droplet capture).

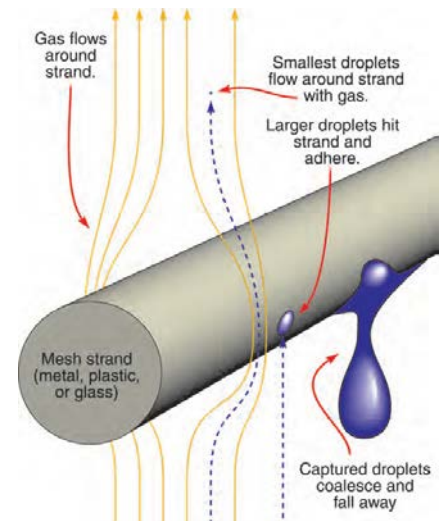


Figure 3 Droplet capture in a mesh-type mist eliminator (Amistco, 2004).

The meshpad is used to separate small liquid droplets, but when the liquid amount is large and the droplets are big it does not manage to drain the liquid fast enough. This results in the meshpad being flooded with liquid reducing its efficiency dramatically. To prevent this, other designs such as the vane pack mist eliminator are used upstream of the meshpad to remove the larger droplets.

Vane pack mist eliminators (Figure 4) can handle a higher liquid amount as opposed to meshpad. It removes droplets from the gas by forcing the gas to change direction as it flows through. The inertia or momentum keeps mist droplets moving in straighter paths causing them to strike the vanes.

Mist droplets are then held by the surface forces as they coalesce with other droplets, and eventually trickle down.

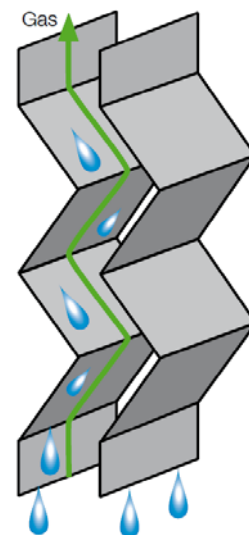


Figure 4 Droplet capture in a vane type mist eliminator (Sulzer, 2011)

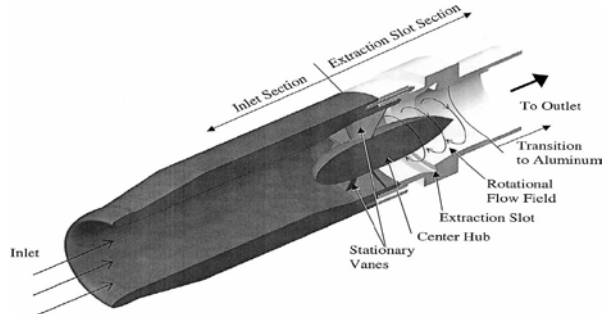


Figure 5 Cut-away of an axial flow cyclone (Straub & Collett Jr., 2004)

The third mist eliminator is the axial cyclone (Figure 5), which make use of centrifugal forces in separation of droplets from the gas. Here a tube

containing a series of fixed blades angled to the axial direction sets the gas flow carrying the droplets into rotation forcing the droplets out to the wall by centrifugal forces.

The conventional technologies just mentioned has different efficiency in terms of the droplet size it manage to separate and the amount of liquid it can drain from the gas stream before it gets flooded. They therefore need to be connected in series according to their operational limits. Although this technique improves the total efficiency of the gas scrubber, it is still limited to low gas velocities. Hence large separators weighing several hundred tons are needed.

1.3 Newer technology

Newer technologies are in development, which exceeds the conventional technologies in terms of efficiency and handling of streams with high liquid-gas ratios. And with an increase in efficiency one is able to move away from the conventional tanks, as seen in Figure 2, to a separation integrated in to the piping (an illustration of this can be seen in Figure 7). These newer technologies are called in line separators. And the most prominent are the Twister Supersonic Separator, the Rotating Particle Separator (RPS) and the NTNU Natural Gas Liquid Separator (NNGLSeparator).

The Twister Supersonic Separator (Figure 6) is developed in Netherland by Twister BV. It has thermodynamics similar to a turbo-expander, and it operates as follows: The gas flows through guide vanes creating a swirl, and are then fed through a Laval nozzle expanding the gas to supersonic velocities. The expansion causes reduction in pressure and temperature, as a result mist of water and hydrocarbon condensate droplets are formed. The formatted condensation droplets are removed from the gas through cyclonic separation. After the separation the gas stream is slowed down in a diffuser, recovering some of the initial pressure (Twister BV, 2012).

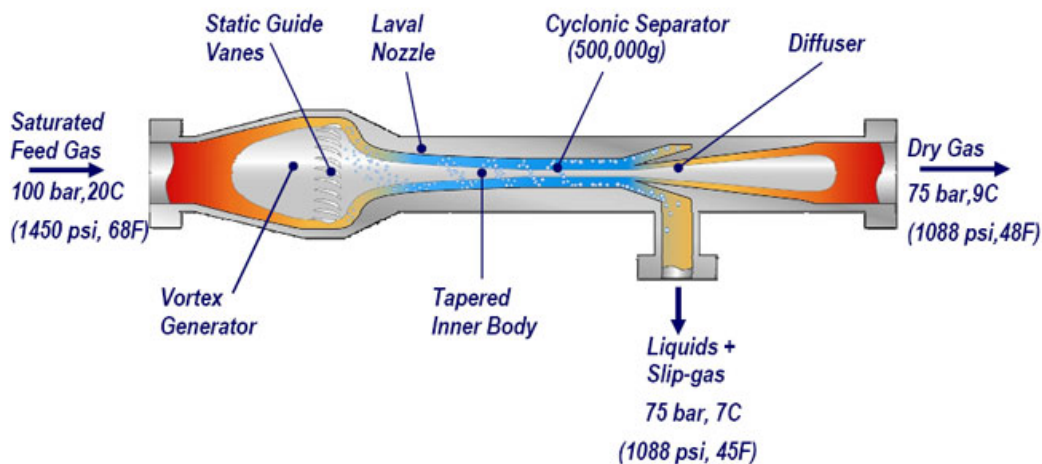


Figure 6 Cross-section of a Twister tube with typical process conditions (Twister BV, 2012)

One of the disadvantages of the separator is the high pressure loss (see Figure 6), which is the consequence of expansion by acceleration through the Laval nozzle. Further disadvantages are the limitations in terms of the liquid-gas ratio it is designed for. The separator can only handle low liquid-gas ratio, which shortens its life span on wells where the amount of liquid in the product stream increases with exploration of the well.

Another compact separation technology is the Rotating Particle Separator (RPS), which has been in development for several years, patented as early as 1988 (Eur. Patent 0286160, 1988). The RPS core component is a cylinder packed with a larger number of axially oriented channels which rotate as a whole around a common axis (see Figure 7). Particle or droplets are centrifuged to the outer walls of each channel, and adheres to the collecting walls as results of the action of centrifugal forces, van der Waals forces and/or forces due to surface tension (Brouwers J. , 1997)¹.

Several practical versions of the RPS were developed and implemented in various fields of operations. For example, Philips incorporated the RPS in a stand-alone air cleaner for domestic appliances which was sold world-wide (Brouwers, 2012). The version seen in Figure 7 is meant for separation of CO₂ and H₂S from natural gas, and consists of a swirl generators and an expansion turbine upstream and downstream of the RPS core. Although it was initially intended as separator of particulate material from gas (Eur. Patent 0286160, 1988), the version marketed for the oil and gas industry is an oil-water separator which was introduced by the Coalescence company under the name CLSR Coalescing Pump (Coalescence, 2011).

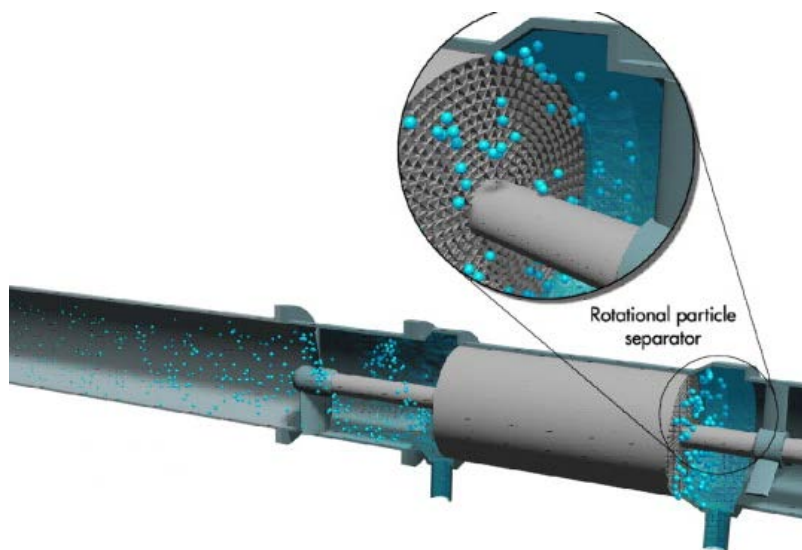


Figure 7 The Rotating Particle Separator (RPS) applied as an in line separator. This version has a swirl generator upstream of the RPS and deswirler downstream (van Wissen, 2006)

¹ A flash animation describing the use of the RPS can be seen on <http://www.wtb.tue.nl/woc/ptc/research/RPS/>

There exists studies on the use of the RPS as a gas-liquid separator (Mondt, 2005; van Wissen, 2006), but it does no longer seem to market itself towards the natural gas industry. It is therefore still a need for a compact and light-weight gas-liquid separator which can handle large liquid content. This leads us to one of the most recent technologies developed by Dorao and Fernandino at NTNU, the NNGLseparator (Figure 8).

The NNGLseparator resembles the meshpad demister reviewed in section 1.2, both consisting of a meshpad and a liquid storage unit. But unlike the conventional technology the meshpad spins (Figure 8).

The spinning meshpad creates a centrifugal field shooting the liquid in to a surrounding capturing tank. This increases the drainage of the filter element (meshpad) preventing it from getting flooded at high liquid-gas ratios, which is one of the main problems of the conventional technologies. This also enables it to handle higher gas-liquid ratios than the supersonic separator.

At high liquid-gas ratios a liquid film will form on the pipe walls. This liquid film is separated through a gap before the filter element, while the entrained droplets are separated in the filter element. The separated liquid is drained from the capturing tank, and the dry gas flows through the rotating meshpad and leaves the separator.

The NNGLseparator is still in a development phase and there have only been small scale tests with air-water at atmospheric conditions. Tests with conditions closer to real hydrocarbon systems (using hydrocarbons and higher pressure) are being planned for the near future. In addition to these tests and in order to further identify its possibilities as a compact device for separating liquid from natural gas under conditions required for offshore operation, a thorough research program has been started. This thesis is part of this ongoing research activity.

1.4 Goal and outline

The best way to get a complete picture of how the NNGLseparator will perform under the conditions required in offshore operations is to mimic these conditions in full scale testing. However copying the full range of conditions it may experience in operation, through laboratory experiments, is difficult. Therefore a way to predict its performance is to develop good models which can be tested and validated through small and large scale testing. Simulations through these models can then be used to analyze the NNGLseparator at different conditions.

The purpose of this work is to develop a model describing the pressure drop and separation performance of the NNGLseparator. The model is further used for a parametric study of the performance of the separator under different conditions.

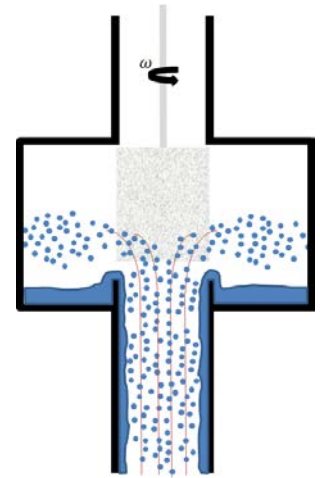


Figure 8 Principle sketch of the NNGLseparator

In this work, the NNGLseparator is described by a one-dimensional model based on the actual geometry of the first prototype of the separator.

In order to describe the separation efficiency of the NNGLseparator, existing models for droplet capture in a fixed wire mesh demister and models for centrifugal separation are modified and combined, thus obtaining a model capable of describing the effects of a rotating meshpad.

Existing pressure drop models through porous media are extended in order to include the spinning effect of the meshpad in the NNGLseparator. These models and involved approximations are analyzed by comparing to available experimental results and the more appropriate models are identified.

The proposed model is then used to do a parametric study of the separator performance in terms of pressure drop and efficiency of separation for different flow conditions and geometries.

This thesis is organized as follows. In chapter 2, a literature review on the basics and existing models needed for this work is presented. Chapter 3 contains a description of the proposed model and validation against experimental data. The most appropriate models describing the NNGLseparator and main modeling parameters are identified. An analysis of the proposed model and parametric study is presented in Chapter 4, together with a summary of the models. Chapter 5 contains the main conclusions of this work.

2 Literature review

In this section we will review studies on annular flow, previous proposed models for cyclonic separation, pressure drop across porous media and an approach for describing fluid motion in porous media through the governing equations.

2.1 Introduction

The two-phase flow upstream of the separator consists of both a liquid film on the walls and liquid droplets entrained in the gas. This flow structure is referred to as annular flow. Removal of the liquid film and the entrained droplets divides the NNGL-separator into two parts. First, the liquid film is removed at the inlet through a gap. The amount of liquid removed at the inlet is determined by the liquid film thickness upstream of the separator. Calculation of the liquid film thickness requires studies on annular flow theory.

Second, the remaining liquid in the upstream flow is entrained as liquid droplets in the gas flow. These droplets are removed by a spinning meshpad. This separation technique combines both the properties of porous structure in conventional meshpad demisters and centrifugal separation in cyclones. Therefore study on suggested models for the meshpad demister and cyclonic separation is included in this section.

2.2 Annular flow

Annular flow is a multiphase flow regime in which the lighter fluid flows in the center of the pipe, and the heavier fluid is contained in a thin film on the pipe wall. It occurs at high velocities of the lighter fluid, and is observed in both vertical and horizontal flows (Schlumberger, 2011).

In the derivation of the momentum equation for two phase flow new parameters are introduced to describe the flow, some of which can be seen in Figure 9. Here \dot{M}_{LF} represents the mass flow of the liquid film (kg/s), \dot{M}_G the mass flow of the gas, \dot{M}_{LE} the mass flow of the entrained liquid droplets and δ the film thickness (m). Other important parameters are the void fractions similar to the one used in flow through porous media, where ϵ_G is the fraction of total cross sectional area which is occupied by the gas. And similarly we have ϵ_d for cross section occupied with drops and ϵ_C occupied with core (gas and liquid drops).

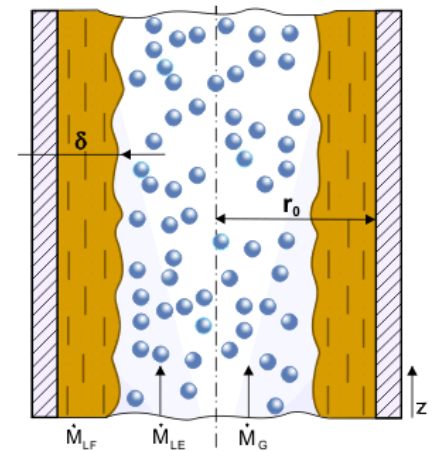


Figure 9 Annular flow regime in vertical pipe (Schlumberger, 2011).

In the derivation of the momentum equation the gas core is assumed as a homogenous mixture of droplets and gas. With this assumption the momentum equation for steady state flow in a circular tube may be written (Hewitt & Whalley, 1989):

$$-\frac{dp}{dz} = \frac{2\tau_i}{r_o - \delta} + \frac{1}{\epsilon_c} \frac{d}{dz} \left\{ \frac{\dot{m}^2 [x + F_E(1 - x)]^2}{\rho_c \epsilon_c} \right\} + \rho_c g \quad (2.2.1)$$

Here

r_o = pipe radius (m)

x = the quality (fraction of total flow which is in the form of gas)

F_E = fraction of the liquid phase entrained as droplets in the gas core

τ_i = the interfacial shear stress (N/m²)

\dot{m} = total mass flux (kg/m²s), given by the total mass flow rate (kg/s)/total cross sectional area (m²)

And ρ_c is the density of the core given by:

$$\rho_c = \frac{\dot{M}_{LE} + \dot{M}_G}{\dot{M}_G/\rho_G + \dot{M}_{LE}/\rho_L} \quad (2.2.2)$$

Equation (2.2.1) can be used to calculate the interfacial shear from measured pressure gradient when the film thickness and entrained fraction are known. However, there is still the problem of calculating film thickness and the respective shear stresses. In other words, the momentum balance equation is not particularly helpful in actually producing a solution to the problem (Hewitt & Whalley, 1989).

The liquid film along the wall is not smooth, but is covered by a complex system of waves, resulting in a constant interchange of liquid between the liquid film and the gas core. Droplets are entrained from the wave tips and are subsequently re-deposited back into the film (this is discussed in more detailed in section 2.2.3). Thus for practical predictions, it is necessary to have theoretical models or correlations for deposition (D) and entrainment rates (E). Normally the deposition rate is related to the concentration of droplets in the gas core (c , kg/m³, the mass of droplets per unit volume of the gas core) (Hewitt & Whalley, 1989):

$$D = kc \quad (2.2.3)$$

Where k = droplet transfer coefficient (m/s).

For a small element, a mass balance on the liquid entrained flow rate \dot{M}_{LE} gives for the case of entrainment or phase change:

$$\frac{d\dot{M}_{LE}}{dz} = -2\pi r_o D \quad (2.2.4)$$

Here z is the distance from the inlet (see Figure 9). Using equation (2.2.3) for D and that c is approximately equal to $(\rho_G \dot{M}_{LE})/\dot{M}_G$ then equation (2.2.4) can be integrated over a distance z_D to give:

$$k = \frac{\dot{m}_G 2r_o \ln(\dot{M}_{LE1}/\dot{M}_{LE2})}{4z_d \rho_G} \quad (2.2.5)$$

Where

\dot{m}_G = mass flux of the gas ($\text{kg}/\text{m}^2\text{s}$) = $\dot{M}_G/\pi r_o^2$

\dot{M}_{LE1} = entrained liquid mass flow rate at the inlet (kg/s)

\dot{M}_{LE2} = entrained liquid mass flow rate at the outlet (kg/s)

2.2.1 Thin film approximation

In this approximation the film thickness is assumed to be very small, leading to further assumptions:

- 1) Acceleration and gravity affects in the film is small
- 2) The effects of curvature in the film is small
- 3) The wall and interfacial shear stresses are approximately equal

For laminar flow this leads to the following simple equation

$$\tau \approx \tau_o \approx \tau_i = \mu_l \frac{du}{dy} \quad (2.2.6)$$

Here τ_o is the wall shear stress (N/m^2) and y is the distance from the wall

This approximation leads to the following equation for the liquid film flow rate (Hewitt & Whalley, 1989):

$$\dot{M}_{LF} = \int_0^\delta 2\pi r_o u \rho_l dy = \frac{\pi r_o \rho_l \tau_o \delta^2}{\mu_l} \quad (2.2.7)$$

For turbulent flow equation (2.2.6) is replaced by:

$$\tau = \mu_E \frac{du}{dy} \quad (2.2.8)$$

Here μ_E is the effective liquid viscosity (Ns/m^2), which varies with the wall shear stress and the distance from the wall (Hewitt & Whalley, 1989). For the thin film approximation the liquid film flow may be estimated using the value of the liquid film friction factor, f_{LF} :

$$\dot{M}_{LF} = 2\pi r_0 \delta \left[\frac{2\tau_0 \rho_l}{f_{LF}} \right]^{1/2} \quad (2.2.9)$$

The liquid film friction factor can be seen to be a function of the liquid film Reynolds number Re_{LF} , shown in Figure 10.

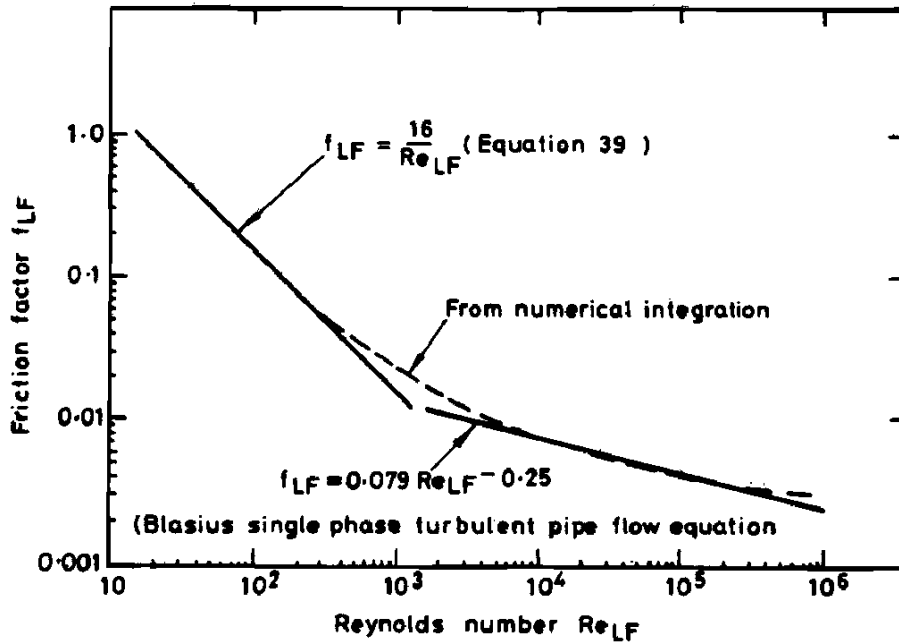


Figure 10 Relationship between f_{LF} and Re_{LF} for thin-film approximation (Hewitt & Whalley, 1989)

Here the liquid film Reynolds number, correlated to the liquid film velocity (u_{LF}) defined by:

$$Re_{LF} = \frac{4\rho_l u_{LF} \delta}{\mu_l} \quad (2.2.10)$$

The value of τ_0 in equation (2.2.9) may be acquired through the interfacial roughness relationship described in section 2.2.4a) (remember that the thin-film approximation assume $\tau \approx \tau_o \approx \tau_i$).

2.2.2 Thick film

In a more complete theory the shear stress within the film is not considered to be constant, as it was in the thin film approximation. Instead the distribution of the shear stress is calculated by carrying out a force balance on an angular ring of outer radius r and inner radius r_i ($r_i = r_0 - \delta$) and axial length δz . This leads to the following equation for the shear stress distribution (Hewitt & Whalley, 1989):

$$\tau = \tau_i \frac{r_i}{r} - \frac{1}{2} \left[\rho_l g + \frac{dP}{dz} \right] \left[\frac{r^2 - r_i^2}{r} \right] \quad (2.2.11)$$

By relating this to the laminar shear stress equation ($\tau = \mu_l \frac{du}{dy}$) an equation for the velocity distribution within the film can be obtained. Integrating the equation over the cross section of the pipe leads to the equation for the laminar film flow rate (Hewitt & Whalley, 1989):

$$\dot{M}_{LF} = \frac{2\pi\rho_l}{\mu_l} \left\{ \left[\tau_i r_i + \frac{1}{2} \left(\rho_l g + \frac{dp}{dz} \right) r_i^2 \right] \left[\frac{1}{4} (r_0^2 - r_i^2) - \frac{1}{2} r_i^2 \ln \left(\frac{r_0}{r_i} \right) \right] - \frac{1}{16} \left(\rho_l g + \frac{dp}{dz} \right) (r_0^2 - r_i^2)^2 \right\} \quad (2.2.12)$$

For the more common turbulent case the effective viscosity (see previous section) is commonly calculated from the sum of the laminar and turbulent viscosities as follows (Hewitt & Whalley, 1989):

$$\mu_E = \mu_l + \varepsilon_t \rho_l \quad (2.2.13)$$

Here ε_t is the eddy diffusivity (m^2/s). The common practice has been to relate ε_t with the single phase flow expressions (Hewitt & Whalley, 1989):

For $y^+ < 20$ the Deissler(1952) equation has been used:

$$\varepsilon_t = n_k^2 u y \left[1 - \exp \left(-\rho_l n_k^2 \frac{u y}{\mu_l} \right) \right] \quad (2.2.14)$$

And for $y^+ > 20$ the von Karman (1939) expression:

$$\varepsilon_t = \frac{k_k (du/dy)^3}{(d^2u/dy^2)^2} \quad (2.2.15)$$

Here n_k^2 and k_k are dimensionless constant with values 0.1 and 0.4.

2.2.3 Interfacial waves and three regimes

Liquid re-entrainment is associated with liquid film Reynolds number Re_{LF} , causing ripples or disturbance waves on the surface.

The break-up of the liquid film that is formed by the separated droplets is supposed to be the major source of re-entrainment if the maximal capacity of the separator is exceeded (Swanborn, 1988). The two principle mechanisms that determine film break-up can be seen in Figure 11.

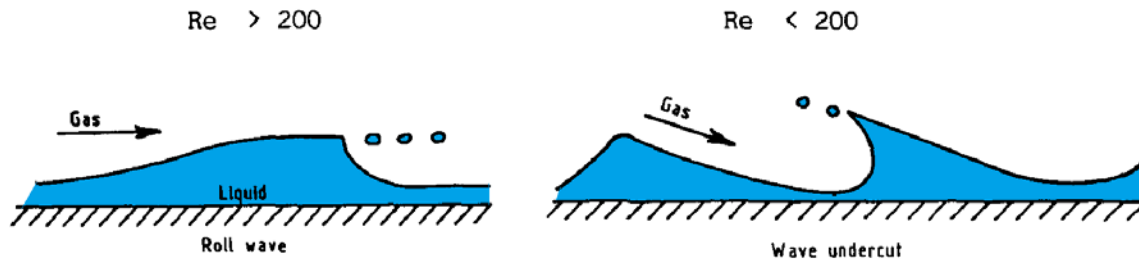


Figure 11 Re-entrainment mechanisms (Ishii & Grolmes, 1975)

The first mechanism (roll wave) appears at thick films and high liquid film Reynolds number. Under certain conditions an extreme deformation of the top of the wave leads to the formation of numerous drops (Swanborn, 1988).

In the second mechanism (wave undercut) the gas starts to cut under the wave. The wave starts to bulge and can eventually burst by the pressure inside the half closed bubble. Wave under cut is not often encountered and it takes place only at low liquid film Reynolds number (Swanborn, 1988).

The phenomena of re-entrainment can roughly be separated in to three schemes: Minimum Reynolds number Regime (where no re-entrainment will occur), rough turbulent regime (re-entrainment of a liquid film will take place, irrespective of its Reynolds number) and transition regime connecting the first and second regime.

For two-phase mixtures in co-current flow the transition regime starts at a certain minimum liquid film Reynolds number (Re_{LFmin}) and the rough turbulent regime starts from $Re_{LFmin} > 1500 - 1750$ (Ishii & Grolmes, 1975).

There are several correlations derived for the minimum liquid film Reynolds number, although earlier work (before 1970) have been argued to be too empirical, and not always consistent (Swanborn, 1988). Later correlations should therefore be considered. One of these was derived by Ishii and Grolmes (1975) to be:

$$Re_{LFmin} = \left(\frac{y^+}{0.347} \right)^{1.5} \left(\frac{\rho_l}{\rho_g} \right)^{0.75} \left(\frac{\mu_g}{\mu_l} \right)^{1.5} \quad (2.2.16)$$

Where y^+ represent the dimensionless distance from the wall based on the shear velocity, and was approximated by Ishii and Grolmes (1975) to equal 10. The criteria for the transition regime were estimated to:

Vertical upward flow (co-current):

$$160 < Re_{LFmin} < 1635$$

Downward flow:

$$2 < Re_{LFmin} < 1635$$

2.2.4 Empirical methods for prediction of annular flow

The object of an annular flow prediction scheme is usually to predict, knowing the initial liquid film flow rate \dot{M}_{LF} at a distance z , the value of flow rate at distance $z + \delta z$. Hewitt and Whalley (1989) gave a rather broad prediction scheme:

- 1) Prediction of deposition rate (D , kg/m²s) from $D = kc$. Hence the value of the mass transfer coefficient, k , is needed.
- 2) Calculation of entrainment rate (E , kg/m²s). Here the first step is to solve simultaneously the triangular relationship between δ , \dot{M}_{LF} and $\frac{dp}{dz}$ (equation(2.2.9)), and an empirical correlation for interfacial friction (see section a) below). Leading to a prediction of the interfacial shear stress (τ_i) and the film thickness (δ). These values are then used in an empirical correlation for entrainment rate E (section b) below).
- 3) Calculation of $d\dot{M}_{LF}$, which is estimated from the expression:

$$\frac{d\dot{M}_{LF}}{dz} = P \left(D - E - \frac{\varphi}{\Delta h_V} \right) \quad (2.2.17)$$

Where

P = channel periphery (m) = $2\pi r_o$

φ = heat flux (W/m²), positive for evaporation. Equals zero for adiabatic systems

Δh_V = latent heat for vaporization (J/kg)

a) Correlation for interfacial friction

The interfacial friction factor can relate to the core or the liquid phase². In the first case the shear stress on the interface is calculated from f_{ci} , the interfacial friction factor to the gas phase (Hewitt & Whalley, 1989):

$$\tau_i = f_{ci} \frac{1}{2} \rho_c u_c^2 \quad (2.2.18)$$

Here u_c is the velocity of the core.

$$u_c = 4\dot{M}_G / (\pi \rho_G d_o^2) \quad (2.2.19)$$

In the second case τ_i relates to f_{li} , the interfacial friction factor related to the liquid phase (Swanborn, 1988).

$$\tau_i = f_{li} \frac{1}{2} \rho_l u_l^2 \quad (2.2.20)$$

There have been several friction factor correlations relating to the three equation mention above. These are cited in “Multiphase science and technology” (Hewitt & Whalley, 1989) and “A new approach to the design of gas-liquid separators for the oil industry” (Swanborn, 1988).

Wallis(1969):

$$f_{ci} = f_c \left(1 + C_1 \frac{\delta}{2r_o}\right)^{C_2} \quad (2.2.21)$$

Here f_c = friction factor for single phase flow in the same tube of fluid density ρ_c , velocity u_c (=core velocity) and viscosity equal to gas viscosity μ_g . C_1 and C_2 are constants which Wallis (1969) found the following values fitted to his experiments (Swanborn, 1988):

$$C_1 = 360 \quad \text{and} \quad C_2 = 1$$

Baratan (1987) on the other hand found values of:

$$C_1 = 818200 \quad \text{and} \quad C_2 = 2.04$$

² Swanborn(1988) mention a correlation to the gaseous phase: $\tau_i = f_{gi} \frac{1}{2} \rho_g (u_g - u_i)^2$. Here u_i is the velocity of the interface. Although a mathematical expression for this velocity was not found, comparison between the friction factor f_{gi} by Swanborn (1988) and f_{ci} by Hewitt & Whalley (1989) indicates that the two expressions are the same.

Whalley and Hewitt gave the following correlation to f_{ci} :

$$f_{ci} = f_c \left[1 + 24(\rho_l/\rho_g)^{1/3} \frac{\delta}{2r_o} \right] \quad (2.2.22)$$

Both equation (2.2.21) and (2.2.22) were mention as unsatisfactory with scattered data (Hewitt & Whalley, 1989, s. 156).

Førde and Nørstrud (1984) quantified the influence of surface tension σ , and developed the following expression (Førde & Nørstrud, 1984):

$$\left(\frac{k_{ih}}{\delta} \right)_{eff} = 4 \sqrt{\frac{(1 - \varepsilon_G)}{\varepsilon_g}} \left(\frac{\sigma}{\mu_g u_g} \right)^{1/2} \quad (2.2.23)$$

Here

k_{ih} =height of instabilities on the film.

Hence, $(k_{ih}/\delta)_{eff}$ becomes the effective interfacial roughness and can be related to the more conventional surface roughness. The interfacial friction factor can then be determine conventionally, for instance with the graph of Moody, or with the explicit formula developed by Haaland (1981) as was done by Førde and Nørstrud(1984):

$$\frac{1}{\sqrt{f}} = -1.8 \log_{10} \left[\frac{6.9}{Re} + \left(\frac{k_{ih}}{3.7 \cdot D_h} \right)^{1.11} \right] \quad (2.2.24)$$

Here the D_h is the hydraulic diameter (m)

$$D_h = 2(r_o - \delta).$$

If the interfacial friction factor is related to the liquid phase it can be quantified as follows (Ishii & Grolmes, 1975).

Hughmark (1973):

$$\sqrt{f_{li}} = (K_1 Re_{LF}^m) \quad (2.2.25)$$

And

$$K_1 = 3.730 ; m = -0.47 \quad \text{for } 2 < Re_{LF} < 100$$

$$K_1 = 1.962 ; m = -1/3 \quad \text{for } 100 < Re_{LF} < 1000$$

$$K_1 = 0.735 ; m = -0.19 \quad \text{for} \quad Re_{LF} > 1000$$

By combining the equation for liquid film Reynolds number, the liquid interfacial shear stress and the interfacial friction factor given by Hughmark, equations for the film thickness can be obtain:

$$\delta = \frac{K_1}{\sqrt{32}} Re_{LF}^{m+1} \sqrt{\frac{\rho_l \mu_l}{\tau_i \rho_l}} \quad (2.2.26)$$

b) Correlation for deposition and entrainment in annular flow

In correlation for the deposition coefficient k , two are mentioned by Whalley and Hewitt (1989).

For low pressure, by McCoy and Hanratty (1977):

$$\frac{k}{u^*} = 4390 \left[\frac{\mu_G^2}{2r_o \sigma \rho_l} \right]^{1/2} \quad (2.2.27)$$

Here u^* = the friction velocity (m/s) given by:

$$u^* = \sqrt{\tau_i / \rho_c}$$

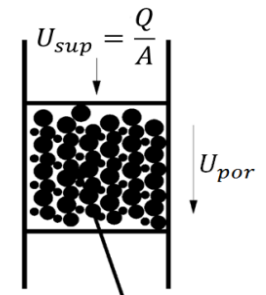
For high pressure, by Hewitt (1978):

$$\frac{k}{u^*} = 87 \left[\frac{\mu_l^2}{2r_o \sigma \rho_l} \right]^{1/2} \quad (2.2.28)$$

2.3 Dry flow through porous media

By definition, a porous medium consists of pores between some particulate phases, contained within a vessel or control volume, illustrated in Figure 12 (Holdich, 2002). Here the superficial velocity U_{sup} (m²/s) is the gas flow divided by the cross sectional area.

The porous media reduces the area available for fluid flow, and the fluid need to squeeze through the available area. Hence to preserve fluid continuity the velocity through the porous media is greater than the superficial velocity.



Porous medium

Volume fractions:
void fraction + solid fraction = unity
 $\mathcal{E} + C = 1$

Figure 12 Flow through a porous medium (Holdich, 2002)

The volume available for the fluid to flow through is referred to as the void and is represented as a fraction of the total volume called porosity (usually an isotropic property). Considering fluid continuity the velocity through the porous media can be expressed in relation to the superficial velocity as follows (Holdich, 2002):

$$U_{por} = \frac{U_0}{\varepsilon} \quad (2.3.1)$$

Here ε is the porosity.

2.3.1 Pressure drop

A natural consequence of flow through a porous media is a pressure drop. The pressure drop is a result of energy losses from the fluid due to viscous and form drag. The energy loss is related to the flow regime, turbulent or laminar, which is determined by the Modified Reynolds number. Here the traditional Reynolds number formula is modified by replacing the velocity with U_{por} . And a modification to the characteristic length (d) was deduced by Kozeny expressed as volume of the void over the surface area of the void. The modified Reynolds number then becomes:

$$Re_m = \frac{\rho_g U_{sup}}{\mu_g S_{mesh}} \quad (2.3.2)$$

When the modified Reynolds Number is large ($Re_m > 2$), turbulent conditions pertain (Holdich, 2002).

a) *Laminar*

When the flow is laminar ($Re_m < 2$) Darcy's law and the Kozeny-Carman equation are valid, and can be used to predict the pressure drop in the porous media. Darcy's law is a simple linear transport law and has the same form as Ohm's law, where the resistance is described by a constant for the permeability (k) of the porous media (Helsør, 2006).

Darcy's law:

$$\frac{\Delta P}{h} = \frac{\mu}{k} U_{sup} \quad (2.3.3)$$

The Kozeny-Carman equation was derived from the Hagen-Poiseuille equation for laminar flow of a fluid in a circular channel, where the Hagen-Poiseuille equation is:

$$\frac{\Delta P}{h} = \frac{32\mu}{d^2} u \quad (2.3.4)$$

Here d is the channel diameter (m) and u is the fluid velocity (m/s).

The derivation assumed that the flow through porous media can be represented as flow through many small channels. Hence the Hagen-Poiseuille equation could be modified in a similar fashion as the modified Reynolds number.

Kozeny-Carman equation (Holdich, 2002):

$$\frac{\Delta P}{h} = \mu \left[\frac{K_p S_{mesh}^2}{\varepsilon^3} \right] U_{sup} \quad (2.3.5)$$

Here K_p is the Kozeny constant, or the permeability of the media³.

b) Turbulent

When turbulence becomes significant ($Re_m > 2$) additional drag terms to the viscous ones becomes important. In pipe and channel flow a friction factor is used to represent this region. Carman extended the analogy with a porous media friction factor (Holdich, 2002).

The Carman correlation:

$$f = \frac{R_p}{\rho U^2} = \begin{cases} \frac{5}{Re_m} + \frac{0,4}{Re_m^{0,1}} & Re_m > 2 \\ \frac{5}{Re_m} & Re_m < 2 \end{cases} \quad (2.3.6)$$

Here R_p is the shear stress on the surface of the porous media. Applying a force balance on the surface gives the Blake expression (Helsør, 2006; Holdich, 2002):

$$\frac{\Delta P}{h} = f \frac{\rho_g U_{sup}^2 S_{mesh}}{\varepsilon^3} \quad (2.3.7)$$

c) A more general term

A more general term for the pressure drop is a quadratic extension of the Darcy equation, relating the pressure drop to a viscous drag and a form drag. The resulting equation is named Hazen-Dupuit-Darcy equation by Lage (Helsør, 2006).

$$\frac{\Delta P}{h} = \frac{\mu}{K_p} U_{sup} + C_p \rho U_{sup}^2 \quad (2.3.8)$$

³ There is much experimental evidence to suggest that $K_p = f(\varepsilon)$ (Holdich, 2002).

Here K_p is the permeability, and C_p is the form coefficient. Both are hydraulic properties of the porous medium. This expression for determining the pressure drop seems to appear more often in papers than the Blake expression (Helsør, 2006; Lage, 1998).

Lage (1998) make several arguments against the use of a modified Reynolds number in describing the flow through porous media, which is done in the derivation of equation(2.3.7). Implying that it is a short-sighted terminology to say that flow through any porous media is similar to flow through a straight conduit. He further argued that the uses of particle and pore diameter as the length parameter are not general enough, being appropriate only for very specific permeable media (Lage, 1998). However Lage’s arguments do not indicate that equation (2.3.7) is wrong, but rather that it is not general enough. This again may give an indication to why equation (2.3.8) has been the more popular choice in describing pressure drop through porous media.

2.4 Porous-continuum equation

The governing continuum transport equations are well known for describing fluids in a continuum domain, and consist of the continuity, momentum and energy equation. Reason studies have suggested modeling these equations inside a so called porous-continuum domain.

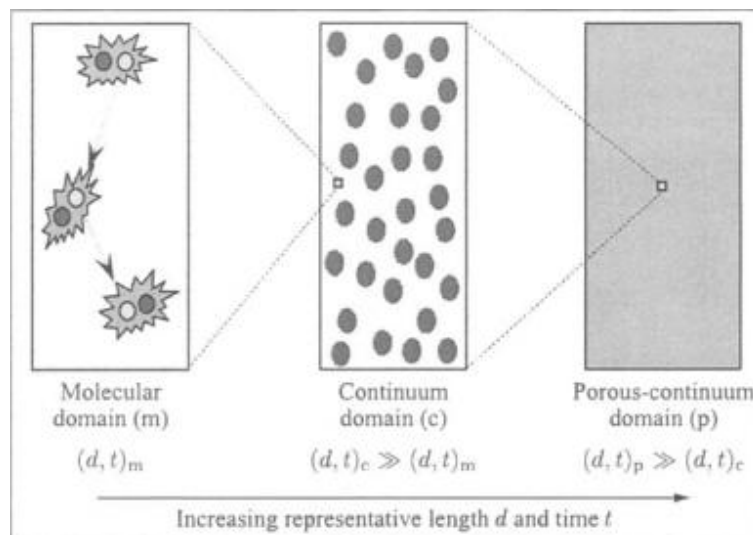


Figure 13 Evolution from molecular to continuum to porous continuum domain (Lage & Merrikh, 2005).

Figure 13 is taken from Lage and Merrikh (2005) and illustrates the transition from continuum to porous continuum domain.

In the porous continuum domain model, porous media is viewed in a macroscopic way and with low resolution. This view will eventually cause the porous media to blur with the fluid, forming a

single homogeneous porous-continuum medium. In this case the transport phenomena taking place within the enclosure can be modeled using a porous continuum model that treats the whole structure as a porous medium (Lage & Merrikh, 2005).

The most common porous continuum model available is the volume averaging method (Lage & Merrikh, 2005). Here the porous-continuum equation suggested by Lage (1998), Nield and Bejan (1999) are given by (Lage & Merrikh, 2005):

$$\nabla \cdot \langle u \rangle = 0 \quad (2.4.1)$$

$$\rho \left[\frac{\partial \langle u \rangle}{\partial t} + (\langle u \rangle \cdot \nabla) \langle u \rangle \right] = -\nabla \langle p \rangle + \mu_{eff} \nabla^2 \langle u \rangle + \rho g \beta (\langle T \rangle - T_c) j - \frac{\mu}{K_p} \varepsilon \langle u \rangle - \rho C \varepsilon^2 |\langle u \rangle| \langle u \rangle \quad (2.4.2)$$

$$(\rho c)_{eff} \frac{\partial \langle T \rangle}{\partial t} + (\rho c) \varepsilon \langle u \rangle \cdot \nabla \langle T \rangle = k_{eff} \nabla^2 \langle T \rangle \quad (2.4.3)$$

The variable within the brackets represents volume-averaged parameters. The fluid velocity $\langle u \rangle$ is the pore velocity U_{por} in equation(2.3.1), and the effective viscosity μ_{eff} is usually set as equal to the fluid viscosity μ . The last two terms in equation (2.4.2) represents the linear viscous-drag effect and the quadratic form-drag effect from equation (2.3.8) (Lage & Merrikh, 2005).

2.5 Droplet separation and flow in centrifugal field

Liquid droplets are entrained in the gas flow due to the drag force exerted by the gas. So for the liquid droplet to separate from the gas flow, the external force on the liquid droplets must exceed the drag force. Here the most basic external force is gravity, illustrated in Figure 14.

For the droplet to separate, gravity minus the buoyant force must be equal to the drag force exerted on the liquid droplet. This can be expressed by the following force balance equation.

$$(\rho_l - \rho_g) g V_p = F_D \quad (2.5.1)$$

Where

ρ_l =density of liquid (kg/m³)

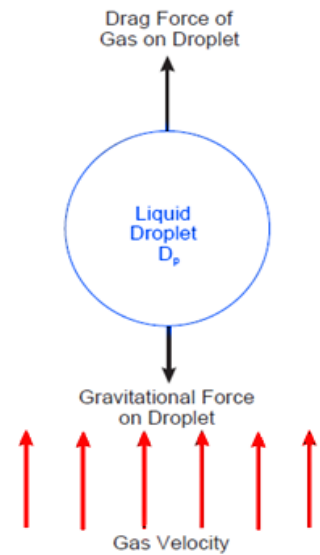


Figure 14 Illustration of the forces acting on a liquid droplet

ρ_g =density of the gas (kg/m³)

V_p =Volume of droplet, (m³)

F_D =Drag force (N)

g = gravitational constant, (m/s²)

If we assume the droplet to be spherical or can be assigned the diameter of an equivalent sphere, has small diameter, and moves so that viscous forces predominate, the drag force can be described by Stokes' drag expression (GPSA, 2004)

$$F_D = -3\pi U \mu_g D_p \quad (2.5.2)$$

Thus equation (2.1.1) becomes

$$(\rho_l - \rho_g)g \frac{4}{3}\pi \left(\frac{D_p}{2}\right)^3 + 3\pi U \mu_g D_p = 0 \quad (2.5.3)$$

Where

μ_g = gas viscosity, (kg/ms)

D_p = droplet diameter (m³)

U = gas velocity (m/s)

A rearrangement of equation (2.5.3) gives us the minimum gas velocity that causes the droplet to separate. Referred to as the settling velocity (U_{set}) (GPSA, 2004).

$$U_{set} = \frac{D_p^2(\rho_l - \rho_g)g}{18\mu_g} \quad (2.5.4)$$

A similar approach is used to describe the separation of droplets by centrifugal force, where the model describing the trajectory of a droplet in a centrifugal force is popularly named the time of flight model.

2.5.1 Time of flight model

It is well known that when a particle moves in a circular motion it will experience a centrifugal force field similar to gravity. And from a strict physical definition of force balance on the particle it is the centripetal force and not the centrifugal force that should be considered. It is then a

simple matter to arrive at an analogue expression to equation (2.1.3), for the radial settling velocity in a centrifugal field (Holdich, 2002).

Centripetal acceleration:

$$a_c = \frac{u_\theta^2}{r} \quad (2.5.5)$$

Radial settling velocity:

$$\frac{dr}{dt} = u_r(r) = \frac{D_p^2(\rho_l - \rho_g)u_\theta^2}{18\mu_g r} \quad (2.5.6)$$

Here u_θ (m/s) is the tangential velocity of the gas flow, and it is a fundamental parameter for cyclonic separation. This velocity will be discussed further in the next section.

An illustration of how the radial velocity affects particle trajectory can be seen in Figure 15. Here the gas flow with entrained liquid droplets enters the bottom and is set into circular motion. The increased inertia from the droplets' circular motion, drawn as the centrifugal force, together with drag force cause the droplet to increase its radial velocity resulting in an arced trajectory.

By integrating equation (2.5.6) from r_l to R_w , the time for the droplet to reach the wall (t_{radial}) can be found.

$$t_{radial} = \frac{18\mu_g}{D_p^2(\rho_l - \rho_g)\omega^2} \ln\left(\frac{R_w}{r_l}\right) \quad (2.5.7)$$

Here R_w is the radius of the centrifuge, and r_l is the distance from the droplet inlet position to the centrifuge center.

The gravitational forces can safely be excluded as it has little effect in centrifuges used for droplet separation. Therefore the time for the droplet to leave the top is the volume of the centrifuge divided by volume flow rate, Q .

$$t_{axial} = \frac{H}{v_z} = \frac{\pi R_w^2 H}{Q_g} \quad (2.5.8)$$

This is a simple time of flight model described by Holdich (2002).

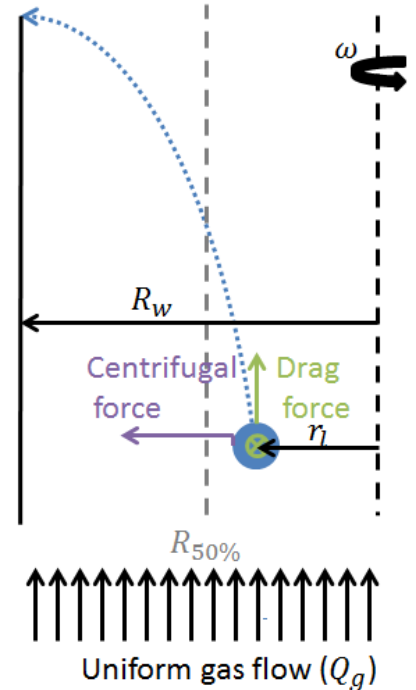


Figure 15 Trajectory of a particle experiencing both centripetal and gravitational force

The name of the model comes from comparing the size of t_{axial} and t_{radial} , leading us to two possible scenarios: Either $t_{axial} > t_{radial}$, and the liquid droplet will hit the wall before it leaves the separator, separating it from the gas flow. Or $t_{axial} < t_{radial}$, and the liquid droplet will not reach the wall within the centrifuge, but carry on entrained in the gas flow.

A more complete model for the efficiency of droplet separation in centrifugal field can be made by assuming uniform droplet distribution to estimate the lower bound capture particle diameter. This was described by van Wiessen (2006).

We consider a cylinder of radius R_w . Because of the uniform inlet flux 50% of the particles will enter the cylinder between R_w and $R_{50\%}$. The smallest droplet which undergoes a radial displacement of $R_w - R_{50\%}$ in the time t_{axial} , is therefore collected with 50% efficiency (van Wissen, 2006). The diameter of this droplet can be calculated by integrating equation (2.2.2) over the time t_{axial} .

$$r^2(t_{axial}) - r^2(0) = \frac{2(\rho_l - \rho_g)D_p^2}{18\mu_g} \int_0^{t_{axial}} u_\theta^2 dt \quad (2.5.9)$$

Where $dt = dz/u_{ax}$, $r(t_{axial}) = R_w$ and $r(0) = R_{50\%}$ resulting in

$$D_{p50} = \left[\frac{18\mu(R_w^2 - R_{50\%}^2)u_z}{2(\rho_l - \rho_g) \int_0^H u_\theta^2 dz} \right]^{1/2} \quad (2.5.10)$$

Particle collection efficiency is usually compared to the particle diameter nondimensionalized by D_{p50} , and described by an S-curve (see Figure 16). Where for $D_p \gg D_{p50}$ practically all particles will be removed; for $D_p \ll D_{p50}$ separation will be minuscule (van Wissen, 2006).

Any further description on the separation efficiency, except that it could be described by an S-curve, was not found in the literature study for this thesis.

To solve the equation describing the separation taking place within a cyclone we need to describe the swirl flow created, and get an expression for u in equation(2.5.10).

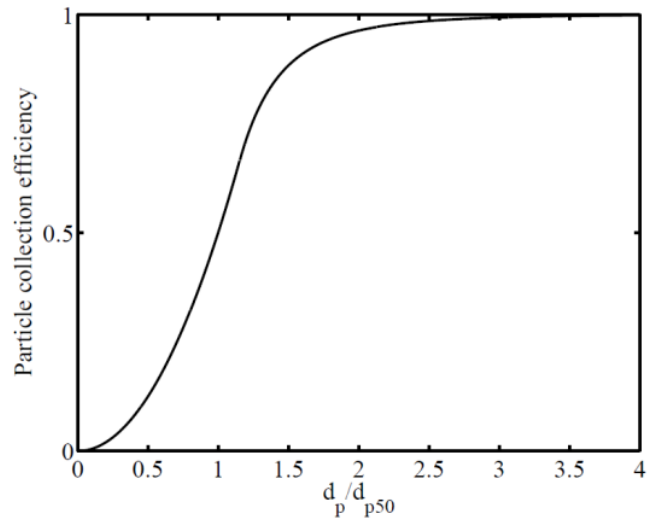


Figure 16 Particle collection efficiency in a centrifuge as a function of particle size normalized to D_{p50} (van Wissen, 2006).

2.5.2 Swirl flow

A description of swirling flow has been attempted by many researchers. Stern (1973) based his predictions on a laminar flow with no eddies. Seillan (1929), Lissman (1930) and Barth (1932) all assumed that vortices formed obeying the equation (Dickinson, 1998):

$$u_{\theta} = \alpha r^{-n}$$

Where

$$-1 \leq n \leq 1$$

The vortices formed by the swirl flow were then categorized into free, forced and combined vortex. Here “forced” and “free” vortex is represented by $n = -1$ and $n = 1$ respectively; anywhere in between represents a combination vortex. The velocity profile of the free, forced and combined vortex is shown in Figure 17A, B and C.

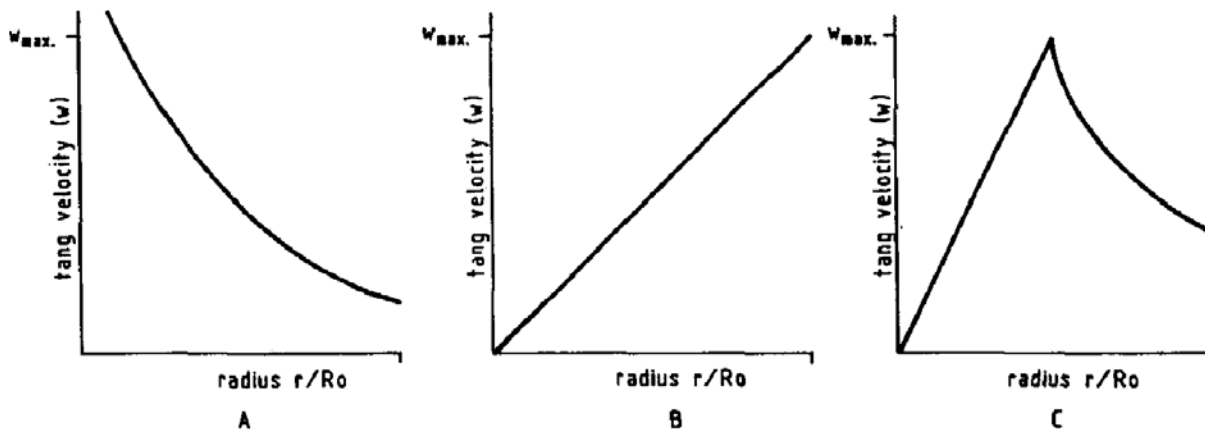


Figure 17A, 17B and 17C various vortex forms (Swanborn, 1988).

In free vortex the speed and rate of rotation of the fluid is greatest at the center, and decreases progressively with distance from the center. Usually a core forms in the middle, like water flowing down a plug hole.

In a forced vortex the speed is zero at the center and increases proportional to the distance from the center. This is the velocity of a fixed body of rotation like the spinning meshpad.

The last possible vortex is the combination of a free and a forced vortex generated across the diameter of a cyclone. This usually occurs with a forced vortex in the central region and a free vortex on the outside of the region. This is the vortex associated with cyclonic separation. To determine the maximum height, and the radius at which the tangential velocity reaches this maximum, is considered an important characteristic.

One of the challenges in modeling cyclonic separators is to determine which of these vortices describes the swirling gas flow. The swirl flow in conventional separators, like the axial cyclone, is usually described by the combined vortex, where it follows the forced vortex profile very close to the center.

3 Modeling

In this section we will analyze the models reviewed in the literature study to see if they are suitable to describe the NNGLseparator. Through this analysis we will show how the different models can be combined or modified in to new a mathematical models to better describe the separator.

3.1 Introduction-A complete model for efficiency and pressure drop

As a guide in describing which models in the literature study requires further review, a flow chart of the envisioned modeling process for pressure drop and efficiency in the NNGLseparator is included.

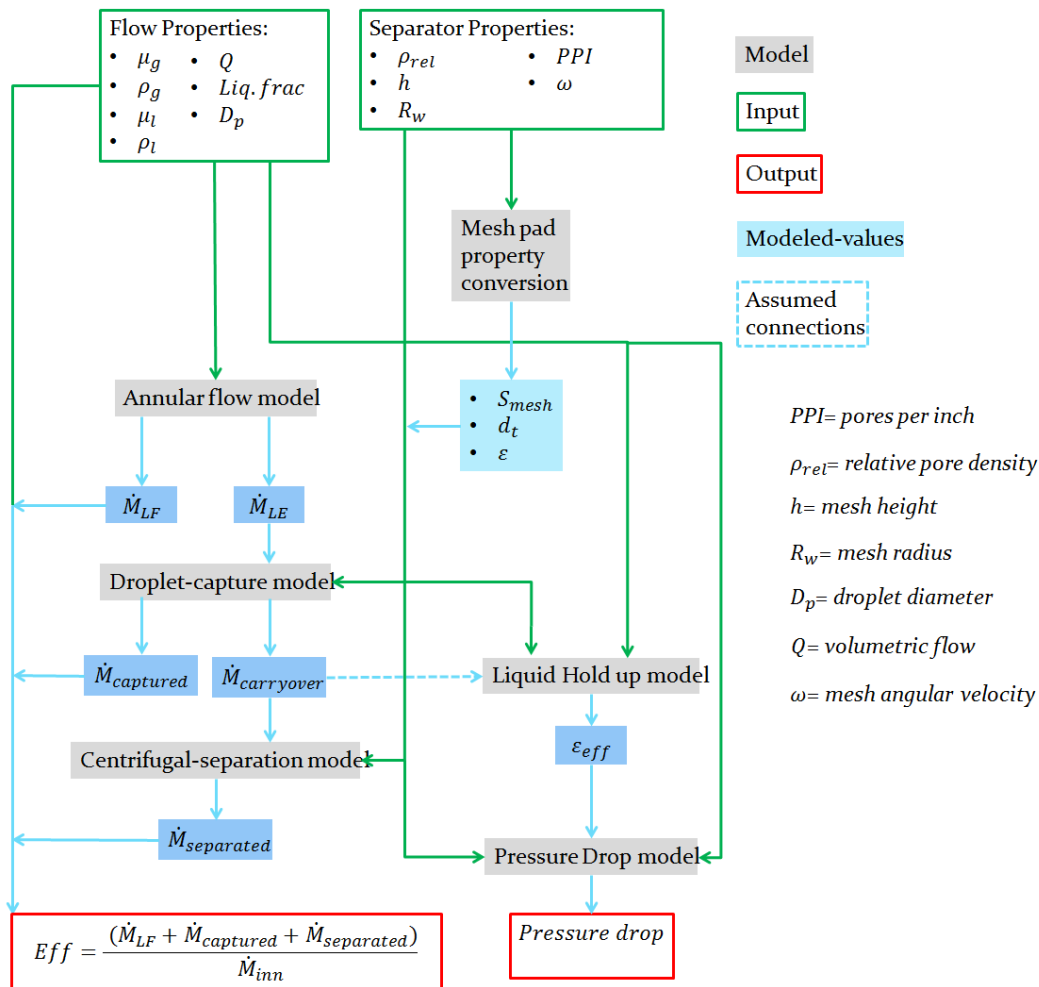


Figure 18 Flowchart of the modeling of pressure drop and efficiency. The color code is explained in the top right corner

Top right corner in Figure 18 gives a short description of the color code in the flow chart. Where the green indicates meshpad and fluid properties which are needed as input values in the different models (grey box), and the blue indicates output values from the models. Where these values are used is indicated by the arrows. Marked with a red box are the final output values from the complete model, pressure drop and efficiency.

The properties for the meshpad which are given by the manufacturer differ from the properties required in the model. Therefore a conversion of the properties from the manufacturer is needed, indicated in the flow chart by the “Meshpad property conversion box”. Here properties like the diameter of the mesh fibers (d_f) needs to be approximated.

The path on the right in Figure 18 leads to the pressure drop. Here the liquid hold up refers to the liquid that accumulates inside the mesh. This liquid will affect the properties of the meshpad, particularly the porosity, and needs to be modeled. Output from this model is referred to as effective porosity (ϵ_{eff}) and should be included in the pressure drop model.

Since the porous media in the NNGLseparator spins, an analysis on how this affect the models for pressure drop reviewed in the literature study is included. As well as a modified model which incorporates different flow characteristics that describe swirl flow (see explanation of free, forced and combined vortex flow in section 2.5.2).

The path for efficiency is shown to the left in Figure 18. Here the first part that needs to be modeled is the annular flow in the separator inlet. It assumed that the liquid film formed on the walls will be completely separated through the gap upstream of the filter element, and hence will add to the total efficiency. However the NNGLseparator design does not indicate a need for modification to the models on annular flow reviewed in the literature study. Focus is therefore put on parts where modifications deems far more necessary. This section does therefore not include an analysis on this already well-studied phenomenon.

A mechanism that needs to be studied is the droplet capture, referring to the droplets that strike the fibers inside the meshpad. Because this separation occurs during the droplet flight inside the mesh, this separation mechanism is assumed to take place before cyclonic separation. The output from the droplet capture model ($\dot{M}_{capture}$) is also assumed to be included in a model for liquid hold up. Therefore an analysis of current capture models and how they are affected by the spinning mesh is included. As well as a modified capture model incorporating other possible swirl flow characteristics.

The negative output from the droplet capture model ($\dot{M}_{carryover}$), which are the droplets that slips by the fibers in the mesh, are separated through centrifugal forces. Because this separation occurs inside a porous structure, a suggestion to a modified time of flight model is included in this section.

In addition to deriving new models and analyzing previous proposed models, the swirl flow inside the mesh is reviewed. Here it is assumed that the spinning mesh causes the flow to follow the forced vortex characteristics, thus the flow has the same velocity as the mesh. This assumption is analyzed by simulating a modified pressure drop model, and comparing it to previous experiments.

It is further assumed that the gas flow across the NNGLseparator can be approximated as flow through a spinning mesh inside a pipe. Thus the possibility of the gas to flow around the mesh is neglected. A simple illustration of this approximation can be seen below (Figure 19).

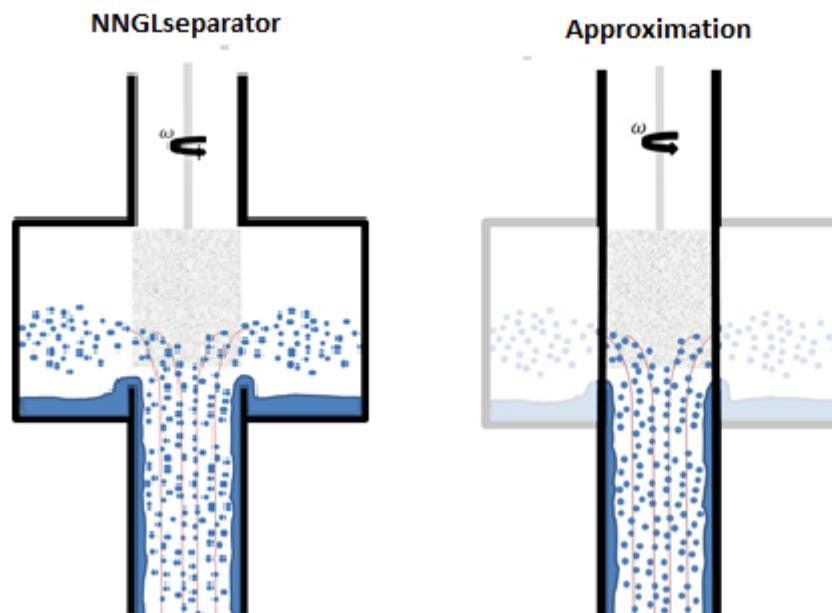


Figure 19 Simple illustration of the approximation of the NNGLseparator

When the models are compared to each other, or certain features of the models are discussed with results as reference, the properties of air and water at ambient temperature and 0.5 K-factor are applied in the simulation. These properties are cited in Table 1 in section 4.1. Here air and water was chosen since the referenced experimental data are for air and water, thus for consistency it has been applied in all simulation throughout this section.

3.2 Droplet separation

In the case of droplet separation, the capture of droplets by the mesh and the separation of droplets due to centrifugal forces are reviewed. Here the droplets are regarded as separated when they either hit the porous material (referred in this paper as the target when reviewed in microscopic scale) or leaves the meshpad due to centrifugal forces.

3.2.1 Single target droplet capture

The traditional modeling approach for single target droplet capture in a wire mesh demister is to consider the porous material as series of cylinders obstructing the two phase flow. Then the mechanisms for droplet separation are divided into capture by inertial impaction, direct interception and diffusion due to Brownian motion. When the flow is set to a spin modifications to the traditional models are needed. The most obvious difference from the traditional models is then to include the centrifugal force.

Our scenario for reviewing the impact of centrifugal force on the single target capturing efficiency will be to assume that the gas flow follows the mesh spin (see forced vortex regime section 2.5.2). This gives the strongest centrifugal force, thus the comparison gives the best indication of the spins impact.

In the separation by direct interception the mass of the droplet is ignored, hence the centrifugal force will not have an effect. Any effect on Brownian motion due to centrifugal forces have not been found, and therefore not considered. Our focus is therefore on the separation by inertial impaction. Here the centrifugal force should be considered in the force balance used to derive the collection efficiency by inertial impaction.

In Figure 20 you can see an illustration on how the centrifugal force will affect the inertia of the liquid droplet. The force balance on a liquid droplet can be expressed by:

$$\frac{d(m\vec{v})}{dt} = \vec{F}_E + \vec{F}_D \quad (3.2.1)$$

Here \vec{v} is the velocity vector of the droplet, \vec{F}_D the drag force and \vec{F}_E other external forces.

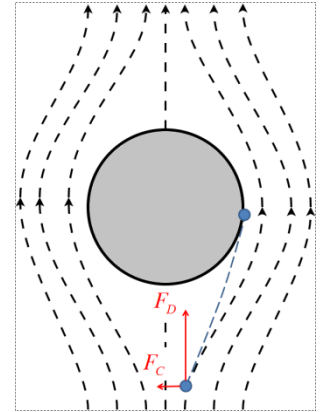


Figure 20 Illustration of the effect of centrifugal forces on inertial impaction.

In the derivation of the inertial single target efficiency for non-spinning mesh all external forces are usually excluded and the drag is assumed to follow Stokes' law. To analyze the mesh spinning effect on the single target efficiency the same approach is used except with the inclusion of the centrifugal acceleration (\vec{a}_c).

The next step is to separate equation (3.2.1) into a momentum equation in the x- and y-direction as follows:

$$2\psi_{I-1} \frac{d^2 \bar{x}}{d\bar{t}^2} + \frac{d\bar{x}}{d\bar{t}} - \bar{u}_x = 0 \quad (3.2.2)$$

$$2\psi_{I-1} \frac{d^2 \bar{y}}{d\bar{t}^2} + \frac{d\bar{y}}{d\bar{t}} - \bar{u}_y + 2\psi_{I-2} \bar{a}_c = 0 \quad (3.2.3)$$

Where equation (3.2.3) and (3.2.2) are nondimensionalized versions of equation(3.2.1), and:

$$\psi_{I-1} = \frac{\rho_g d_p^2 U_0}{18\mu_g d_f} \quad \psi_{I-2} = \frac{(\rho_l - \rho_g) d_p^2 U_0}{18\mu_g d_f} \quad \bar{x} = \frac{2x}{d_f} \quad \bar{y} = \frac{2y}{d_f} \quad \bar{u}_x = \frac{u_x}{U_0} \quad \bar{u}_y = \frac{u_y}{U_0} \quad \bar{t} = \frac{2U_0 t}{d_f}$$

$$\bar{a}_c = \frac{a_c d_f}{2u_0^2}$$

Here x and y is the position of the droplet, u_x and u_y represents the x- and y-velocity of the gas, u_0 the initial velocity of the gas, d_f the diameter of the target, ρ_l the density of the liquid droplet, ρ_g the density of the gas and μ_g the viscosity of the gas.

To solve equation (3.2.2) and (3.2.3) we need an expression for the gas velocity field (u_y and u_x) around the cylinder. Ranz and Wong (1952) were able to solve the momentum equations analytically by simplifying and approximating the gas flow field. With the exclusion of external forces they derived the following expression for single target efficiency due to inertial impaction.

$$\eta_I = \frac{S_2 - S_1}{S_2 \exp(S_1 t') - S_1 \exp(S_2 t')} \quad (3.2.4)$$

Where

$$S_{1,2} = -(1/4\psi_{I-1}) \pm \sqrt{(1/4\psi_{I-1})^2 + (1/2\psi_{I-1})}$$

$$t' = (1/q) \tan^{-1} \left[\frac{4\psi_{I-1} q}{\psi_{I-1} - 1} \right]$$

$$q = \sqrt{(1/2\psi_{I-1}) + (1/4\psi_{I-1})^2}$$

Because of the simplicity in Ranz and Wong approximation, this method was used to compare the impact of centrifugal forces on the momentum equations (3.2.2) and (3.2.3). With this approximation the following expression including the centrifugal acceleration was derived

$$\eta_{I-c} = \frac{S_2 - S_1 + F_c S_1 - F_c S_2 + F_c S_2 \exp(S_1 t') - F_c S_1 \exp(S_2 t')}{S_2 \exp(S_1 t') - S_1 \exp(S_2 t')} \quad (3.2.5)$$

Where

$$F_c = 2\bar{a}_c \psi_{I-2}$$

The full derivation of equation (3.2.5), and how the Ranz and Wong approximation is applied, can be seen in Appendix C.

Figure 21 shows a comparison between equation (3.2.4) and (3.2.5) for different centrifugal accelerations. Here the separation number ψ_{I-1} and ψ_{I-2} are close to equal, which would be the case for air and water. The ‘ac’ in Figure 21 represents the nondimensionalized centrifugal acceleration.

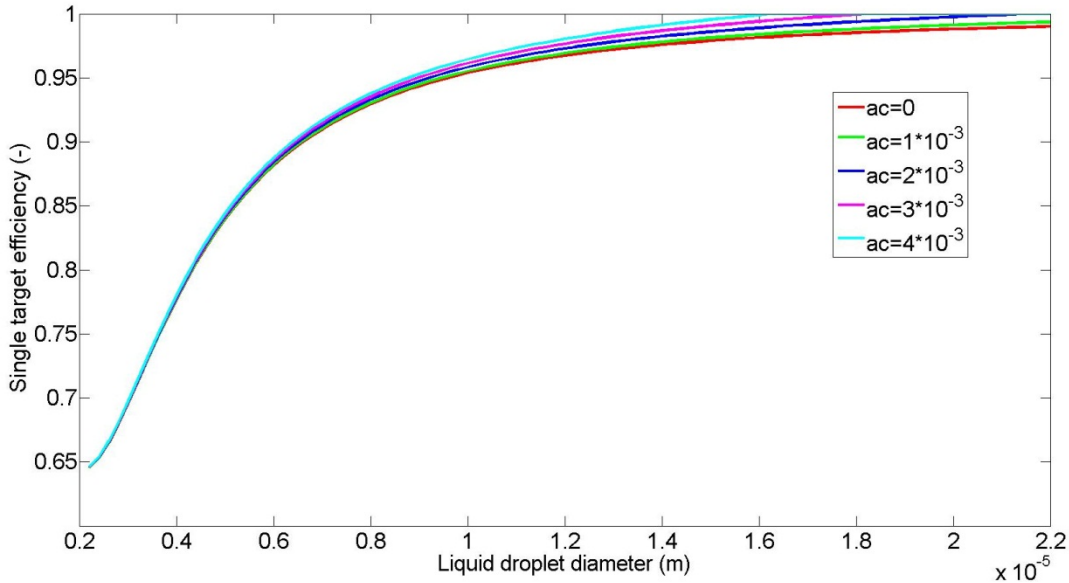


Figure 21 A comparison of single target efficiency for different centrifugal acceleration when applying the gas flow

From Figure 21 one sees that the single target efficiency for $\bar{a}_c = 1 \times 10^{-3}$ compared to the single target efficiency without centrifugal acceleration is almost the same. This nondimensionalized centrifugal acceleration does however not give much information before reviewing the mesh properties and the gas flow. But considering the target diameter in mesh demisters is usually around 0.3 mm (Helsør, 2006), the numbers represented in Figure 21 are

reasonably high. To get a sense of how high this number is let us consider a superficial gas velocity of 5 m/s, target diameter of 0.3 mm and $\bar{a}_c = 1 \times 10^{-3}$; then the centrifugal acceleration is 167 m/s^2 or close to 17G. This is a lot higher than what can be expected under normal operational condition for the NNGLseparator.

Based on this analysis one can therefore safely approximate the single target efficiency to the models for non-spinning mesh as long as $\bar{a}_c < 1 \times 10^{-3}$. This enables us to utilize an empirical model relation, found by Landhal and Herrmand (1949) which has shown to give a better estimation to the efficiency than the Ranz and Wong approximation.

Landhal and Herrmand (1949):

$$\eta_I = \frac{\psi_{I-1}^3}{\psi_{I-1}^3 + \psi_{I-1}^2 + 0.22} \quad (3.2.6)$$

Figure 22 shows a comparison between the analytical solution by Ranz and Wong (equation(3.2.4)) to the empirical relation by Landhal and Herrmand (equation(3.2.6)). Here the single target efficiency is plotted as a function of the separation number $\psi_{I-1}^{1/2}$

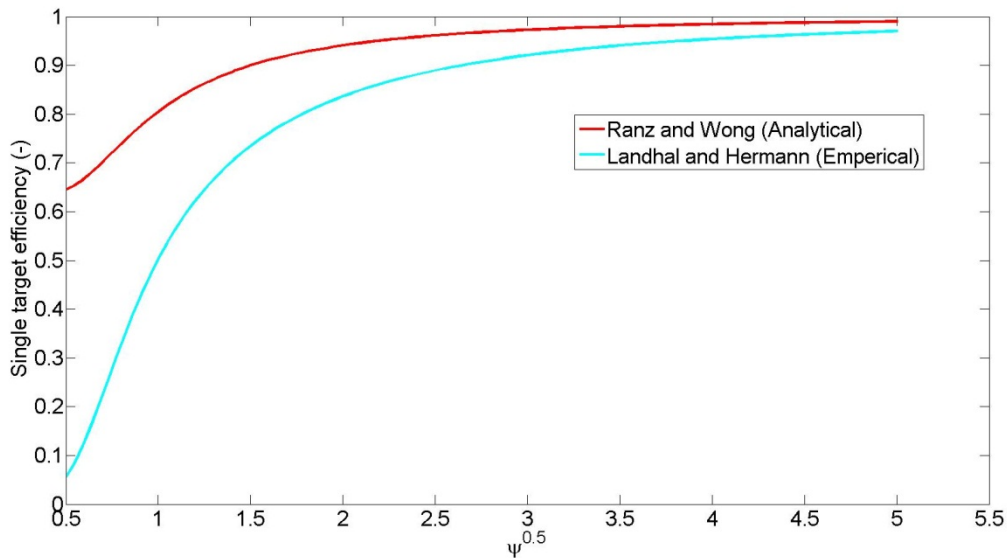


Figure 22 Comparison between the analytical approximation by Ranz and Wong to the empirical relation developed by Landhal and Herrmand.

The difference between the empirical and analytical approximations is significant. And knowing that the empirical relation is known to give better results, it will benefit us to use this expression for the single target efficiency instead of the Ranz and Wong approximation.

Based on the simplification by Ranz and Wong it is therefore conclude that under normal operational condition the centrifugal force can be neglected. And therefore the empirical relation by Landhal and Herrmand will be a good model for the single target efficiency for spinning mesh when the $\bar{a}_c < 1 \times 10^{-3}$.

Up until now the gas is assumed to completely follow the mesh spin. In the scenario of gas flow not following the mesh the relative velocity difference between the flow and the mesh is assumed to increase the capture efficiency. This case is most easily applied in the model for overall droplet capture.

3.2.2 Overall droplet capture

An expression for the overall separation efficiency was presented in an article by Carpenter and Othmer (1955). The method they applied was to divide the meshpad into several layers, illustrated in Figure 23. They also assumed uniform particle size, no re-entrainment, no liquid hold-up and uniform distribution of particles between layers (Helsør, 2006).

Carpenter and Othmer (1955) then started by defining the fraction of particles escaping one single layer as

$$\zeta = 1 - \frac{\eta_{ST}}{c} \quad (3.2.7)$$

Here η_{ST} is the single target capturing efficiency. In this paper η_{ST} refers to the separation efficiency due to inertial impaction ($\eta_{ST} = \eta_I$) described by equation (3.2.6)

Because of the assumption that each layer in the separator has the same removal efficiency, the fraction of particles escaping a layer can be summed across all layers. Therefore, fraction of particles escaping the separator equals the fraction of particles escaping a single layer raised to the power equivalent to the number of layers in the separator.

$$\zeta_t = (1 - \eta_T) = \left(1 - \frac{\eta_{ST}}{c}\right)^{N_z} \quad (3.2.8)$$

$$\eta_T = 1 - \left(1 - \frac{\eta_{ST}}{c}\right)^{N_z} \quad (3.2.9)$$

Here c is a modifying constant defined by Carpenter and Othmer (1955) as (Helsør, 2006):

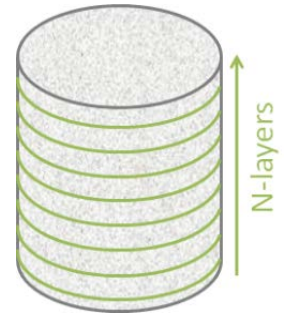


Figure 23
Illustration of how
Carpenter and
Othmer (1955)
divided the
meshpad. Here the
green lines
represent the
different layers.

$$c = \frac{N_z \pi r^2}{F l_w d_w} = \frac{N_z S_{mesh} h}{F \pi} \quad (3.2.10)$$

Carpenter and Othmer (1955) measured the factor F to be $2/3$ (Helsør, 2006) and S_{mesh} is the surface area of the mesh. This specification is provided by the manufacturer described in section 3.4.

The overall efficiency then becomes

$$\eta_T = 1 - \left(1 - \frac{\eta_{ST}}{N_z} S_{mesh} \frac{2h}{3\pi}\right)^{N_z} \quad (3.2.11)$$

One alternative way to write this expression is to insert the distance between each layer, z , by realizing that $z = h/N_z$. This was done by Brunazzi and Paglianti (1998). If the number of layers is large, the expression can be rewritten using (Helsør, 2006):

$$\exp(x) = \lim_{n \rightarrow \infty} \left(1 + \frac{x}{n}\right)^n \quad (3.2.12)$$

The expression then becomes:

$$\eta_T = 1 - \exp\left(-\frac{2\eta_{ST} S_{mesh} h}{3\pi}\right) \quad (3.2.13)$$

This is the expression that has been derived previously for capturing efficiency of a fixed mesh. In the modeling for a spinning mesh, equation(3.2.13) is extended further by assuming the gas does not follow the mesh. This indicates that it is a tangential velocity difference between the mesh and the gas flow, thus the mesh is spinning through the fluid. This in turns means that for every layer the flow goes through in the z -direction it also goes through several separation layers in the θ -direction (see Figure 24).

The relation between the numbers of layers it travels through in the θ -direction for every layer in the z -direction depends on the relative velocity difference of the spinning mesh and fluid, and can be expressed as follows:

$$\frac{N_\theta}{N_z} = \frac{z}{u_z} (\omega r - u_\theta(r)) \quad (3.2.14)$$

Hence the total number of levels it goes through in the θ -direction depends on the distance from centrum (r). An average value can be found by integration and division over the total radius, R_w :

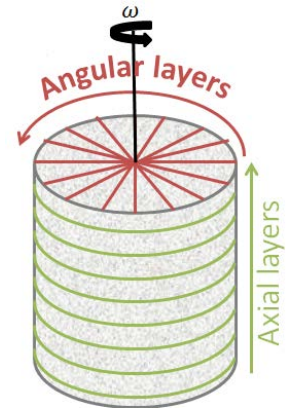


Figure 24
Illustration of layers
in a spinning mesh

$$\frac{1}{R_w} \int_0^{R_w} \frac{z}{u_z} (\omega r - u_\theta(r)) dr = \frac{z}{u_z} \left[\omega \frac{R_w}{2} - \frac{1}{R_w} \int_0^{R_w} u_\theta(r) dr \right] \quad (3.2.15)$$

Thus the expression for the overall efficiency becomes:

$$\eta_{CT} = 1 - \exp \left(- \frac{2 \eta_{ST} S_{mesh} h \left(1 + \frac{1}{u_z} \left[\omega \frac{R_w}{2} - \frac{1}{R_w} \int_0^{R_w} u_\theta(r) dr \right] \right)}{\pi} \right) \quad (3.2.16)$$

This is the proposed model for droplet capturing efficiency in a spinning meshpad. It is assumed that capturing of the droplets is the initial separation mechanism in the NNGLseparator it is therefore implemented as described in Figure 18. "

For η_{ST} in equation (3.2.16), the inertial impaction efficiency described by equation (3.2.6) is used. And for S_{mesh} , the approximation $10.4 + 1.1 \cdot \rho_{rel}$ is used. This approximation is later described in section 3.4. $u_\theta(r)$ is the tangential velocity of the swirl flow. Hence to solve the expression for total capture efficiency (equation(3.2.16)) we need to know the velocity profile inside the meshpad. However with our previous assumption of a gas velocity equal the meshpad velocity, it is fair to assume that the capture efficiency of a spinning mesh will equal that of fixed mesh. And in this case, the overall capturing efficiency from equation (3.2.16) equals equation(3.2.13).

3.2.3 Time of flight model

For the remaining small droplets which are not captured by the mesh, separation will occur through centrifugal forces. The best approach to model this process is through a modified version of the time of flight model, described in section 2.5.1, which includes the porous structure.

We will start by assuming that the swirl flow inside the mesh follows the pure forced vortex, with same velocity as the spinning mesh (ωr).

Applying this to equation 2.2.2 gives the following expression:

$$\frac{dr}{dt} = u_r(r) = \frac{D_p^2 (\rho_l - \rho_g) r \omega^2}{18 \mu_g} \quad (3.2.17)$$

Equation (3.2.17) represents the radial velocity of a particle inside a forced vortex. This equation needs a modification in the case of the

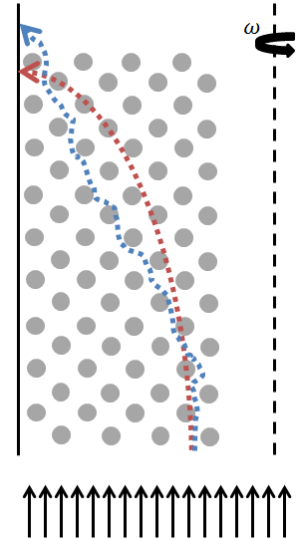


Figure 25 Illustration how the droplet' flight path with mesh (blue arrow) and without (red arrow).

NNGLseparator. It is assumed that the porous material will interrupt its flight path, making it more broken or crooked, illustrated by the blue arrow in Figure 25.

Hence the time for the particle to reach the wall with a mesh present is assumed to be higher than without. This is included in our model by multiplying equation (3.2.17) with a β -factor, where $0 < \beta < 1$.

$$\left(\frac{dr}{dt}\right)_{mesh} = \beta \cdot \left(\frac{dr}{dt}\right)_{no\ mesh} \quad (3.2.18)$$

Assuming a uniform inlet flux we can apply the same procedure as was explained in the literature review, with the inclusion of the modifying β -factor. The expression for the liquid droplet which will be capture with $x\%$ efficiency then becomes:

$$D_{px} = \left[\frac{18\mu_g \ln\left(\frac{R_w}{R_{x\%}}\right)}{\beta(\rho_l - \rho_g)\omega^2 t_{axial}} \right]^{0.5} \quad (3.2.19)$$

If we neglect gravity and approximate the gas velocity by equation (2.3.1) the following expression for t_{axial} is obtained

$$t_{axial} = \frac{h\varepsilon}{U_{sup}} \quad (3.2.20)$$

Inserted into equation (3.2.19) gives

$$D_{px} = \left[\frac{18\mu_g \ln\left(\frac{R_w}{R_{x\%}}\right) U_{sup}}{\beta(\rho_l - \rho_g)\omega^2 h\varepsilon} \right]^{0.5} \quad (3.2.21)$$

Equation (3.2.21) contains the ratio between the radius of the mesh (R_w) and the inlet radius ($R_{x\%}$) needed to separate droplet of size D_{px} or larger. Assuming uniform distribution of droplets across the mesh area, $A\%$ of the droplets will enter at

$$A\% = \frac{\pi R_{x\%}^2}{\pi R_w^2} = \frac{R_{x\%}^2}{R_w^2} \quad (3.2.22)$$

Then all droplets that undergo a radial displacement of $R_w - R_{x\%}$ will be separated with $1 - A\%$ efficiency. Thus,

$$\eta_c = 1 - \frac{R_{x\%}^2}{R_w^2} \quad (3.2.23)$$

Then,

$$R_{x\%} = R_w \sqrt{1 - \eta_c} \quad (3.2.24)$$

Inserting equation (3.2.24) into equation (3.2.21) gives

$$D_{px} = \left[\frac{18\mu_g \ln\left(\frac{1}{\sqrt{1 - \eta_c}}\right) U_{sup}}{\beta(\rho_l - \rho_g)\omega^2 h \varepsilon} \right]^{0.5} \quad (3.2.25)$$

Giving us the following expression for centrifugal separation as a function of droplet size

$$\eta_c = 1 - \frac{1}{\left[\exp \frac{D_p^2 \beta(\rho_l - \rho_g)\omega^2 h \varepsilon}{18\mu_g U_{sup}} \right]^2} \quad (3.2.26)$$

This is the proposed model for centrifugal separation with a meshpad. Here ε is the mesh porosity. And β is a proposed parameter representing the reduction in the droplet's radial velocity due to the obstructing mesh. β is assumed in the range 0.7-1.0.

3.2.4 Results and discussion

Droplet capture

In the derivation of equation (3.2.2) and (3.2.3) describing droplet trajectory around a cylinder, the y-variable was nondimensionalized with the radius of the target. It was then stated that the inlet position causing the droplet to just touch surface of the target would determine the capturing efficiency (Helsør, 2006). In Figure 26 you can see an illustration of how the droplet capture was calculated. Where the blue droplet shows the trajectory of the droplet that is regarded as 100% captured, and red the trajectory of a droplet regarded as 0% captured.

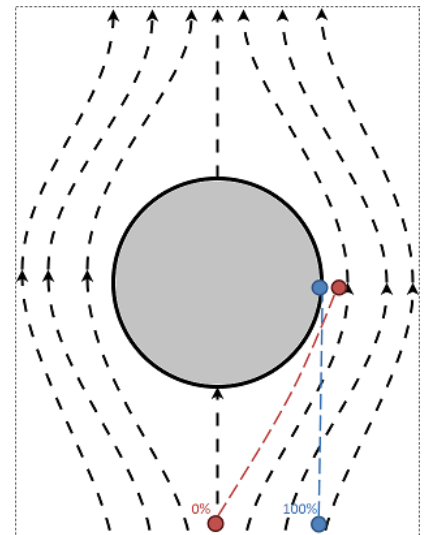


Figure 26 Illustration of single target capturing

When centrifugal force is included in the model however,

there exists trajectories where the droplet can enter beyond the 100% line and still touch the target. Hence we will get droplet capture above 100%.

Despite the fault in the model, we still feel it is good enough to analyze how the centrifugal force impacts the single target efficiency. Therefore, our conclusion that the centrifugal force has little effect, and can be disregarded under normal conditions, still stands.

Time of flight model, β -factor

In our proposed time of flight model (equation (3.1.21)) a β -factor was suggested explained through equation(3.2.18). We have not been able to relate this factor to any mesh properties, and hence regard it to be any empirical factor that needs to be found experimentally. It should be clarified that the factor is regarded to be related to the mesh structure.

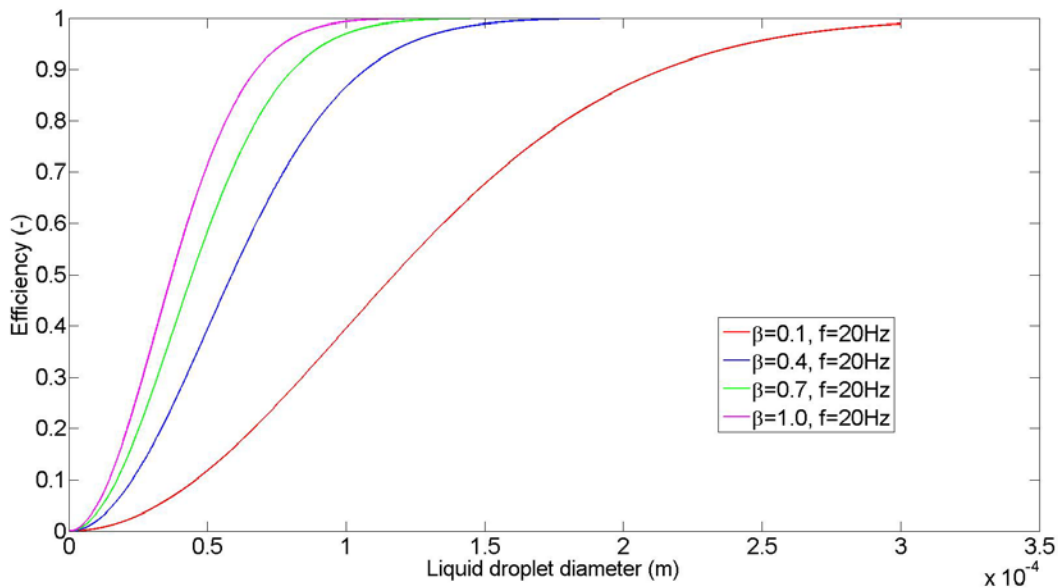


Figure 27 Comparison of droplet separation efficiency through the time of flight model for different β -factors

In Figure 27 the droplet separation efficiency is compared for different β values. From this comparison, the impact of this parameter is shown to be very small. Even with a value of 0.4 for β the separation efficiency is 100% for droplet diameters less than $20 \mu\text{m}$. The β needs to be as small as 0.1 before it will have a significant impact on the efficiency. Based on our assumption that this factor represents a mesh structure obstructing its path, we assume this factor to be far higher than 0.1. A measurement of this factor through experiments is therefore regarded a challenge, since it is assumed to have a very small effect.

Cyclonic separation compared to mesh captures of liquid droplets

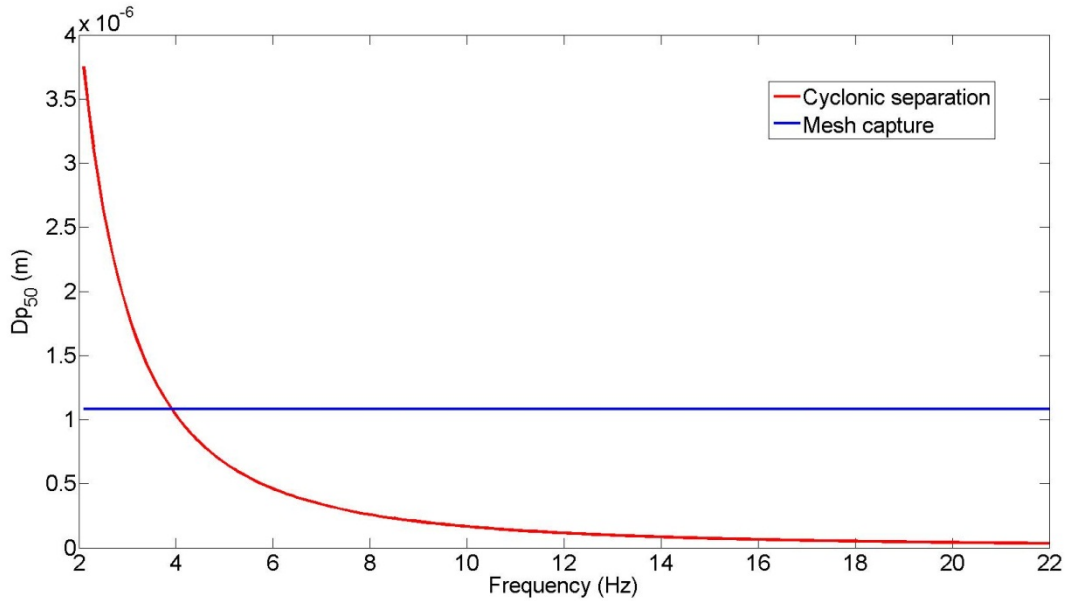


Figure 28 Droplet separated with 50% efficiency as function of frequency. Droplet capture by mesh with 50% efficiency is inserted as reference (blue line).

Figure 28 shows a plot for the droplet diameter which is separated with 50% efficiency by the time of flight model as a function of the meshpads spin frequency (f). The droplet diameter which is capture with 50% efficiency is included as comparison.

The comparison shows that it does not require much spin before cyclonic droplet separation excides droplet capture, in terms of efficiency. Although the plot in Figure 28 is only valid for a specific simulation scenario⁴, considering that 20Hz is the current operational spin it is the cyclonic mechanism that separates the smallest droplets. The separation performance of the NNGLseparator is therefore determined by the time of flight model (equation(3.2.26)).

3.3 Pressure drop

3.3.1 Introduction

Modeling of pressure drop across porous media in the NNGLseparator opposes some real challenges.

⁴ We have here simulated an air and water mix at standard atmospheric conditions, $K=0.5$ and Mesh A dimension. Values and explanation of this simulation description is given chapter 4

First, the introduction of centrifugal force will cause a radial displacement of the fluid. This again results in a cross sectional pressure gradient in the flow.

Second, the fluid does no longer move in a straight path. In addition to the axial velocity vector we have a tangential velocity vector do to the swirl flow created by the spinning meshpad.

And lastly, because of the capturing tank surrounding the filter element, the NNGLseparator does not have clear boundaries. Solving the governing equations requires clear boundary conditions, and without a solution to these equations we cannot predict the flow.

This last problem of unclear boundaries is particularly challenging. With the use of commercial codes such as Fluent one is able to numerically simulate flow from the inlet in the NNGLseparator to the capturing tank. And there are also suggested models on how to numerically simulate flow through porous media (Lage & Merrikh, 2005). But a good numerical simulation of the separator will require that the interface between porous and non-porous is also modeled. If we further add spin to the interface, and two phases to the fluid, the complexity of the problem becomes redundant.

Modeling of pressure drop across the NNGLseparator therefore requires an approximation to its design. And we assume that the NNGLseparator can be approximated by removing the surrounding tank and replace it with no slip wall boundaries. This gives a well posed problem and enables us to analyze the first and second problem (this was also described in section 3.1, see Figure 19).

This section includes a comparison between the two models reviewed in the literature review study to experimental data. The appropriate model based on the comparison is applied to analyze how the first and second problem affects the pressure drop by reviewing dry flow through the separator. Based on this analysis a new modeling approach is suggested for the particular case of the fluid not following the spin of the mesh. Further, pressure drop across wet meshpads is reviewed, and difference between liquid hold up in the NNGLseparator and conventional meshpad demisters is analyzed.

3.3.2 Dry flow

a) Comparing the Blake and Hazen-Dupuit-Darcy equation to experimental data

The two expressions for pressure drop reviewed in the literature section are based on two different modeling approaches. To see which expression best represents the meshpad used in the NNGLseparator, the two expressions are compared to experimental data.

The experiments were done prior to this project. They consist of data for pressure drop across the mesh when used in a conventional method and pressure drop when used as a fixed filter element inside the NNGLseparator. Although the surrounding tank is the only thing that separates these two experiments, they gave different results. A simple illustration of the two experimental setups can be seen in Figure 29.

The exact conditions during the experiments and the confidence interval for the data are unknown to the author. Hence the comparison done in this section should be regarded as an estimate. This is especially the case for the experiments done on the rig with the separation tank (Figure 29 b), where the values could not be verified⁵.

Plots comparing the model to the experimental values can be seen in the bottom of this section (Figure 30, Figure 31, Figure 32 and Figure 33)

In Figure 30 the Hazen-Dupuit-Darcy equation is compared to the experimental data for the conventional separator illustrated in Figure 29 a. The plot shows no significant spread between the modeled and the experimental values, thus the quadratic analogy between the gas velocity and the pressure drop proposed in the model can be regarded a good fit.

In Figure 31 the model is compared to the experiments for the separator with the capturing tank. Although the spread is larger than the comparison in Figure 30, it is still acceptable. However as mentioned there is an uncertainty in the values measured in the separator rig with the capturing tank. And due to this uncertainty, the values for the conventional separator are assumed to best represent the pressure drop.

In Figure 32 modeling with the Blake expression is compared to the experimental results for the conventional separator rig, where the error bar represents variation in the model. The large variation in the modeling results comes from the uncertainty in relative density given by the manufacturer for the meshpad, specified to be between 6% and 10%. But even with this large

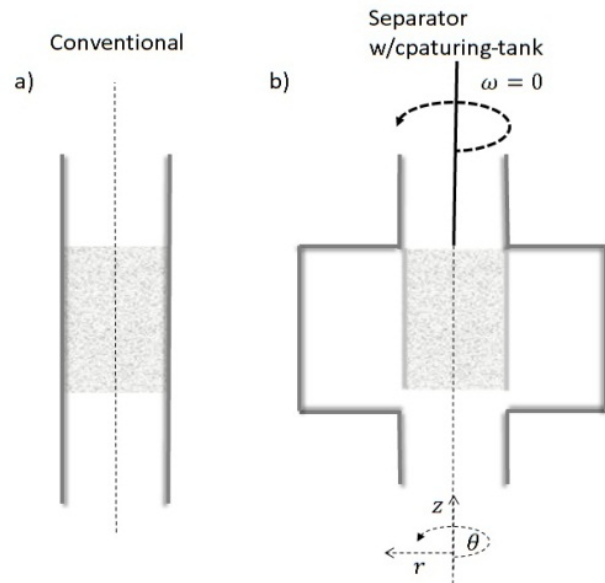


Figure 29 Comparison between the experiment for the use of the meshpad in conventional technologies (a), and experiments of meshpad used in the NNGLseparator with surrounding capturing tank (b).

⁵ The measured values were lower than expected, which could not be explained.

spread the model does not manage to include the experimental results. Further comparison, to the experiments for the separator with the capturing tank, shows an even larger spread between experiment and model (see Figure 33). So given that the manufactures specifications are correct, modeling through the Blake expression is not valid for this particular meshpad (see section 3.4 for further information on the meshpad specifications).

The model that shows the best results is thus the Hazen-Dupuit-Darcy equation. This is unfortunate since modeling by the Hagen-Poiseuille flow analogy used in the Blake expression means that we do not need to determine the permeability and the form coefficient when changing mesh specifications such as the porosity.

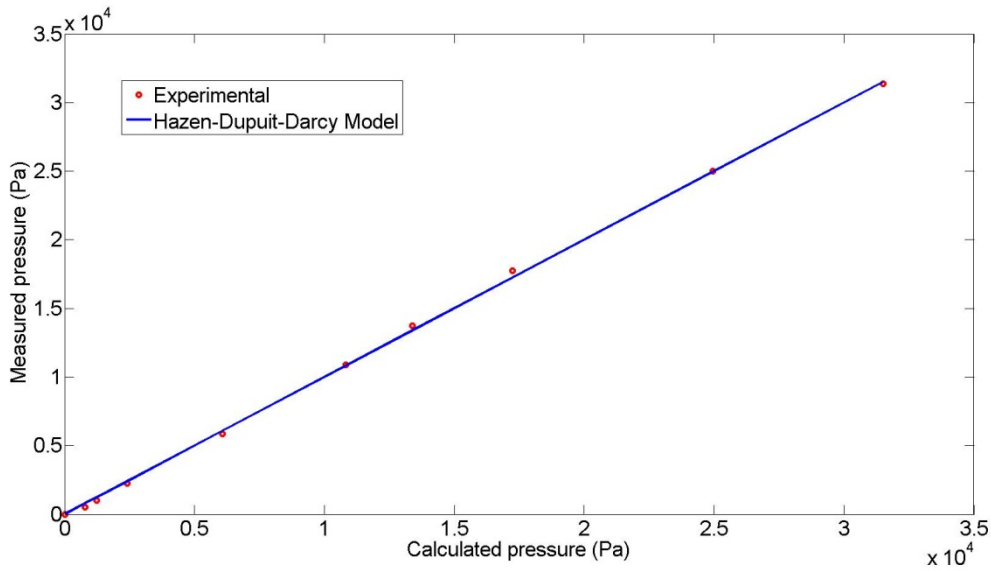


Figure 30 Modeling through the Hazen-Dupuit-Darcy equation compared to the experimental data for the conventional separator.

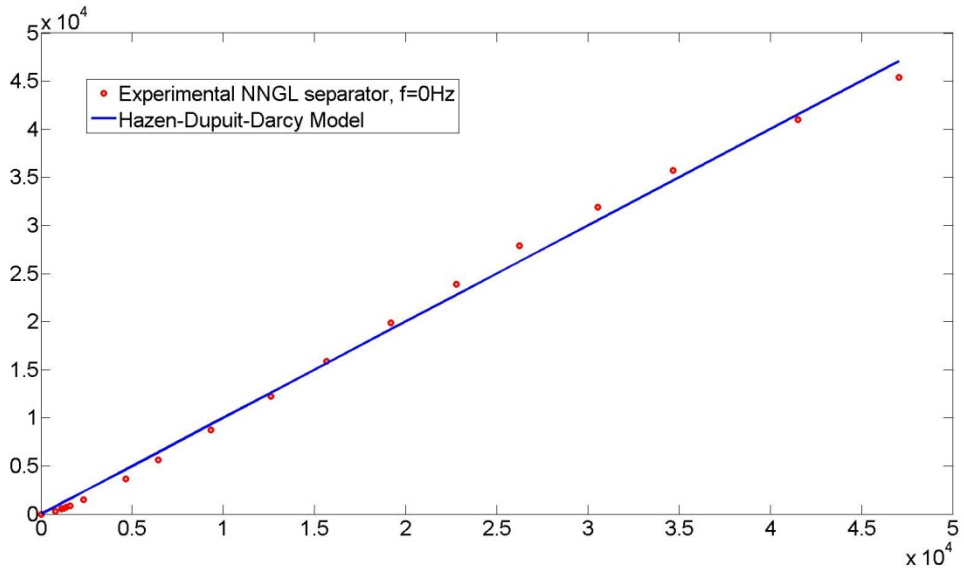


Figure 31 Experimental results of pressure drop across the NGLseparator with the inclusion of separating tank, compared to the Hazen-Dupuit-Darcy equation.

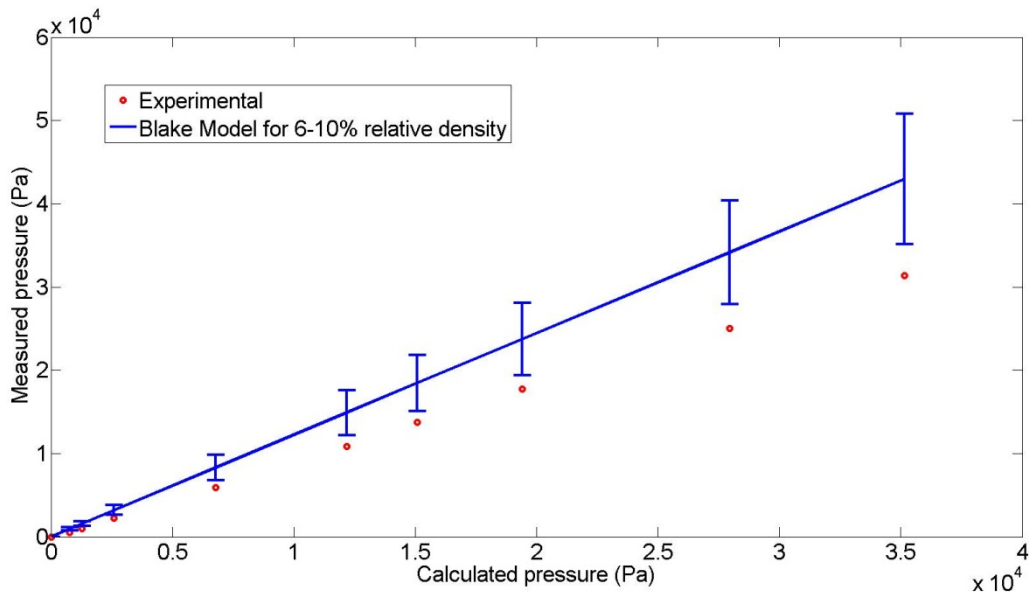


Figure 32 Comparison of modeling by the Blake expression to experimental values. The error bar comes from the uncertainty in the relative density of the mesh

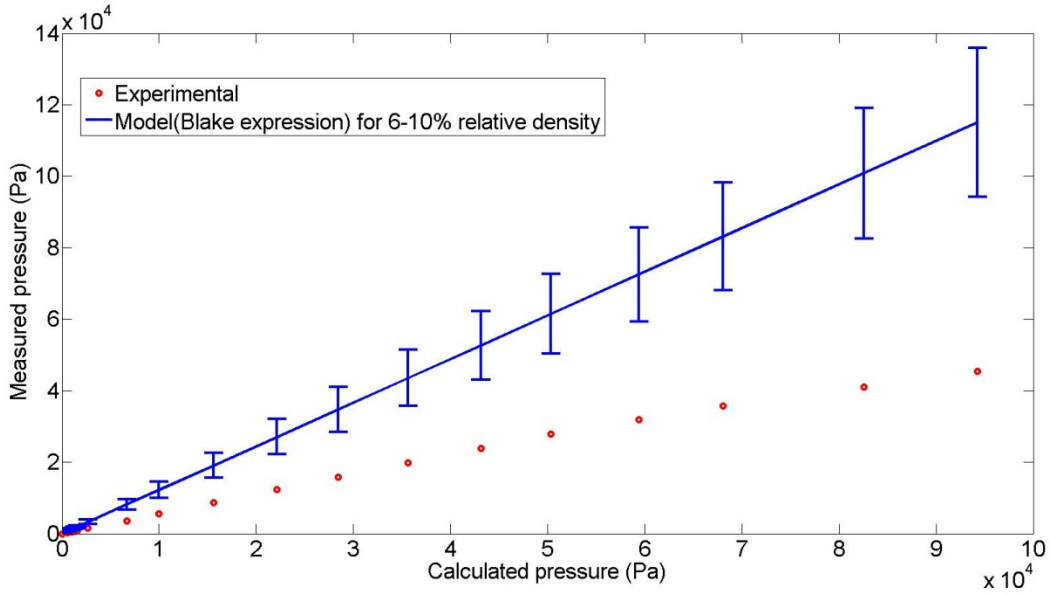


Figure 33 Experimental results of pressure drop across the NGL separator with the inclusion of separating tank, compared to the Blake expression.

b) Spinning mesh

To determine if the Hazen-Dupuit-Darcy equation is valid when the meshpad is spinning two scenarios are proposed to base our analysis on. These are illustrated in Figure 34.

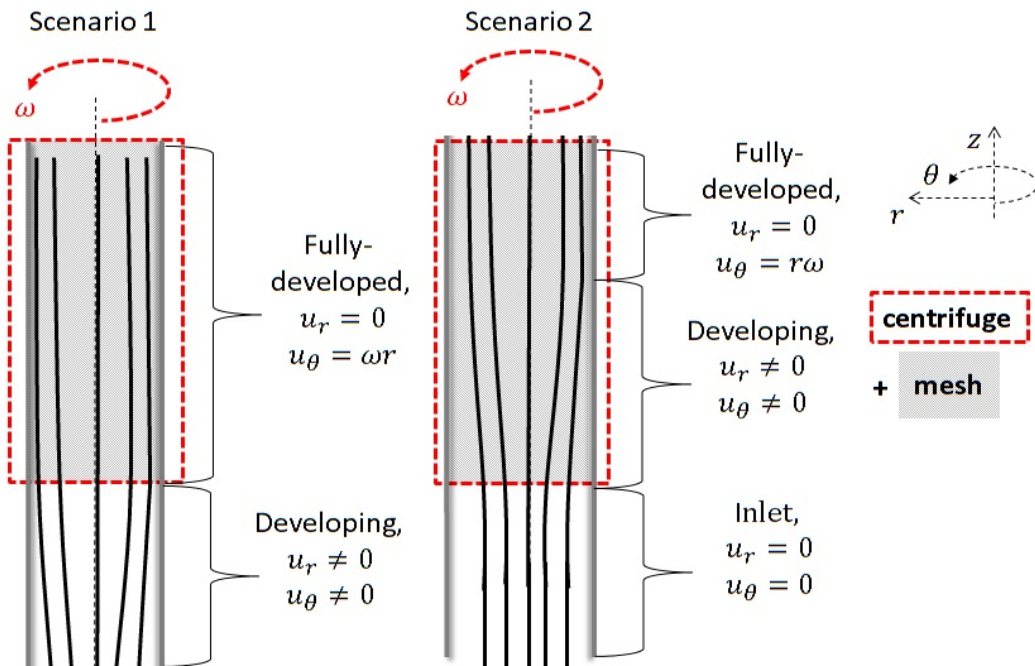


Figure 34 The two scenarios applied in the analysis for the Hazen-Dupuit-Darcy equation validation for spinning mesh.

In Scenario 1 the flow is assumed to be fully developed before entering the mesh. This scenario enables us to analyze the flow properties effect on the pressure drop. Because the flow is a fully developed forced vortex flow, the flow properties can be calculated through the governing equation. The difference between rotating and non-rotating flow can then be studied, and there effect on the pressure drop can be analyzed.

In Scenario 2 the fluid is assumed to develop inside the mesh. Here our focus points can be divided into two parts. First we will study how the radial displacement occurs inside the mesh. How this radial displacement affect the pressure drop is then analyzed.

The second part of Scenario 2 is how a tangential velocity difference between the meshpad and the flow affects the pressure drop.

Scenario 1: Fully developed before entering the meshpad

First we assume that the flow is exposed to the centrifugal field before entering the mesh and then maintain this flow through the mesh. The equation that needs to be analyzed together with the Hazen Dupuit-Darcy Equation is the momentum equations describing fully developed flow in a centrifugal field.

Through the Navier-Stokes equation it can easily be seen that the axial velocity profile $u_z(r)$ is not affected by the centrifuge (the Navier-Stokes equation is cited in Appendix B). Therefore, focus is put on how changes in the cross sectional area interfere on the conventional models.

By combining the boundary conditions with the continuity equation, the following conditions can be derived for fully developed forced vortex flow inside a centrifuge.

$$u_r = 0, \quad u_\theta = r\omega \quad \text{and} \quad \frac{\partial u_z}{\partial z} = 0 \quad (3.3.1)$$

Given the assumption above, the radial pressure difference in a centrifugal field can by derived from the momentum equation:

$$\frac{\partial P}{\partial r} = \rho \frac{u_\theta^2}{r} = \rho_g r \omega^2 \quad (3.3.2)$$

$$\Delta P(r) = \frac{1}{2} \rho_g (r\omega)^2 \quad (3.3.3)$$

Here $\Delta P(r)$ represents the pressure difference from the center.

Through experiments Helsør (2006) concluded that the pressure drop across the mesh for both high and low pressure flow, is equally depended on the properties of the mesh. The Hazen-

Dupuit-Darcy equation is therefore valid in both cases (Helsør, 2006). In other words, the radial pressure difference itself does not require a modification of the form and permeability factor.

Any effect the pressure difference has on the density of the gas can also be neglected. Here higher pressure at the walls consequently results in lower pressure in the center. And through conservation of mass one observes that an increase in density at high pressure zones gives equal decrease in density at low pressure zones.

Scenario 2 a: Radial displacement inside the mesh

The second approach is to assume that the flow is not influenced by the centrifugal field before entering the mesh, hence $U_\theta = 0$ and $U_r = 0$ at the inlet. The fluid is then developing inside the mesh, and it is this region that becomes the focus for our analysis. Here the radial displacement inside the mesh effect on the pressure is analyzed first.

To attack this problem an infinitely long spinning meshpad is imagined. Focus is then put on the fully developed region (see Figure 34); by applying the porous continuum model (see section 2.4). Converting the porous continuum equation (2.4.2) into cylinder coordinates gives the following term for the radial pressure⁶:

$$\frac{\partial p}{\partial r} = \rho_g r \omega^2 - \frac{\mu_{eff}}{k} u_r - \rho_g C_p u_r^2 \quad (3.3.4)$$

Applying the condition for fully developed flow ($u_r = 0$) gives:

$$\frac{\partial p}{\partial r} = \rho_g r \omega^2 \quad (3.3.5)$$

This is the same radial pressure field as was derived in equation(3.3.3). What these two expressions represent can be seen in Figure 35.

The theory on why there is no difference in the radial pressure gradient comes from how it is induced. The rotation is induced by a motor set to constant rotational speed. This is mathematically included in our analysis by setting $u_\theta = r\omega$. The motor is then assumed to overcome any pressure drop that might occur due to radial movement inside the mesh. This will then be reflected in the effect required by the motor. Here it is assumed that an increases effect is required for mesh types with same relative density, but higher form or drag coefficient.

⁶ the transformation of porous continuum equations from general to cylindrical coordinates can be seen in Appendix B

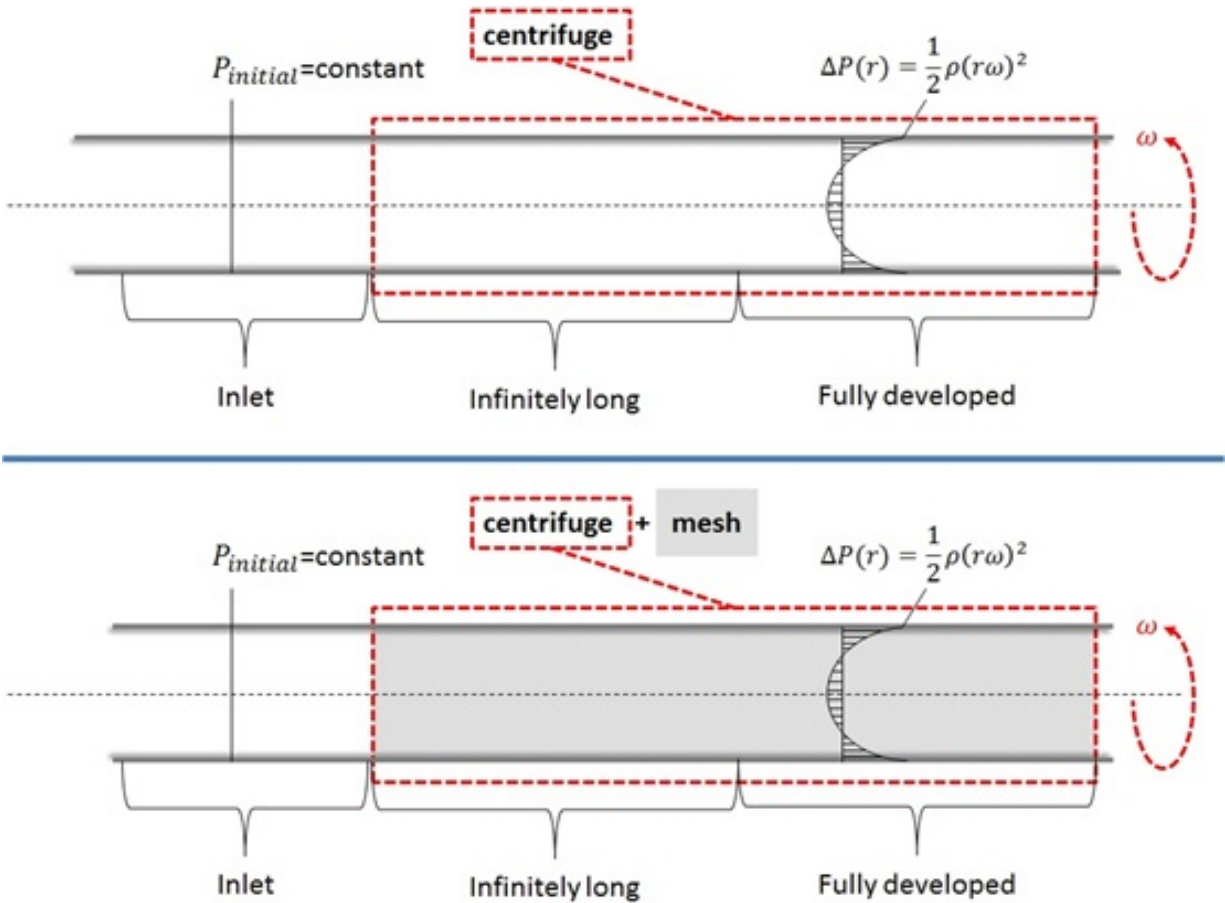


Figure 35 Illustration between flow in a centrifuge and flow in centrifuging mesh. This comparison is used to show that the pressure drop in axial direction is not affected by the centrifugal effect when the forced vortex assumption is made.

Scenario 2 b: $U_\theta \neq 0$

It is generally accepted that pressure drop across porous media increases with the height. And Darcy was the first to realize it was linearly dependent (Helsør, 2006). In the models proposed after Darcy the pressure drop is still seen to be given as per height ($\Delta P/h$, see section 2.3.1). Height in these models can also be represented as the fluid *traveling distance* through the mesh, hence it can also be written as $\Delta P/\text{traveling distance}$.

This *traveling distance* becomes important when the fluid has a relative velocity difference compared to the porous media. Seen from the spinning mesh point of view the flow then swirls around the center with a velocity equal to $2\pi r\omega - u_\theta(r)$. When this occurs as the fluid flows through the mesh the *traveling distance* increases and should be included in the pressure drop model.

Our proposed model approach is to divide the mesh into layers, similar to the approach given in section 3.2.2.

Figure 7 shows the distribution of layers, with N_z layers in the axial direction, and N_θ layers in the angular direction. The distance between the layers are z in the axial and θ in the angular.

If the layers are proposed to be uniformly distributed, the distance between each layer by the height and the circumference can be expressed as

$$z = \frac{h}{N_z} \quad \theta = \frac{2\pi r}{N_\theta}$$

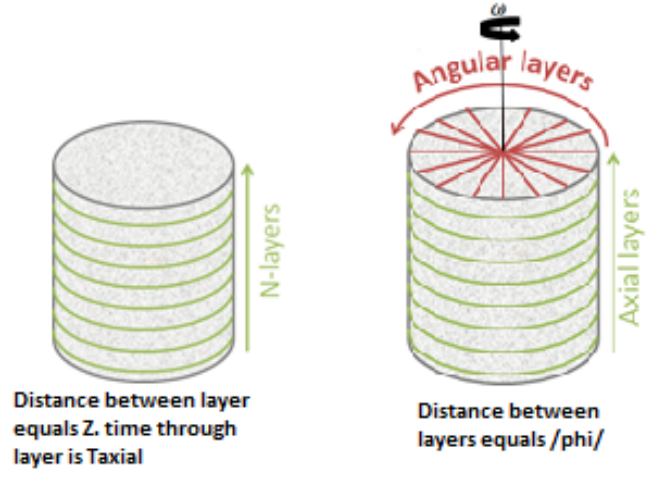


Figure 36 Illustration of modeling by layers

By focusing on one layer in the axial direction, a term for the time it takes to travel through that layer (t_z) can be composed as

$$t_z = \frac{z}{u_z}$$

By expressing the velocity difference between the spinning mesh and the swirl flow as $r\omega - u_\theta$, the distance it travels in the angular direction during the time t_z can be expressed as

$$t_z(r\omega - u_\theta)$$

Dividing this by θ gives the number of layers this distance represents. And, the number of angular layers traveled per axial layer

$$\frac{N_\theta}{N_z} = \frac{t_z(r\omega - u_\theta)}{\theta} = \frac{z(r\omega - u_\theta)}{u_z \theta} \quad (3.3.6)$$

The total traveling distance inside the mesh then becomes

$$N_z \cdot z + \frac{N_\theta \cdot \theta}{N_z \cdot z} = h + \frac{(r\omega - u_\theta)}{u_z} \quad (3.3.7)$$

As can be seen in equation(3.3.7), the traveling distance becomes relative to the distance from the center. In the case of small u_θ , the fluid go through a lot more porous media in the outer circumference compare to an inner one. Therefore, to get a one dimensional expression a mean value is proposed. The total traveling distance can then be expressed as

$$h + \frac{(r\omega - u_\theta)}{u_z} = h + \frac{1}{R_w} \int_0^{R_w} \frac{(r\omega - u_\theta)}{u_z} dr = h + \frac{\frac{R_w}{2} \omega - \frac{1}{R_w} \int_0^{R_w} u_\theta dr}{u_z} \quad (3.3.8)$$

Inserting the total distance into the Hazen-Dupuit-Darcy equation gives the total pressure drop

$$\Delta P = \left(\frac{\mu}{K_p} U_{sup} + C_p \rho U_{sup}^2 \right) \cdot \left(h + \frac{\frac{R_w}{2} \omega - \frac{1}{R_w} \int_0^{R_w} u_\theta dr}{u_z} \right) \quad (3.3.9)$$

This is our proposed model for pressure drop where $u_\theta(r)$ is the tangential velocity of the gas flow, K_p is the permeability factor calculated from the fixed mesh experiment to $9.4 \cdot 10^{-8} \text{ m}^2$ and C_p is the form factor calculated to be 131.3 m^{-1} .

3.3.3 Wet pressure drop

When meshpads are used as gas liquid separator, some of the separated liquid will accumulate inside the mesh. This is referred to as liquid hold up and increases the pressure drop across the meshpad.

The only model found for pressure drop across a wet mesh demister is a modified Hazen-Dupuit-Darcy equation including an effective porosity defined by Billet (1995) for packed columns (Helsør, 2006):

$$\varepsilon_{eff} = \varepsilon - H^{total} \quad (3.3.10)$$

Here H^{total} is the total liquid hold up inside the mesh, described as fraction of the total volume. This variable needs to be modeled, and was shown by Helsør (2006) to be a function of the gas load factor. The effective porosity is included to the model by replacing the superficial velocity U_{sup} , with an effective velocity:

$$U_{eff} = \frac{U_{sup}}{\varepsilon_{eff}} \quad (3.3.11)$$

Resulting in

$$\frac{\Delta P_{total}}{h} = \frac{\mu}{K_p} U_{eff} + C_p \rho U_{eff}^2 \quad (3.3.12)$$

To the author knowledge there are no good models developed for liquid hold-up inside mesh demister. The only model found is a power law correlation to the gas load factor suggested by Helsør (2006). The correlation includes 4 empirical coefficients, but any physical relationship to these constants was not found (Helsør, 2006).

To develop a model for the liquid hold-up in the NNGLseparator would therefore be futile without good experimental data to base it on. Instead this section includes an analysis on how liquid holdup in the NNGLseparator differs from the conventional fixed meshpad separator, which can be used as foundation for further work. The analysis is based on some phenomenological aspects occurring when meshpad is used as a demister described by Helsør (2006).

a) Flooding and liquid hold-up conventional fixed meshpad

By placing a control volume around the meshpad one can establish a mass balance between the amount of liquid transported to the mesh (\dot{M}_{in}), the amount of liquid drained from the mesh (\dot{M}_{drain}), the amount of liquid carried over the over the mesh ($\dot{M}_{carryover}$) and the amount of liquid accumulating inside the meshpad ($\dot{M}_{accumulating}$)

$$\dot{M}_{in} = \dot{M}_{drain} + \dot{M}_{carryover} + \dot{M}_{accumulating} \quad (3.3.13)$$

In steady state condition the balance reduces to (Helsør, 2006)

$$\dot{M}_{in} = \dot{M}_{drain} + \dot{M}_{carryover} \quad (3.3.14)$$

The difference between equation (3.3.13) and (3.3.14) is the liquid holdup. Or, the liquid holdup is the total amount of liquid that accumulates inside the mesh from start up to steady state.

In Helsør’s study on conventional meshpad demister he described three different regimes occurring during operation. These are the pre-loading, loading and flooding regime⁷. The pre-loading regimes occurs at low gas velocities when the amount of liquid transferred to the mesh (\dot{M}_{in}) equals the amount drained (\dot{M}_{drain}). At this stage liquid hold up does not increase with increasing gas velocities, but remains static (Helsør, 2006). The loading regime occurs when the gas velocity is increased to the point where the liquid starts to accumulate inside the mesh, increasing the liquid hold-up (Helsør, 2006). And at some point the liquid hold up reaches a peak in which no more liquid can be absorbed by the mesh, and the mesh becomes flooded. The different regimes can be summarized as

$$\left. \begin{array}{l} \dot{M}_{in} \approx \dot{M}_{drain} \\ \dot{M}_{carryover} \approx 0 \\ H^{total} \approx static \end{array} \right\} \text{Pre-Loading}$$

$$\left. \begin{array}{l} \dot{M}_{in} \approx \dot{M}_{drain} \\ \dot{M}_{carryover} \approx 0 \\ H^{total} = increasing \end{array} \right\} \text{Loading}$$

⁷ The description given here differs from Helsør(2006), as he included flooding point and loading point in describing the different regimes. These were deemed irrelevant for this analysis.

$$\left. \begin{array}{l} \dot{M}_{in} \neq \dot{M}_{drain} \\ \dot{M}_{carryover} \neq 0 \\ H^{total} = increasing \end{array} \right\} \text{Flooding}$$

How the different regimes affect the pressure drop across the mesh can be seen in Figure 37. Pressure drop across a dry mesh is included as a comparison.

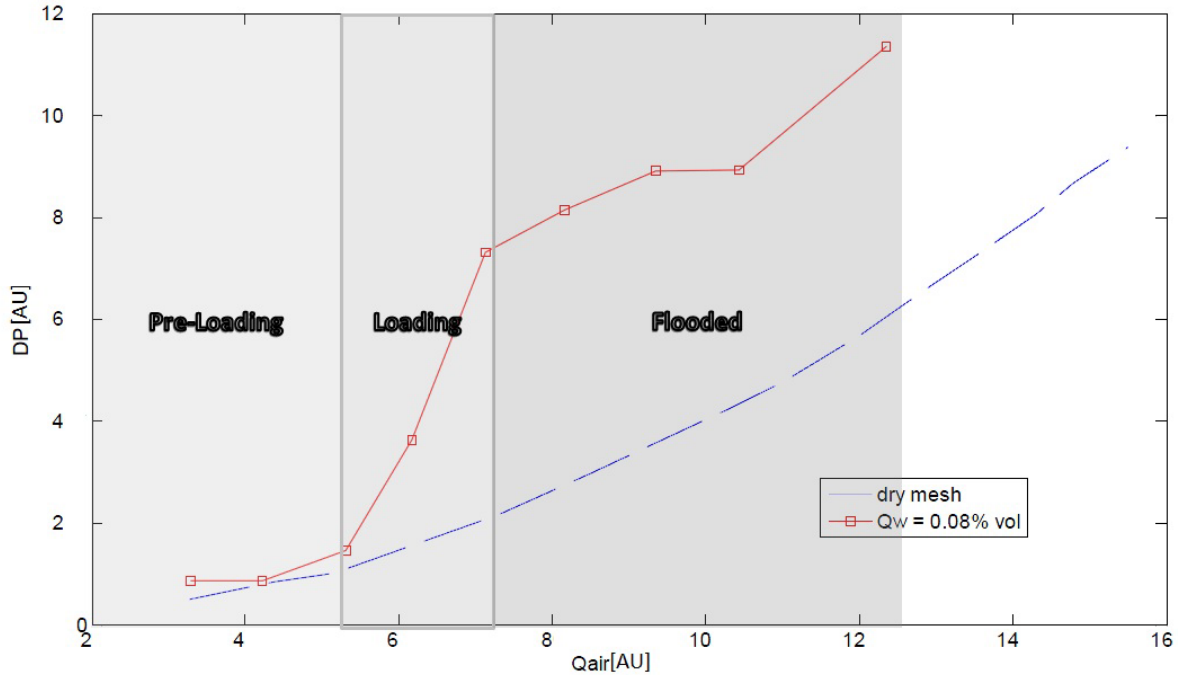


Figure 37 Total and dry pressure drop as function of volumetric air flow. The liquid in this example is water

b) NNGLseparator

A steady state mass balance over the NNGLseparator filter element can be done in the same way as in the previous section.

$$\dot{M}_{in} = \dot{M}_{drain} + \dot{M}_{carryover} \quad (3.3.15)$$

In conventional separators $\dot{M}_{carryover}$ is regarded as the liquid which is not separated by the meshpad. For the NNGLseparator this is assumed to equal the amount which is not captured by the mesh (see section 3.2.2).

The liquid that flows through the meshpad ($\dot{M}_{carryover}$) can be calculated from the capturing efficiency, when assuming that the entrained liquid droplets are of uniform size (D_p)

$$\dot{M}_{carryover} = [1 - \eta_{CT}(D_p)] \cdot \dot{M}_{in} \quad (3.3.16)$$

The connection between the capturing efficiency and the liquid hold-up through the equation above is though only an assumption. And in some cases $\dot{M}_{carryover}$ might be so small that it can be neglected.

Drainage in the NNGLseparator differs from conventional meshpad, in terms of drainage area and drainage force. The drainage area for the NNGLseparator is illustrated in Figure 38.

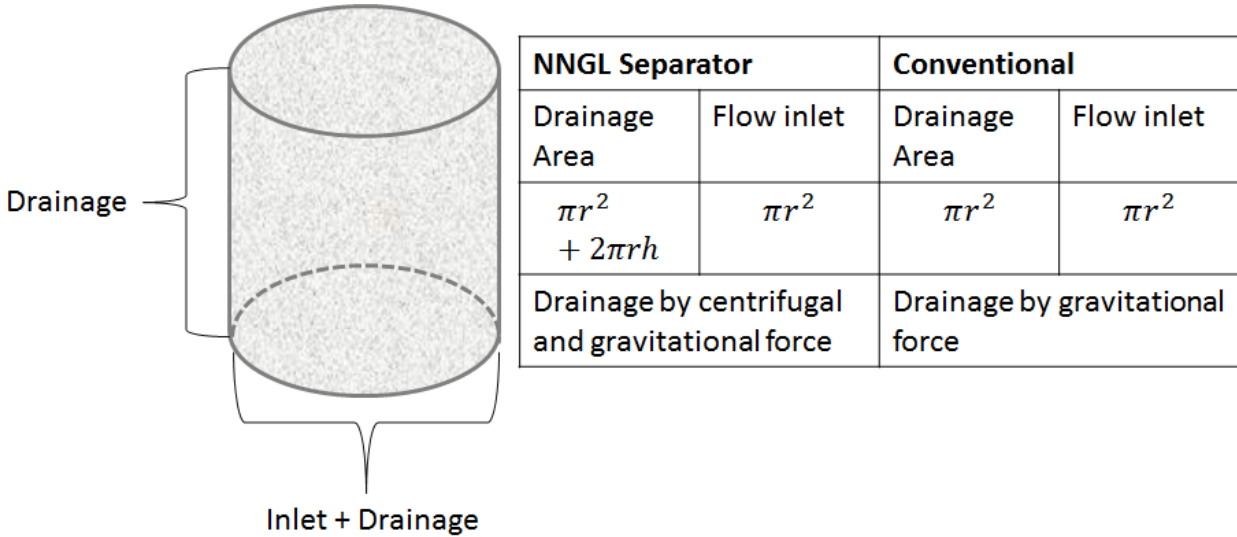


Figure 38 Drainage area in the NNGLseparator compared to the conventional technologies

Figure 38 shows a table that summarized how the NNGLseparator differs in terms of drainage. As well as having a larger drainage area, it also has an extra force in the centrifugal force. The increased area together with the centrifugal force will increase drainage from the mesh. This difference can be seen in the mass balance by converting mass flow in equation (3.3.15) and (3.3.14) into mass fluxes times the respective area.

Conventional:

$$\dot{m}_{in} \cdot \pi r^2 = \dot{m}_{drain-G} \cdot \pi r^2 + \dot{M}_{carryover} \quad (3.3.17)$$

NNGLseparator

$$\dot{m}_{in} \cdot \pi r^2 = \dot{m}_{drain-G} \cdot \pi r^2 + \dot{m}_{drain-C} \cdot 2\pi r h + \dot{M}_{carryover}$$

Here $\dot{m}_{drain-C}$ is the mass flux drained on the sides of the mesh, and $\dot{m}_{drain-G}$ is the mass flux drained on the bottom by gravity.

Because of this increase in drainage, the NNGLseparator can handle much higher gas load factors compared to conventional separators. This has also been shown through experiments comparing the conventional separator with the NNGLseparator. Because of limitations in the current test rig, it has yet been determine at which gas load factor the NNGLseparator reaches the loading and flooding regime. Hence more study and experiments on this subject is required before a complete model for wet pressure drop can be obtained.

3.3.4 Results and discussion

Blake expression

In section 3.3.2a) the Blake expression was shown to be unsuitable as pressure drop model for the meshpad in the NNGLseparator. However the conclusion was based on the relative density specifications from the manufacturer, which is given to be between 6% and 8%. If instead 5% relative density is used for the mesh specifications the model give a good fit to the experiments. A comparison is shown below.

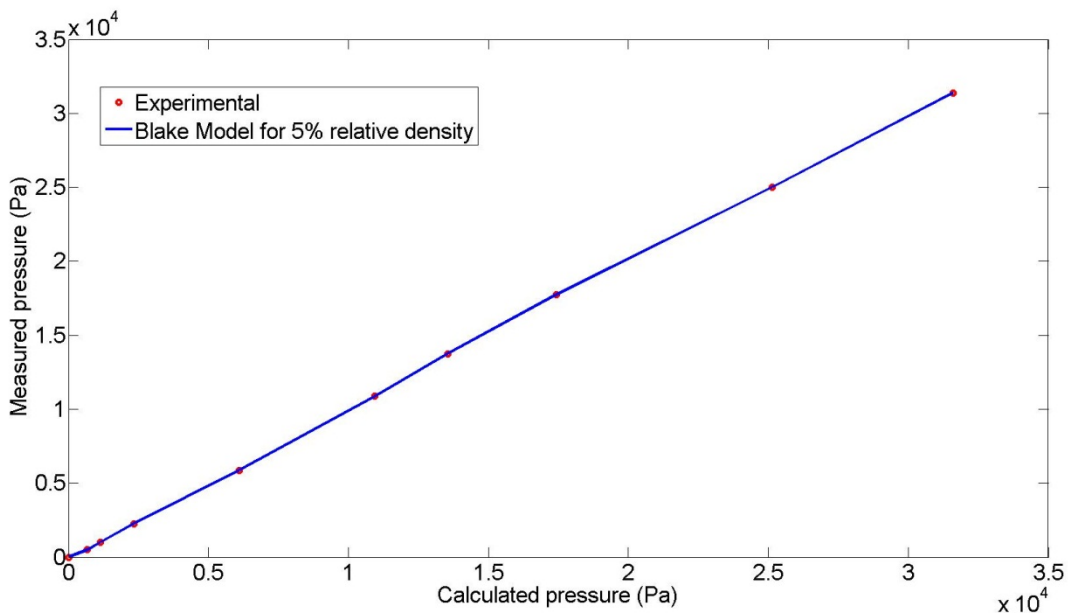


Figure 39 Comparison for the Blake expression for 5% relative density to experimental data

The almost perfect fit seen in Figure 39 gives an indication that it is possible with an analogy between Hagen-Poiseuille flow and pressure drop in the NNGLseparator’s meshpad. The problem is though the manufactures specifications. Here the spread in the density specifications is surly due to uncertainty in their manufacturing process. This might indicate that, for the particular mesh used in the experiments, the specifications were wrong. However the good fit might also be a coincidence. Hence more experiments involving different fluid components are

required. The conclusion is still on the Hazen-Dupuit-Darcy equation to model the pressure drop was made.

Swirl flow: Forced vortex or combined vortex?

An analysis was given in section 3.3.2b) on how developing flow inside the mesh effect the pressure drop. This analysis led to a new equation describing pressure drop, which takes into account a tangential velocity difference between the meshpad and the flow.

The expression did however not give a quantitative description of what the tangential velocity difference is. Instead the tangential velocity was left open as u_θ in equation (3.1.29). This is because it cannot be said for certain how the swirl flow behaves inside the mesh. There is however an assumption that the flow follows the forced vortex characteristics.

Experiments have shown that the pressure drop across the NNGLseparator is not affected by the mesh spin (see Figure 42). Comparing this to equation (3.1.29) indicates that either the flow has the same tangential velocity as the meshpad, or the pressure drop due the velocity difference is neglectable.

To see how much the pressure drop increases when the flow does not follow the mesh, simulation on a simplified combine vortex flow is proposed. The vortex flow follows the forced vortex characteristics to a certain radius R_{top} and free vortex from R_{top} to the wall (R_W).

$$u_\theta(r) = \begin{cases} r\omega & r \leq R_{top} \\ \frac{R_{top}^2\omega}{r} & r > R_{top} \end{cases} \quad (3.3.18)$$

A plot of the velocity function in equation (3.3.18) can be seen in Figure 40. Here the spin is to 20 Hz, and the radius to the wall equals 4.15 cm.

Equation (3.3.18) is not continuously derivative across the domain, thus it is regarded as a simplified version of the combined vortex flow. However the flow gives a good indication on the effect it has on the pressure drop model.

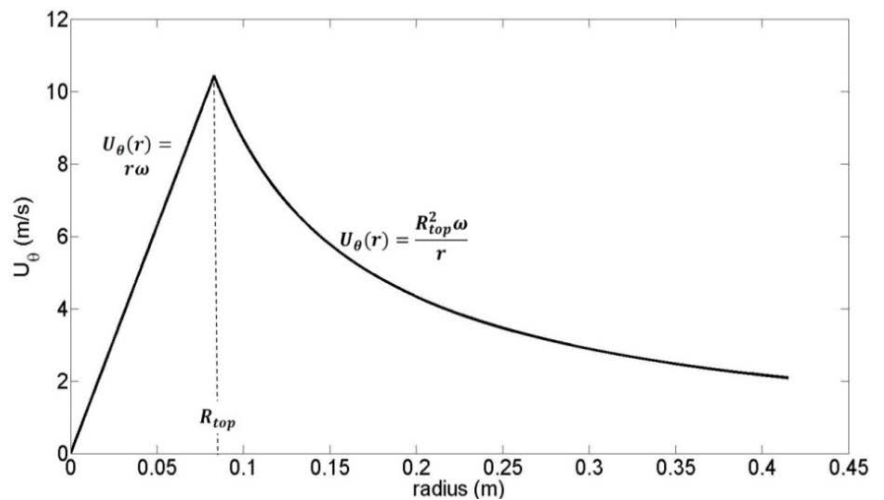


Figure 40 tangential velocity profile of combined vortex flow across the meshpad with a 20 Hz spin frequency

Applying equation (3.3.18) to equation (3.3.9) leads to the following expression for the pressure drop:

$$\Delta P = \left[\frac{\mu}{K_p} U_{sup} + C_p \rho U_{sup}^2 \right] \cdot \left[h + \frac{1}{U_{sup}} \left(\frac{R_w - R_{top}}{2} \omega - R_{top}^2 \omega \ln \left(\frac{R_w}{R_{top}} \right) \right) \right] \quad (3.3.19)$$

The results can be seen in Figure 41, where R_{top} is given as a fraction of the mesh radius (R_w).

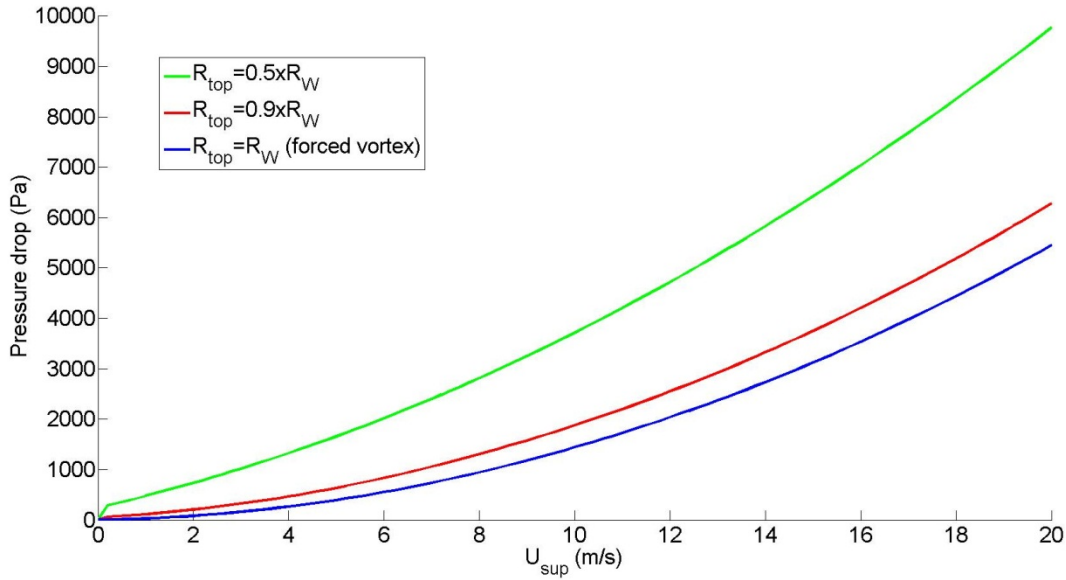


Figure 41 Pressure drop compared for different swirl flows with air at standard atmospheric condition. Mesh spin is 20Hz

Comparing the pressure drop curves in Figure 41 shows that even with R_{top} equaling 90% of the radius the increase in pressure drop is significant and should be measurable in an experiment.

The spinning pressure drop model (equation(3.3.9)) have not been verified, thus the results in Figure 41 is not a proof of the assumption of forced vortex flow. However as long as the reasoning behind the model cannot be unjustified, comparing the model and the experiments adds confidence to the assumption of forced vortex flow inside the mesh.

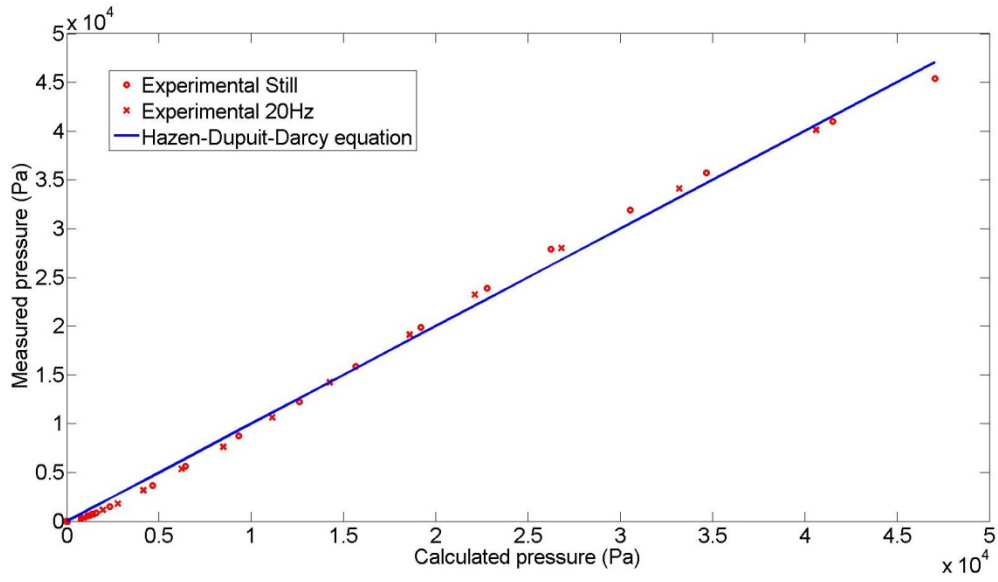


Figure 42 Comparison between experimental data for pressure drop across still and spinning meshpad. The Hazen-Dupuit-Darcy equation is used as reference line

3.4 Meshpad characteristics

The manufactures' meshpad specifications differ from the properties required to use the models proposed in section 3. This section is therefore included to show how to obtain the needed properties for the meshpad.

Surface area

The meshpad used as reference in this thesis is a Duocel® metal foam. The specifics given by the manufacture is the foam's pore density and relative density. Here the pore density is given as pore per inch (PPI), and relative density as percentage of the aluminum density. The surface area of the mesh is given as a graph on the manufactures website, and can be seen in Figure 43 (ERG Aerospace, 2011).

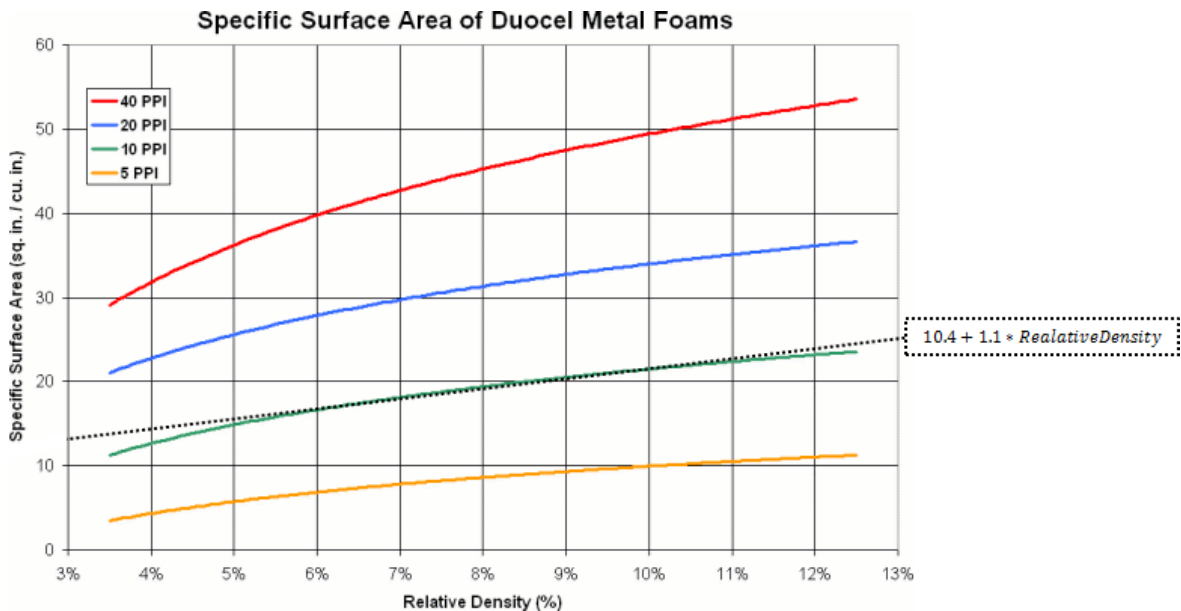


Figure 43 Specific surface area of Duocel metal foams. Graph is taken from ERG Aerospace Corporation (ERG Aerospace, 2011).

It is the 10 PPI Metal foam in Figure 43 that is used as reference in this paper. The mesh specifications given by the manufacture were a relative density of 6-10%. Any function for the specific surface area and relative density was not given by the manufacture. From Figure 43 a linear approximation between 6 and 10% give small errors. This approximation was therefore used in the modeling and can be seen plotted in Figure 43 with a dotted line.

$$S_{mesh} = 10.4 + 1.1 \cdot \rho_{rel} \quad (3.4.1)$$

Porosity

The porosity can be calculated from the relative density as (Helsør, 2006):

$$\varepsilon = [1 - \rho_{rel}] \cdot 100\% \quad (3.4.2)$$

Target diameter

The target diameter (d_f) can be approximated with an equation suggested by Helsør (2006):

$$d_f = \frac{4 \cdot (1 - \varepsilon)}{S_{mesh}} \quad (3.4.3)$$

Helsør(2006) derived the expression with wire mesh demisters as basis, while the particular mesh used in the NNGLseparator is metal foam. Equation (3.3.21) could therefore lead to an error on the capturing efficiency compared to traditional wire mesh demisters.

4 Analysis and Parametric study

In this section we will analyze and perform a parametric study on the pressure loss and separation performance for different design parameters and operating conditions. The study is based on the models proposed in section 3.

4.1 Introduction

In the analysis the scenario of fully developed forced vortex flow is applied in the simulations. The models to represent this scenario are the Hazen-Dupuit-Darcy Equation (equation(2.3.8)) for pressure drop and the modified time of flight model (equation(3.2.26)) for the separation performance. Coefficients calculated from the air-water experiment explained in section 3.3.2a) is applied to the Hazen-Dupuit-Darcy equation. The β -coefficient in the time of flight model is set to 1.

In our analysis we will study how different mesh dimensions affects the pressure drop and separation performance. The meshpad dimensions applied in this study is illustrated in Figure 44.

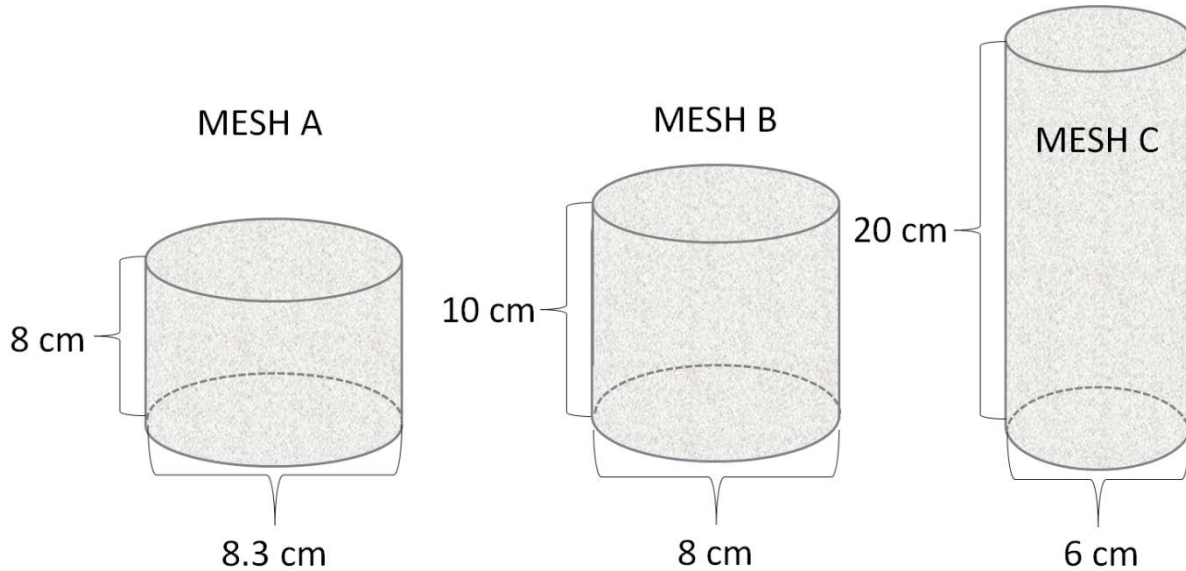


Figure 44 Three different sized meshes used in the analysis of pressure drop and separation performance of the NNGLseparator

The NNGLseparator is design to separate Natural-Gas and Oil at high pressure. However the current experimental rig uses water and air at ambient conditions to test its performance. Analysis on how the different fluids affect the pressure drop and separation performance is thus needed. As reference in our analysis we have proposed three different gas-liquid mixes. These are Air and Water, Natural Gas and Oil, and Sulfur hexafluoride (SF6) and Exxsol D80.

The fluid properties were obtained through the commercial software PRO/II using the build in Peng-Robinson thermodynamic package. These properties are for 101.325 kPa cited in Table 1, for 600kPa in Table 2 and for 8000kPa in Table 3.

SF6 and Exxsol D80 will only be used for simulation at standard atmospheric condition. This is because SF6 becomes fluid at 600kPa and Exxsol D80 is a commercial product from ExxonMobil and is not listed in PRO/II component library.

101,325 kPa (1 Atm)

Component		Water	Air	Natural Gas	Oil	SF6	Exxsol ⁸ D80
Phase		Water	Gas	Gas	Liquid	Gas	Liquid
Temperature	C	15	15	15	15	15	15
Pressure	kPa	101,325	101,325	101,325	101,325	101,325	101,325
Density	KG/M3	998,8	1,2	0,7	756,9	6,3	796
Viscosity	kg/m-sec	1,14E-03	1,80E-05	1,06E-05	6,66E-04	1,46E-05	1,70E-03
Surface Tension	N/m	7,30E-02	n/a	n/a	2,45E-02	n/a	2,63E-02

Table 1 Fluid properties at 101.325 kPa

600 kPa

Component		Water	Air	Natural Gas	Oil
Phase		Water	Gas	Gas	Liquid
Temperature	C	15	15	15	15
Pressure	kPa	600,000	600,000	600,000	600,000
Density	KG/M3	998,8	7,3	4,4	757,3
Viscosity	kg/m-sec	1,13E-03	1,80E-05	1,06E-05	6,65E-04
Surface Tension	N/m	7,30E-02	n/a	n/a	2,44E-02

Table 2 Fluid properties at 600 kPa

8000 kPa

Component		Water	Air	Natural Gas	Oil
Phase		Water	Gas	Gas	Liquid
Temperature	C	15	15	15	15
Pressure	kPa	8000	8000	8000	8000
Density	KG/M3	998,8	100,6	73,6	762,7
Viscosity	kg/m-sec	1,13E-03	1,80E-05	1,06E-05	6,54E-04
Surface Tension	N/m	7,30E-02	n/a	n/a	2,43E-02

⁸ The properties for Exxsol D80 are taken from <http://www.fasakimya.com/upload/d80-msds.pdf> and http://www.shxiangmao.com/Upload.asp?filenames=File_123713.pdf. The confidence of the sources is uncertain, as they are both foreign companies. However, the properties in the two documents match against each other.

Table 3 Fluid properties at 8000 kPa

Components used in our Natural Gas and Oil

NATURALGAS		OIL			
METHANE	82,8 wt%	PENTANE	6,0 wt%	CP	24,0wt%
ETHANE	17,2 wt%	BENZENE	15,0 wt%	DECANE	15,0wt%
		CH	25,0 wt%	OCTANE	15,0wt%

Table 4 Composition of the simplified Oil and Natural Gas

Because there are several variables that affect the separation performance we have proposed as reference scenario for our simulations. The reference scenario consists of:

- Mesh A dimensions
- 20 Hz spin frequency (f)
- Air and Water at 101.325 kPa and 15°C
- K-factor of 0.5 (see equation(4.2.1))

Separation performance

The two main mechanisms for separation of liquid droplets in the NNGLseparator are cyclonic separation by centrifugal forces and droplet capture by the meshpad. With the assumptions of fully developed forced vortex flow, it was shown in section 3.2.4 that cyclonic separation determines the separation performance for the NNGLseparator. All our analysis in this section is therefore based on our modified time of flight model (equation(3.2.26)).

Further assumption is a uniform droplet size distribution. This means that the separation performance is determined on how efficient a certain droplet size is separated. When analyzing parameters and properties against each other, the droplet size that is separated with 50% efficiency is used as reference.

4.2.1 Analysis

The separation performance is determined by the size of t_{axial} and t_{radial} , explained in section 2.5.1. Here reducing t_{radial} , or increasing t_{axial} , increases the separation efficiency. How changing certain parameters affect the separation performance can for the most part be explained through those two time variables.

It is normal to measure the separation performance against a gas load factor (K). The factor is also known as the K-factor or Souder-Brown Coefficient, and dictates the gas velocity (U_g) the separator operates under (GPSA, 2004)

$$U_g = K \sqrt{\frac{(\rho_l - \rho_g)}{\rho_g}} \quad (4.2.1)$$

This factor is often used by the oil and gas industry and is thus used as parameter in this analysis. A plot for how the separator performs under different K-factors can be seen in Figure 45. The specifications for this simulations are standard mesh dimensions (Mesh A) spinning at 20 Hz and air-water at standard atmospheric conditions (101,325 kPa and 15°C).

As expected the efficiency goes down when operating under higher K-factors. Higher K- factor means higher gas velocity (see equation(4.2.1)). This in turn increases the drag force exerted on the droplet, thus increasing its axial velocity. The efficiency will then decrease because t_{axial} decreases. This decrease in efficiency can be compensated by reducing t_{radial} . One of the method to reduce t_{radial} is to increase the centrifugal force through the mesh spin. Figure 46 shows how an increase in K- factor can be compensated with an increased mesh spin. Here the separation efficiency is represented by D_{p50} .

For the scenario plotted in Figure 46, increasing the K- factor from 0.3 to 0.7 can be compensated by increasing the spin frequency from 20 Hz to 25Hz. Thus a less increase in mesh spin is requires to compensate for the increase in K-factor. Further study of Figure 46 shows that the efficiency increase with spin frequency is in the order of two ($\propto f^2$). While from Figure 47 the efficiency can be seen to reduce with the square root of the K-factor.

Another possible method to increase the efficiency is through the mesh height, where an increase in height increases t_{axial} , this is shown in Figure 48. Here efficiency is plotted as a function of the height for three different spin settings. The simulation parameters are as Figure 46 with a K-factor of 0.5.

From the plot in Figure 48 the heights effect on D_{p50} can be seen to be in the order of minus one ($\propto h^{-1}$). Here a decrease in D_{p50} indicates and increase in efficiency. Hence the heights effect is linear, or in the order of one ($\propto h^1$). This effect is much lower than the frequency. When the plot for 10 Hz spin frequency is compared to 20 and 30 Hz, a height exceeding the dimensions of our mesh examples is required to obtain the same separation performance.

How our mesh examples perform in comparison to each other can be seen in Figure 49 and Figure 50. In Figure 50 D_{p50} is plotted as a function of the mesh spin. And in Figure 49 the efficiency is plotted as function of the droplet size at 10 and 20 Hz spin frequency. Both

simulations are done with an air and water mix at standard atmospheric conditions and a K factor of 0.5.

From Figure 49 and Figure 50, MESH C gives the highest efficiency. This is only due to its greater height. Because of the assumption of forced vortex flow inside the mesh ($u_{\theta} = r\omega$) the area of the different mesh types does not affect the efficiency. This can be seen in equation (3.2.17), where the radial velocity is linearly increasing with r . Hence the decrease in separation distance is the same as the decrease in velocity. The lesser diameter of MESH C will therefore not affect the separation efficiency, because t_{radial} remains unchanged.

Our time of flight model includes the mesh porosity, and its effect on the efficiency is shown in Figure 57. Here the reference scenario from the introduction (section 4.1) is simulated with typical relative density specifications for metal foams (ERG Aerospace, 2011). The connection between relative density and porosity comes from equation(3.4.2), where an increase in relative density equals a decrease in porosity.

From the plots in Figure 57 the efficiency is shown to increase with decreasing relative density. This is because the porosity affects the axial velocity by decreasing the volume, thus t_{axial} is reduced. However the effect is shown to be miniscule. This is because the typical range in relative density for metal foams is very small, ranging normally from 4% to 12% (ERG Aerospace, 2011). Converting these values give porosity between 0.96 and 0.88. The maximum effect can then be calculated to be 8.3%. However, the porosity effect on the swirl flow is not included in our time of flight model. If the porosity is very small the flow might easier slip from the spinning mesh, thus reducing its tangential velocity.

In Figure 51 and Figure 52 different fluid components are compared to each other. Here the separation performance is plotted as function of droplet diameter for the components Air-Water, Natural Gas-Oil and SF6-Exxol D80 in Figure 51 and as function of the superficial gas velocity in Figure 52. SF6 is Sulfur hexafluoride and Exxsol D80 is a commercial product from ExxonMobil Chemical. The components used to simulate Natural Gas and Oil can be seen in Table 4.

It is important to remember that the separation performance, through the time of flight model, represents how efficient a certain sized droplet is separated. Hence it is not efficiency in terms of amount of liquid separated. This is discussed further at the end of this section

The plot in Figure 51 and Figure 52 shows that the separation performance is higher for the Natural Gas and Oil mix. This is due to the lower gas viscosity compared to Air and Natural Gas (see Table 1). Here increasing the gas viscosity increases the drag, resulting in a decrease in efficiency for air-water and SF6-ExxsolD80 mix. This decrease in efficiency for air and water is compensated with the higher density difference between liquid and gas. Hence air and water has

a slightly higher efficiency than SF6 and Exxsol D80. The effect of the gas density increase becomes more obvious when analyzing different pressures.

A simulation of separation performance at different pressure can be seen in Figure 53 and Figure 54, where we have compared Natural Gas and Oil to Water and Air at 6 and 80 Bar (600 and 8000 kPa). The superficial gas velocity is set constant to 5 m/s in Figure 53, and the droplet diameter is set constant to 0.01 μm in Figure 54

The plot in Figure 53 and Figure 54 shows a higher separation performance at lower pressure. However the time of flight model does not have the pressure included as variable. It is therefore the pressures effect on the fluid parameters that affects the separation performance. The pressure increases the density of the gas, thus decreasing the density difference between liquid and gas. This decreases the droplet separation efficiency, because the buoyant force increases.

A comparison between the fluids with the K-factor set to 0.5 can be seen in Figure 55. Here the efficiency increases with higher pressure. This is because of the definition of the K-factor. From equation (4.2.1) it can be seen that the gas velocity decreases when the gas density increases. The effect from equation (4.2.1) is thus higher than the effect on equation(3.2.26). This trend is also shown in Figure 56, where separation efficiency of a given droplet diameter is plotted against the K-factor.

Analysis of the plot in Figure 53 and Figure 54 leads to some confusion, when it is compared to real life experience. Experience has shown that, the efficiency goes drastically down when changing from an air and water mix to Natural Gas and Oil. This is however not represented in Figure 53 and Figure 54. Here it is important to differ between separation efficiency of a certain droplet size, and separation efficiency in terms of total liquid removed. In Table 1, 2 and 3 the surface tension is included. The surface tension will affect the droplet size disruption, and Water has a higher surface tension than both oil and ExxsolD80. Meaning, the droplets you can expect in a spray of water are larger than for ExxsolD80 or Oil. Hence, you can expect a higher separation performance for Air and Water than for Oil and Natural Gas. An indication of different size distribution can be obtained through an expression for maximum stable droplet size. Here Sleicher (1962) derived an empirical expression as follows (Swanborn, 1988):

$$We(\mu_g \frac{U_g}{\sigma})^{1/2} = 38 \left[1 + 0.7 \left(\mu_l \frac{U_g}{\sigma} \right)^{0.7} \right] \quad (4.2.2)$$

Where

σ = surface tension (N/m)

and the parameter We is defined as

$$We = d_{max} \rho_g \frac{U_g^2}{\sigma} \quad (4.2.3)$$

From Equation (4.2.2) the maximum stable droplet size can be seen to increase with the surface tension. However, the expression gives only a maximum droplet size and no indication of the amount of smaller droplets entrained in the flow. Thus, assuming a uniform droplet size distribution with a diameter calculated from equation (4.2.2) will possibly give a too high (and false) efficiency.

A summary of how mesh dimensions, spin, porosity and K- factor affects the separation performance is shown in Table 5.

	Proportionality
Mesh Dimensions (m)	$\propto h$ $\propto d^0$
Mesh Spin (Hz)	$\propto f^2$
Mesh Porosity (-)	$\propto \varepsilon$
Gas Load Factor (m/s)	$\propto K^{-0.5}$

Table 5 Summary of the mesh dimensions, spin and K-factor proportionality to efficiency

How the fluid components from Table 1, 2 and 3 affect the separation performance is summarized in Table 6. Here air and water at atmospheric pressure is used as reference values to compare the different fluid. The reference values are shown in the bottom right corner of Table 6.

Pressure Component	101.325 kPA	600 kPA	8000 kPA
Air & Water	$\propto 1 \cdot Ref_1 h$	$\propto 1.56 \cdot Ref_1 h$	$\propto 2.78 \cdot Ref_1 h$
	$\propto 1 \cdot Ref_2 f^2$	$\propto 1.72 \cdot Ref_2 f^2$	$\propto 3.13 \cdot Ref_2 f^2$
	$\propto 1 \cdot Ref_3 K^{-0.5}$	$\propto 1.26 \cdot Ref_3 K^{-0.5}$	$\propto 1.65 \cdot Ref_3 K^{-0.5}$
Natural Gas & Oil	$\propto 0.94 \cdot Ref_1 h$	$\propto 1.47 \cdot Ref_1 h$	$\propto 2.75 \cdot Ref_1 h$
	$\propto 1.05 \cdot Ref_2 f^2$	$\propto 1.72 \cdot Ref_2 f^2$	$\propto 3.13 \cdot Ref_2 f^2$
	$\propto 0.97 \cdot Ref_3 K^{-0.5}$	$\propto 1.20 \cdot 10^2 \cdot Ref_3 K^{-0.5}$	$\propto 1.65 \cdot Ref_3 K^{-0.5}$
SF6 & Exxsol D80	$\propto 1.42 \cdot Ref_1 h$	Reference values	
	$\propto 1.56 \cdot Ref_2 f^2$	$Ref_1 = 3.6 \cdot 10^8$	
	$\propto 1.18 \cdot Ref_3 K^{-0.5}$	$Ref_2 = 6.4 \cdot 10^4$	
		$Ref_3 = 4.5 \cdot 10^3$	

Table 6 Proportionality to separation performance for different fluid components

4.2.2 Plots

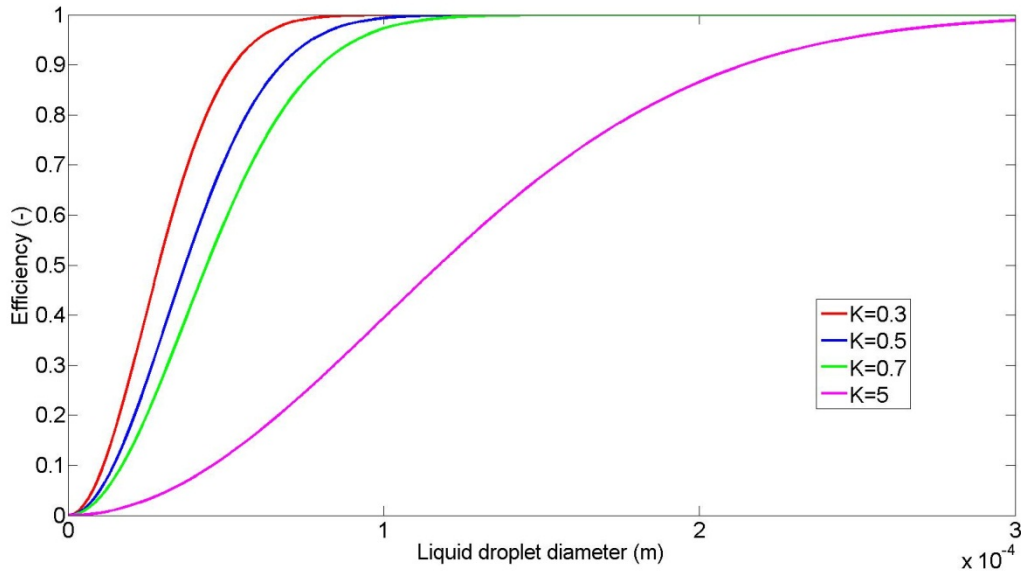


Figure 45 Comparison of droplet separation efficiency for different K-factors. Modeled with air and water mix at 15°C and standard atmospheric pressure.

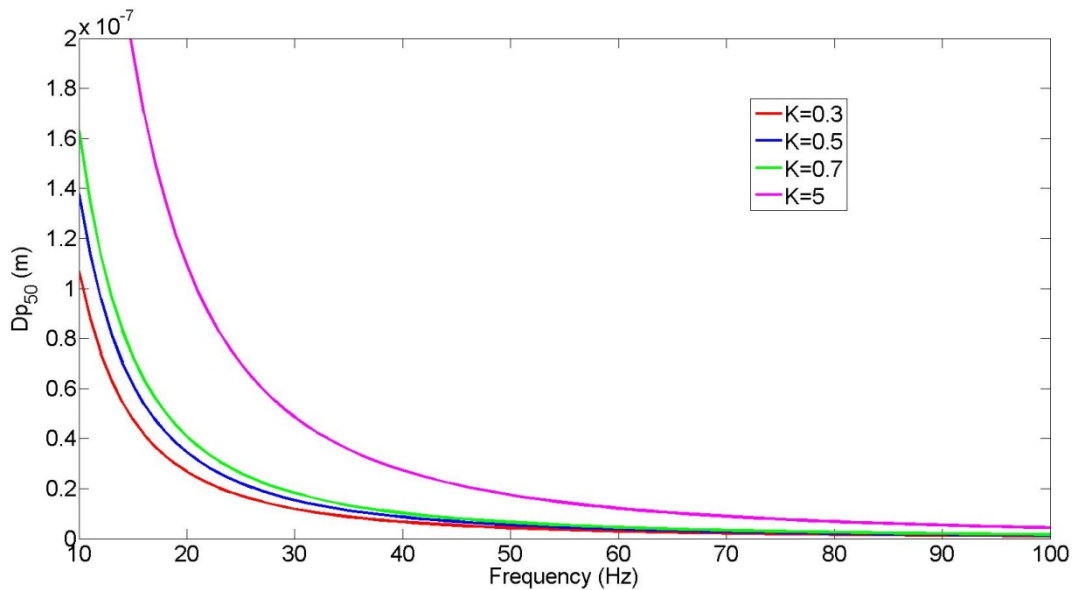


Figure 46 Droplet size separated with 50% efficiency as a function of the spin frequency for different K-factors. Modeled with Air and Water mix at 15°C and standard atmospheric pressure.

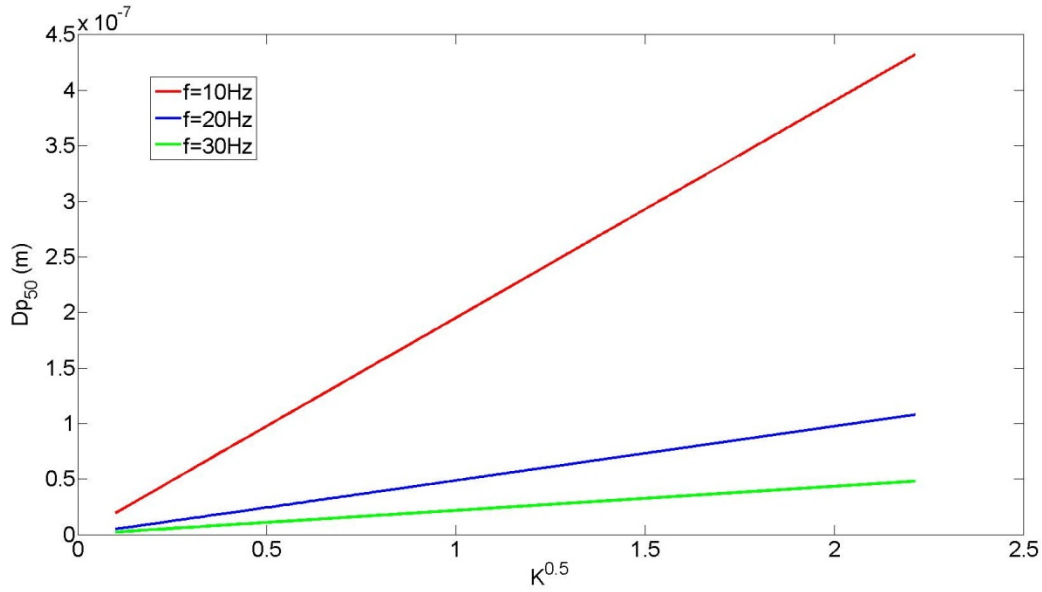


Figure 47 Droplet size separated with 50% efficiency as a function of the K-factor for different spin frequencies. Modeled with air and water mix at 15°C and standard atmospheric pressure

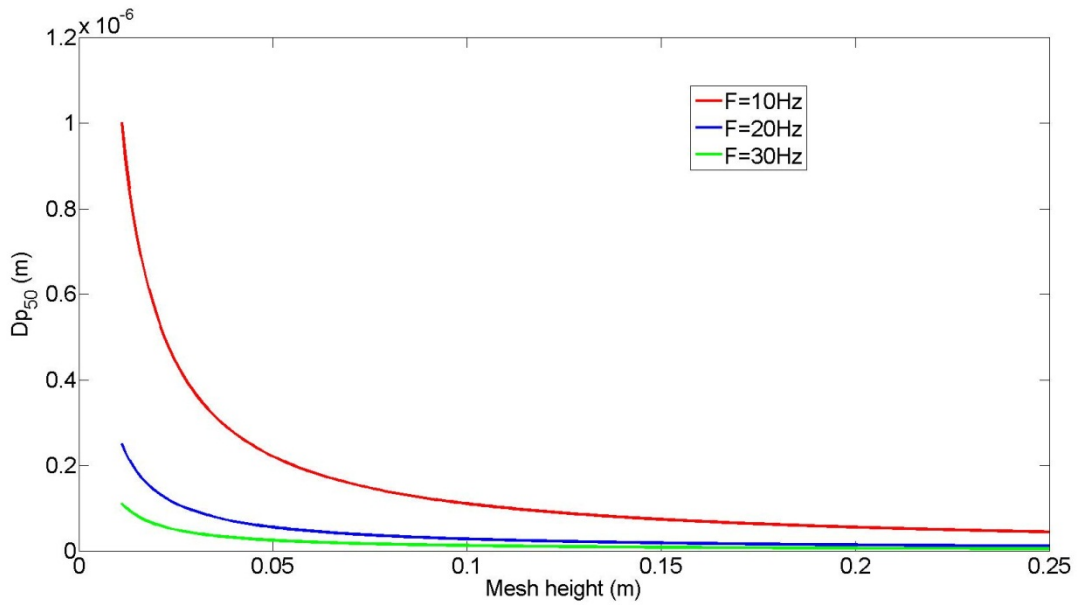


Figure 48 Droplet size separated with 50% efficiency as a function of the mesh height for different frequencies. Modeled with a 0.5 K-factor, Air and Water mix at 15°C and standard atmospheric pressure

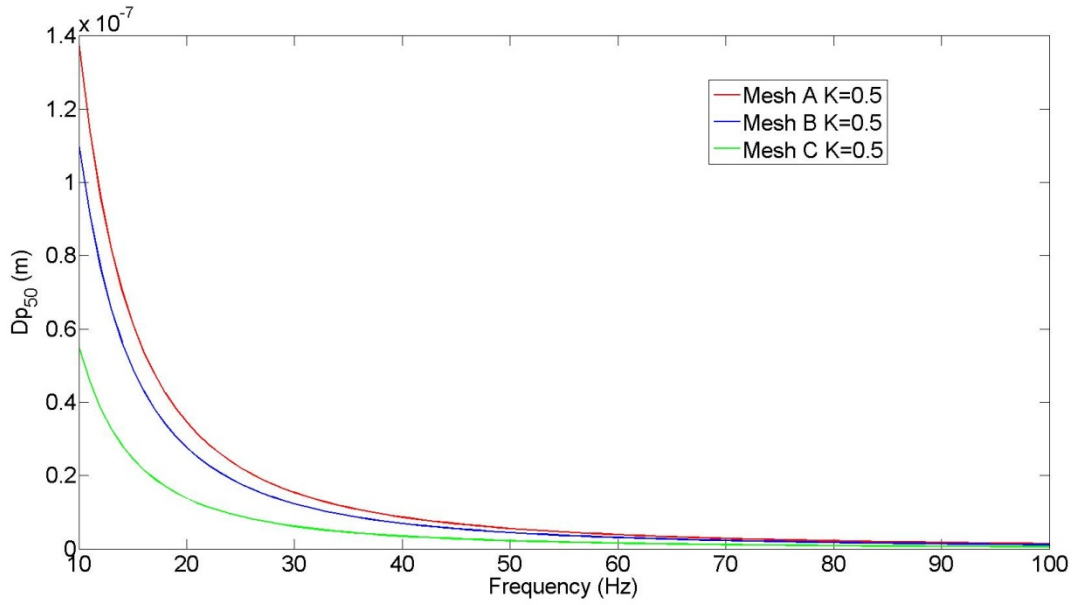


Figure 49 Droplet size separated with 50% efficiency as a function of the spin frequency for different mesh dimensions. Modeled with a 0.5 K-factor, Air and Water mix at 15°C and standard atmospheric pressure

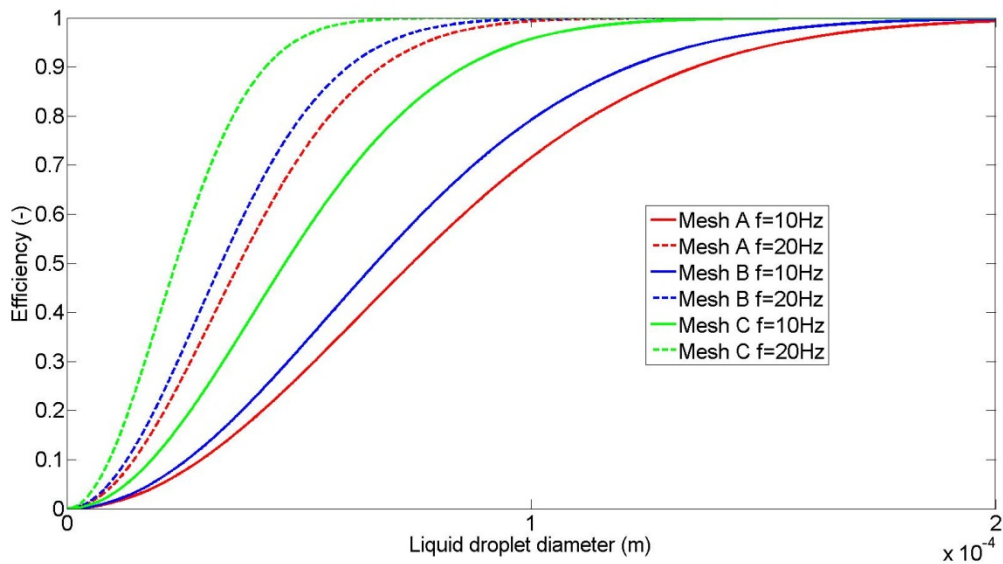


Figure 50 Comparison of droplet separation efficiency for different mesh dimensions and spins. Modeled with a 0.5 K-factor, at 15°C and standard atmospheric pressure.

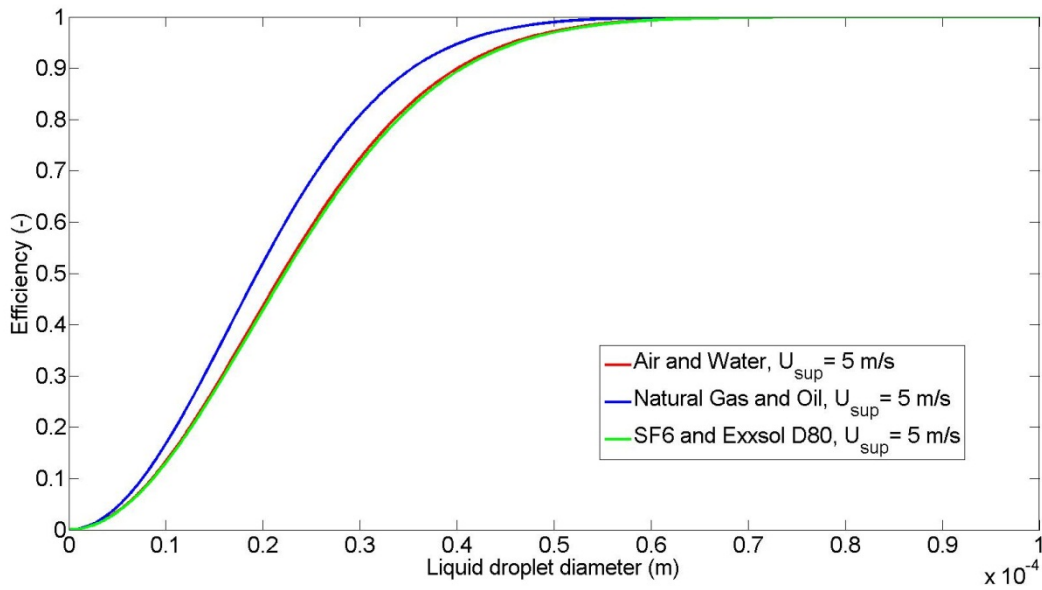


Figure 51 Comparison of droplet separation efficiency for the components: Air and Water, Natural gas and Oil, SF6 and Exxsol D80. Modeled with a 0.5 superficial gas velocity, 20HZ spin frequency 15°C and standard atmospheric pressure.

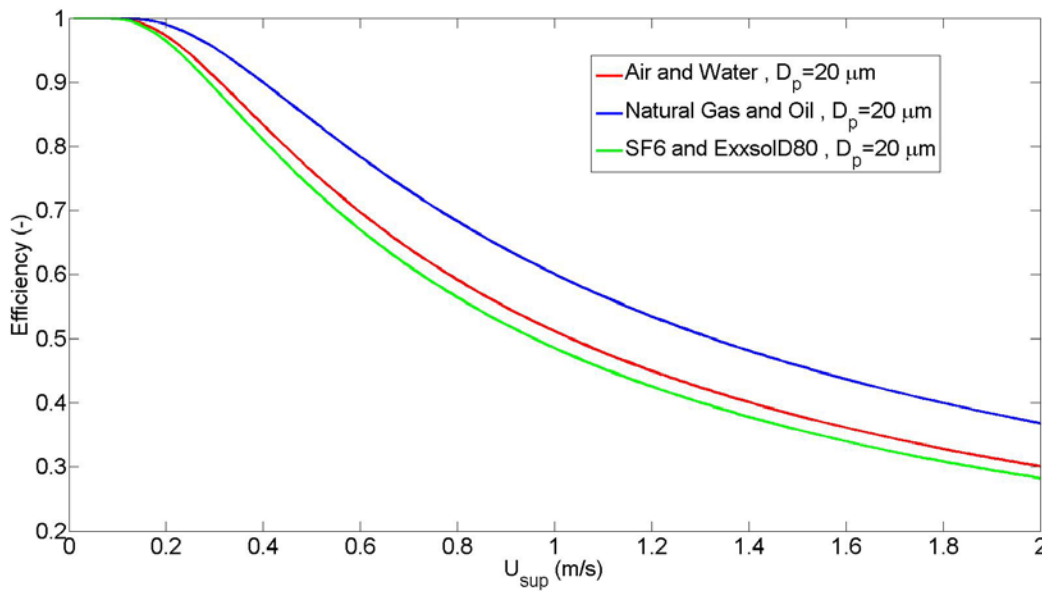


Figure 52 Comparison of $20 \mu\text{m}$ droplet separation efficiency for the components: Air and Water, Natural gas and Oil, SF6 and Exxsol D80, plotted against the superficial gas velocity. Modeled with 20 Hz spin frequency, 15°C and standard atmospheric pressure.

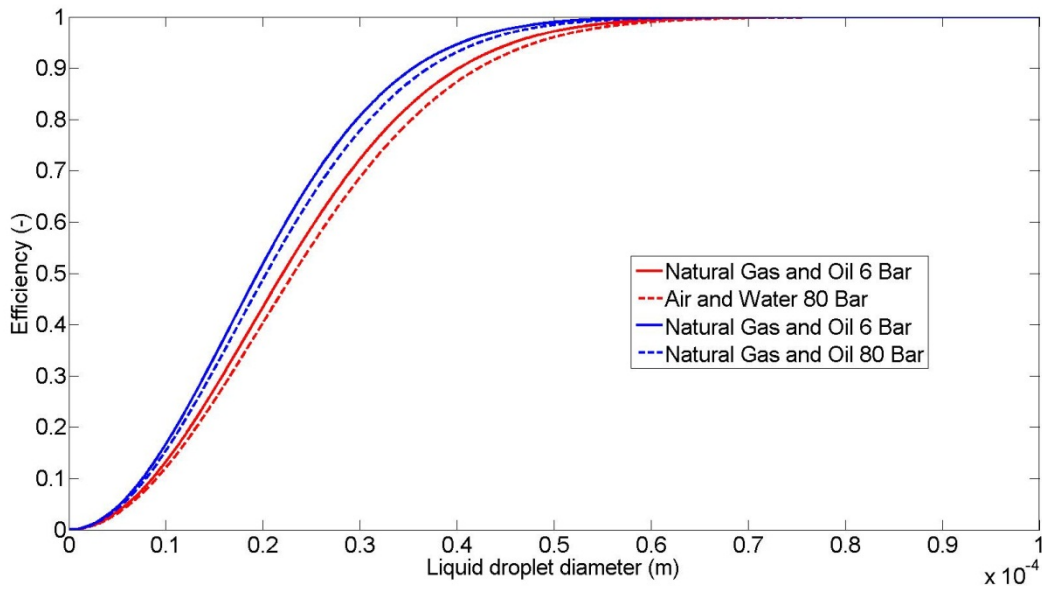


Figure 53 Comparison of droplet separation efficiency for the components: Air and Water and Natural gas and Oil at high pressure. Modeled with 20Hz spin frequency, 5 m/s U_{sup} and 15°C.

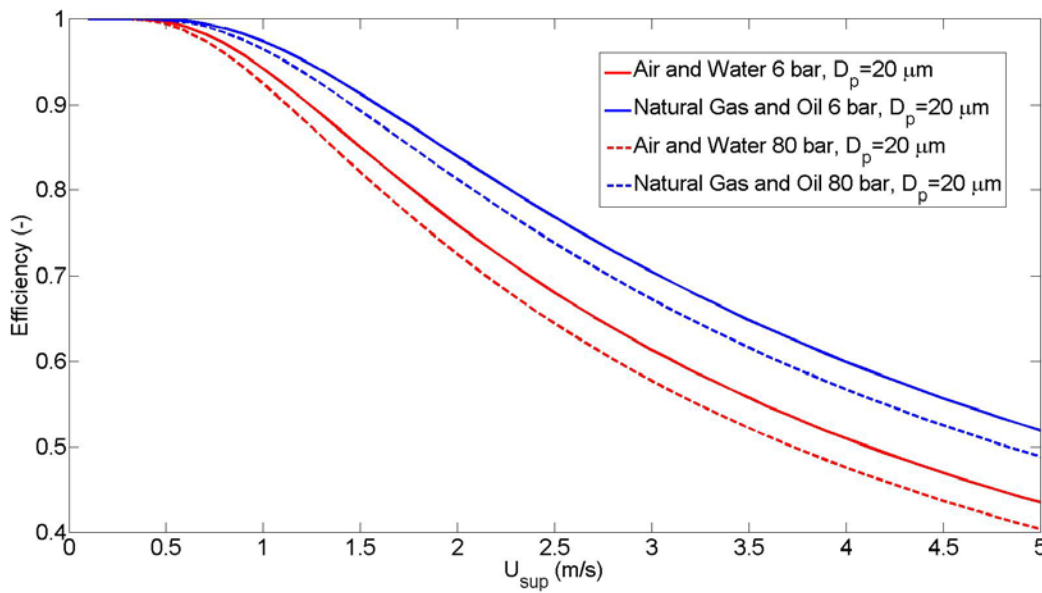


Figure 54 Comparison of 20 μm droplet separation efficiency for the components: Air-Water at 6 and 80 bar and Natural gas –Oil at 6 and 80 bar, plotted against the superficial gas velocity. Modeled with 20 Hz spin frequency and 15°C.

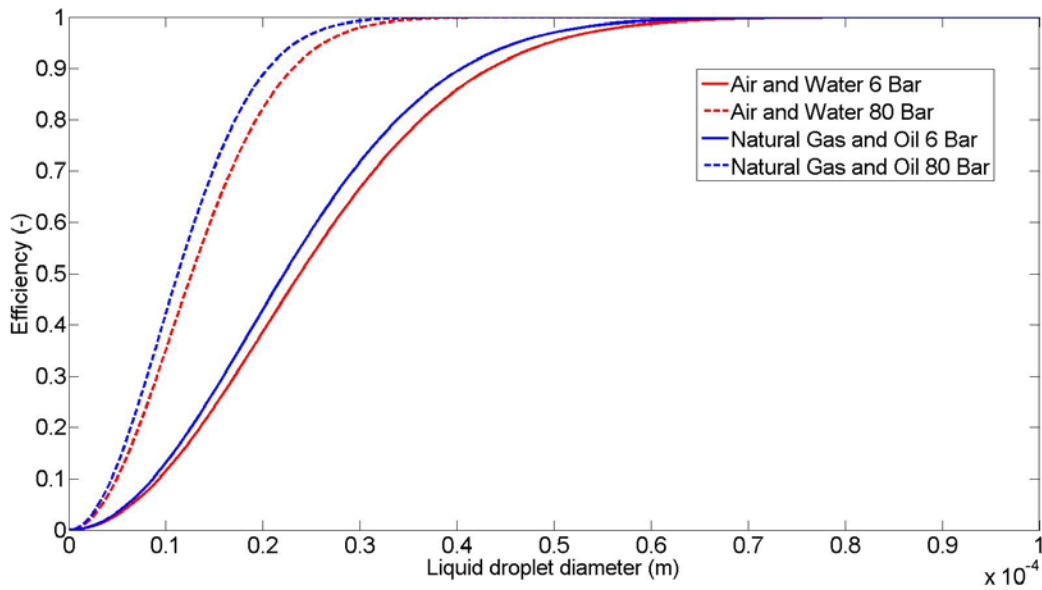


Figure 55 Comparison of droplet separation efficiency for the components: Air and Water and Natural gas and Oil at high pressure. Modeled with 20 Hz spin frequency a 0.5 K-factor and 15°C.

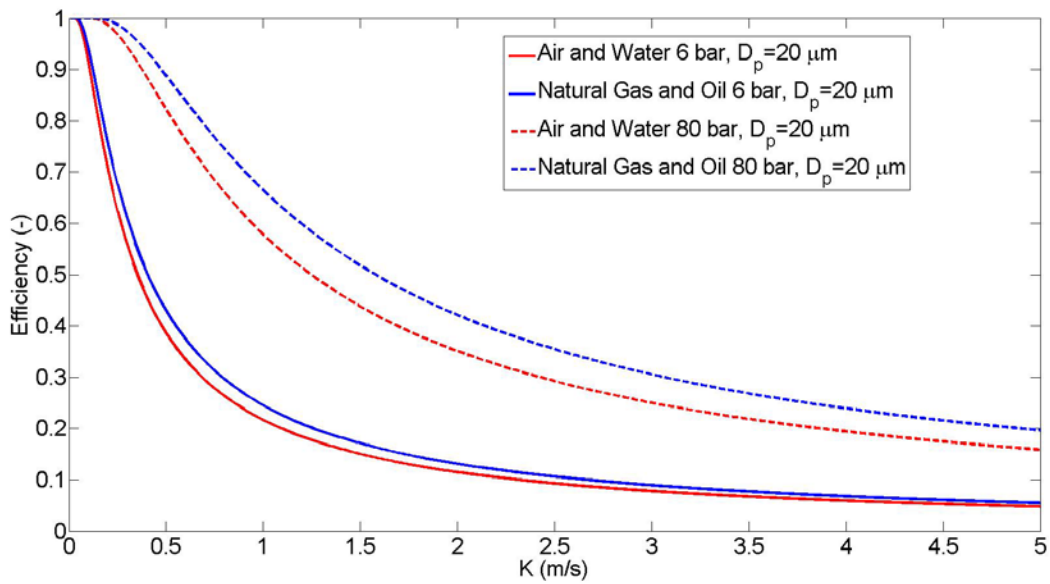


Figure 56 Comparison of 20 μm droplet separation efficiency for the components: Air-Water at 6 and 80 bar and Natural gas –Oil at 6 and 80 bar, plotted against the K-factor. Modeled with 20 Hz spin frequency and 15°C

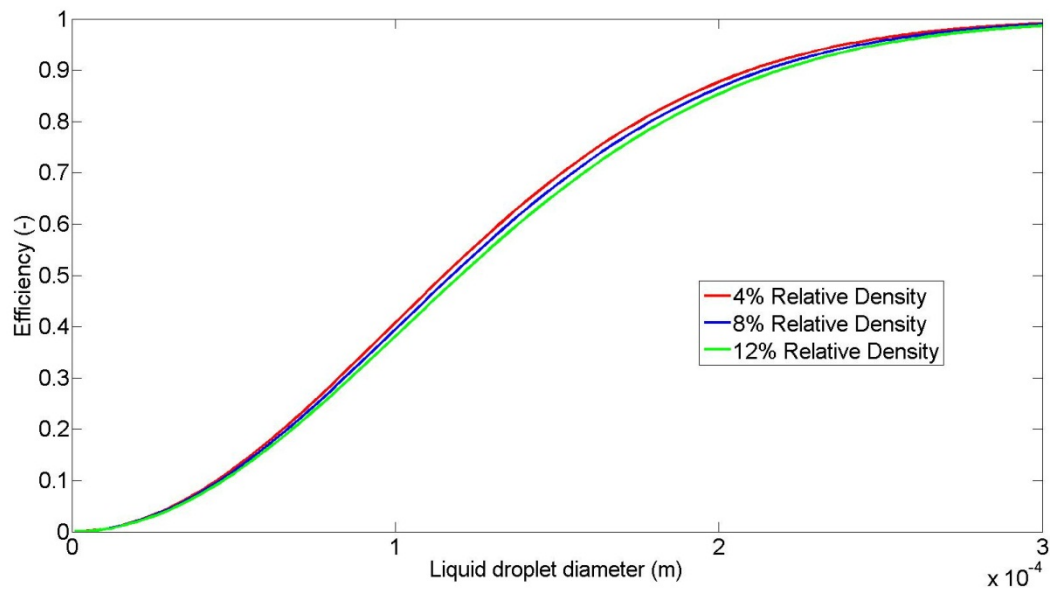


Figure 57 Comparison of droplet separation efficiency for different mesh porosities. Modeled with 20Hz spin frequency, a 0.5 K-factor, air and water mix at 15°C and standard atmospheric pressure

4.3 Pressure drop

Because we do not have a proper model capable of describing the amount of liquid accumulating in the mesh we will only focus on dry flow in our analysis of pressure drop across the NNGLseparator. And through our review of the two modeling approaches given by the Blake and the Hazen-Dupuit-Darcy expression, it was the latter that showed to better replicate the experimental results. And the assumption of forced vortex flow inside the mesh leads to the original Hazen-Dupuit-Darcy equation.

4.3.1 Results and discussion

The Hazen-Dupuit-Darcy equation consists of a viscous and a form drag term. Here the pressure drop through the viscous term is linearly depended on the superficial gas velocity and quadratic depended through the form drag term. Hence it is the ratio between these terms that determines pressure drops proportionality to the superficial gas velocity.

When it comes to mesh dimensions it is the height, and not the diameter that determines the pressure drop. This is because of the assumption of forced vortex flow. In section 3.3.4 it was shown that the pressure is then only dependent on the vertical flow through the meshpad.

A comparison between our mesh dimensions (see Figure 44) can be seen in Figure 58. Here the pressure drop for air at standard atmospheric conditions is plotted as a function of the superficial gas velocity. The same values have been plotted as ratio between each other in Figure 61. Study of this plot shows the linear relation between pressure drop and the mesh height, where the ratio between the different mesh heights can be seen as rate of change in the plots.

Because the coefficients in the Hazen-Dupuit-Darcy equation are empirical values representing a specific porous structure, we have only values for the specific meshpad used in the experiment. We can therefore not simulate different mesh properties such as porosity and surface area. It is then the fluid properties that become the dominating factor, when reviewing the pressure drop proportionality to superficial gas velocities.

In Figure 59 we have plotted pressure drop as a function of the superficial gas velocity for our three reference fluids Air, Natural Gas and SF₆ at standard atmospheric values (1013.25 kPa and 15°C). Here the viscosity to density ratio between Natural Gas and Air is almost the same ($\mu_g/\rho_g \sim 1.5 \cdot 10^5$). This results in a pressure drop equally proportional to the superficial gas velocity. But the specific values for the density and viscosity are about 70% higher for Air (see Table Fluid properties), which can be further exploited through simulation with different mesh dimension. Here pressure drop across a 10 cm high meshpad with Air is the same as a 17cm meshpad with our Natural Gas, simulated in Figure 62.

The SF6 has a low viscosity to density ratio. This is reflected in Figure 59 by the much more quadratic shape of the curve compared to air and natural gas. At low gas velocities the pressure drop for SF6 is higher than Natural gas, but lower than Air. This is because at lower velocities it is the linear viscous term that becomes dominant. And the SF6 has higher viscosity than air, but lower than Natural Gas (see Table 1)

The pressure drop for Air and Natural Gas at 6 and 80 Bar is plotted against the superficial velocity in Figure 60. A comparison between the two pressures shows how sensitive the pressure drop is to higher pressure. The increase in pressure drop is however only due the effect pressure have on the gas density, which increases with the pressure. This results in a lower viscous to density ratio, increasing the form drags dominance on the pressure drop. This in turns make the pressure drop more sensitive to increased gas velocities.

Because the Hazen-Dupuit-Darcy equation consist of a linear viscous drag term and a quadratic form drag term, the pressure drops dependents on the fluid parameter is relative. Hence, the following proportionality table is proposed:

	Pressure drop, ΔP
At high pressure	$\propto U_{sup}^2$
Very viscous flow	$\propto U_{sup}$
Mesh dimensions	$\propto h, \propto d^0$

Table 7 Proportionality in the pressure drop model

Proportionality between the different fluid components can be seen in Table 8.

Pressure Component	101.325 kPA	600 kPA	8000 kPA
Air & Water	$\propto 1 \cdot Ref_{1p} h$	$\propto 1 \cdot Ref_{1p} h$	$\propto 1 \cdot Ref_{1p} h$
	$\propto 1 \cdot Ref_{2p} U_{sup}^2$	$\propto 5.9 \cdot Ref_{2p} U_{sup}^2$	$\propto 79.9 \cdot Ref_{2p} U_{sup}^2$
	$\propto 1 \cdot Ref_{3p} U_{sup}$	$\propto 1.0 \cdot Ref_{3p} U_{sup}$	$\propto 1.0 \cdot Ref_{3p} U_{sup}$
Natural Gas & Oil	$\propto 1 \cdot Ref_{1p} h$	$\propto 1 \cdot Ref_{1p} h$	$\propto 1 \cdot Ref_{1p} h$
	$\propto 0.6 \cdot Ref_{2p} U_{sup}^2$	$\propto 3.6 \cdot Ref_{2p} U_{sup}^2$	$\propto 57.6 \cdot Ref_{2p} U_{sup}^2$
	$\propto 0.6 \cdot Ref_{3p} U_{sup}$	$\propto 0.6 \cdot Ref_{3p} U_{sup}$	$\propto 0.6 \cdot Ref_{3p} U_{sup}$
SF6 & Exxsol D80	$\propto 1 \cdot Ref_{1p} h$	Reference values	
	$\propto 5.1 \cdot Ref_{2p} U_{sup}^2$	Ref_{1p} = 1	
	$\propto 0.8 \cdot Ref_{3p} U_{sup}$	Ref_{2p} = 160.8	
		Ref_{3p} = 190	

Table 8 Proportionality to pressure drop for different fluid components

4.3.2 Plots

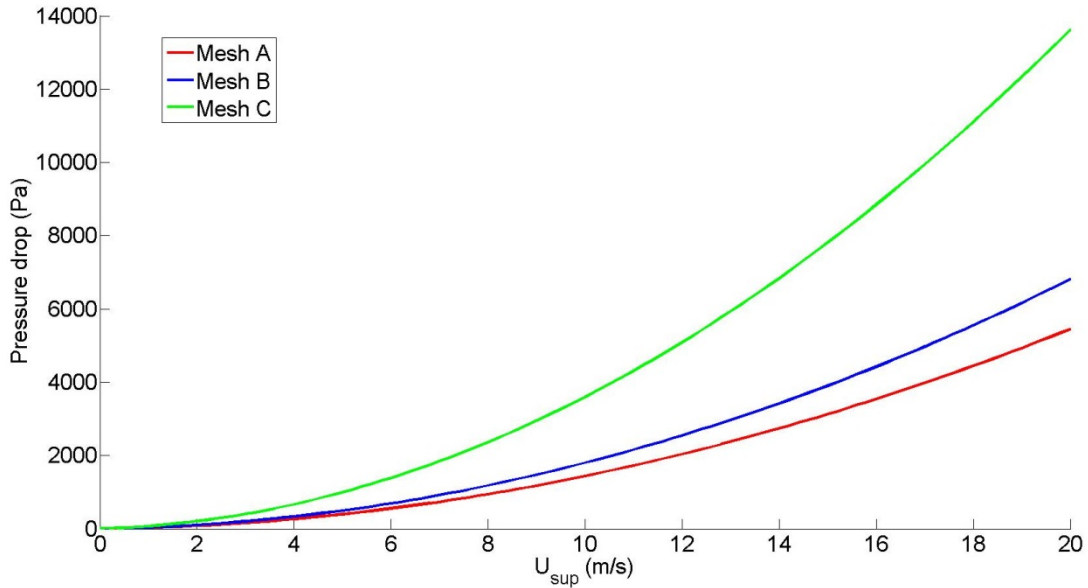


Figure 58 Comparison of pressure drop for different mesh dimensions as function of superficial gas velocity. Modeled with air at 15°C and standard atmospheric pressure.

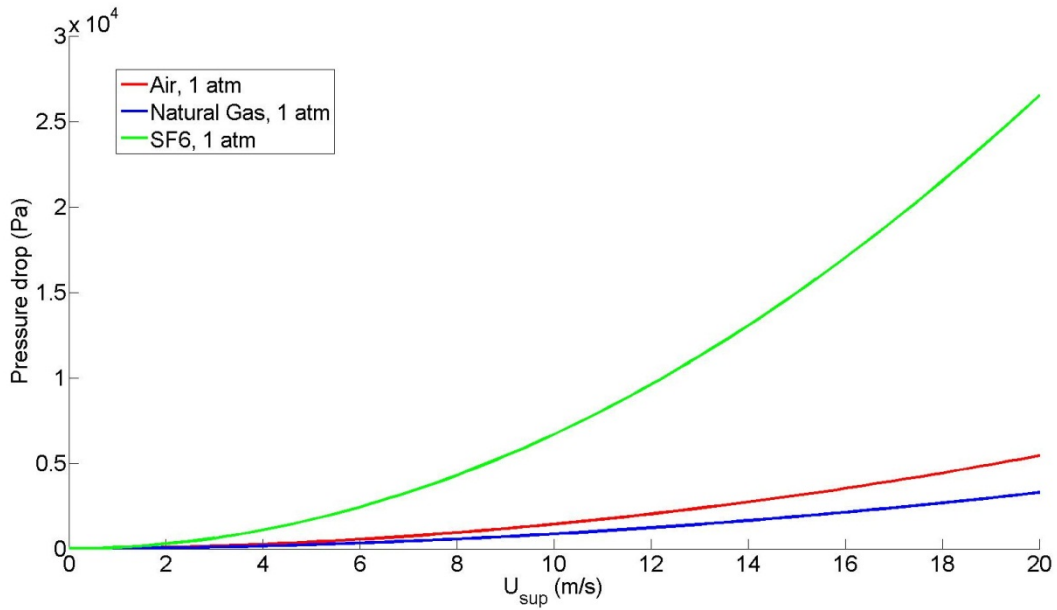


Figure 59 Comparison of pressure drop for different gas composition as function of superficial gas velocity. Modeled with Mesh A, 15°C and standard atmospheric pressure.

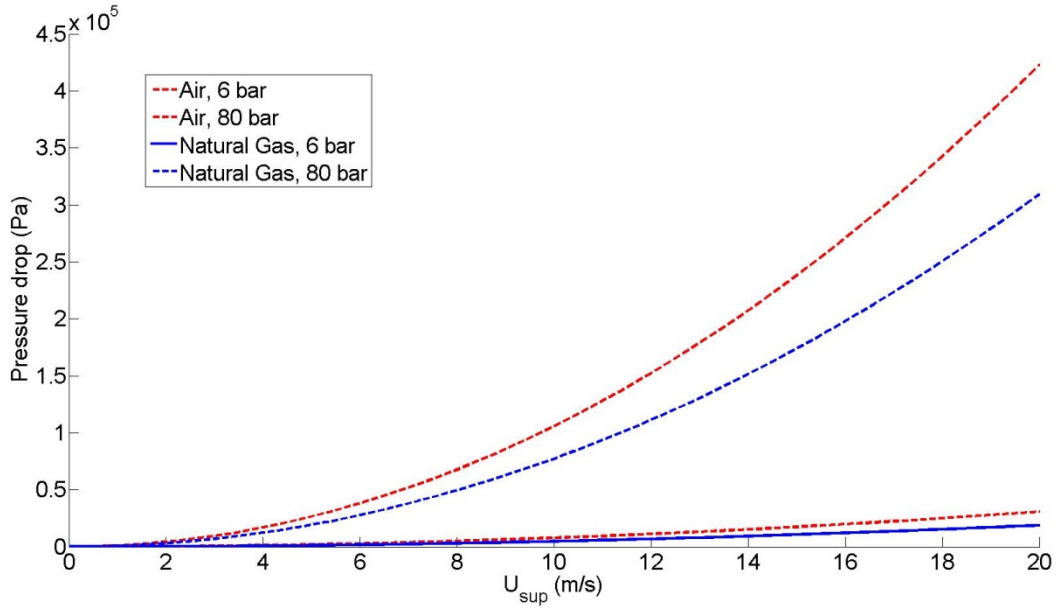


Figure 60 Comparison of pressure drop for different gas composition and pressure as function of superficial gas velocity. Modeled with Mesh A and 15°C.

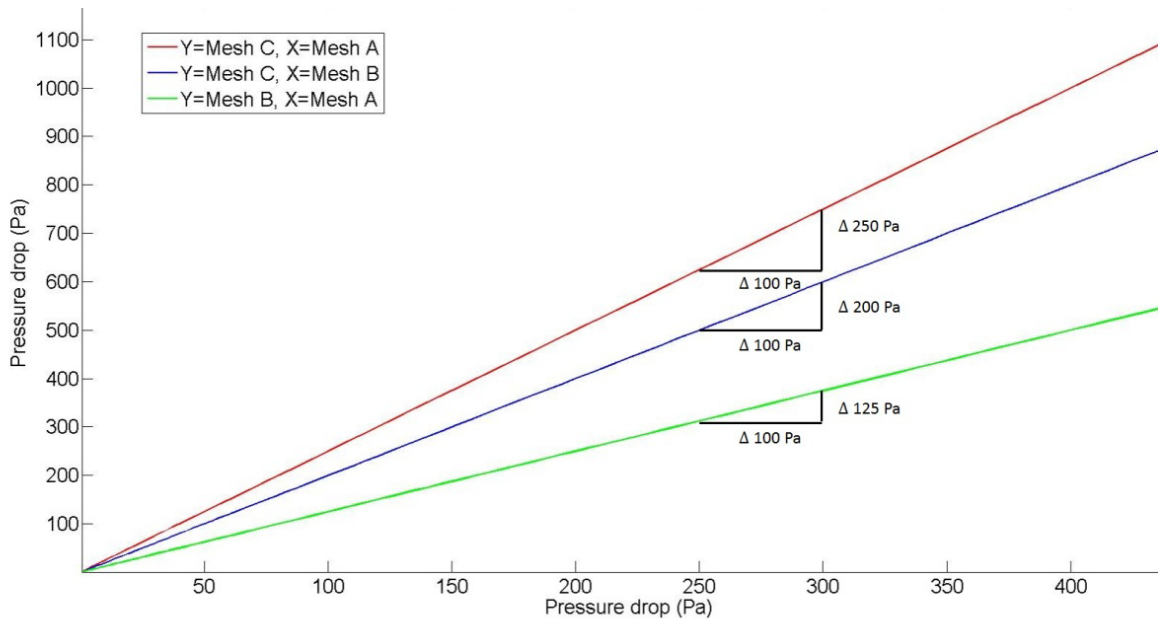


Figure 61 Comparison of pressure drop for different mesh dimensions as function of superficial gas velocity. Modeled with air at 15°C and standard atmospheric

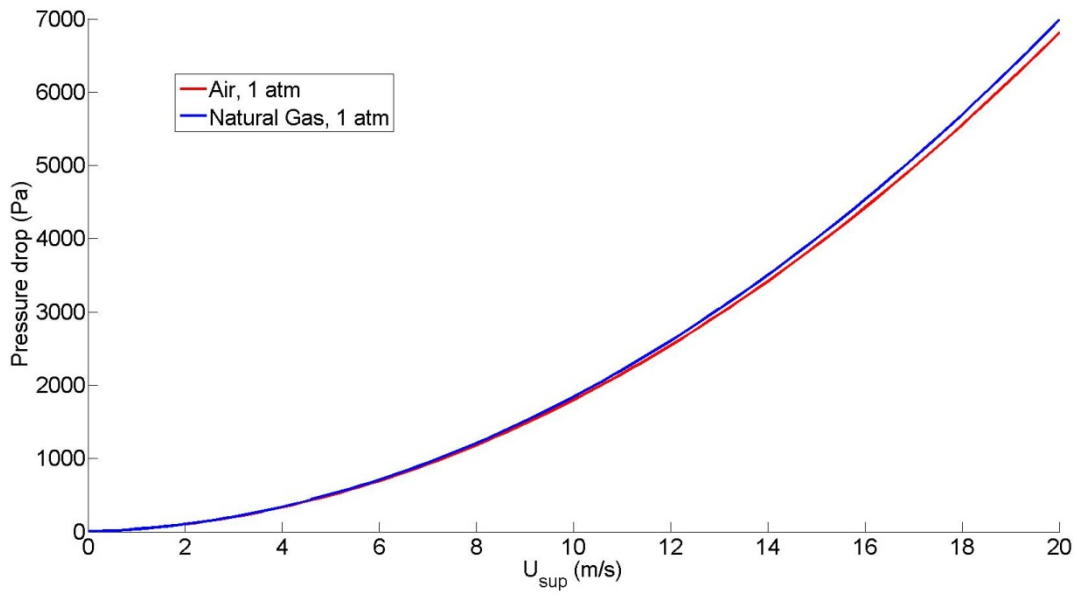


Figure 62 Comparison between pressure drop with air and 10 cm mesh height to Natural Gas with 17 cm mesh height. Modeled with air at 15°C and standard atmospheric

4.4 Summary of the proposed models

To develop a one-dimensional model describing pressure drop and separation performance of the NNGLseparator we analyzed exiting models describing pressure drop across fixed porous media, droplet capture in fixed meshpad and centrifugal separation. Based on the analysis we proposed a further extension to some of these models. This section is summary of the models reviewed, and the extensions that were proposed.

4.4.1 Separation Performance

Modeling of the separation performance was divided into droplet capture and cyclonic separation. The two models are done in sequence, where the droplets that are not capture are separated by centrifugal separation.

Droplet capture is first modeled through single target capture, where the impact of the centrifugal force on previous proposed model was analyzed. This analysis led to an expression for the effect of centrifugal forces on the single target capture.

$$\eta_{I-c} = \frac{S_2 - S_1 + F_c S_1 - F_c S_2 + F_c S_2 \exp(S_1 t') - F_c S_1 \exp(S_2 t')}{S_2 \exp(S_1 t') - S_1 \exp(S_2 t')} \quad (4.4.1)$$

This expression was then compared to the original expression for non-spinning mesh. And through this comparison, it was shown that the effect of the centrifugal force is negligible for $\bar{a}_c < 10^{-3}$. Here \bar{a}_c is a nondimensionalized expression for the centrifugal acceleration.

$$\bar{a}_c = \frac{a_c d_f}{2u_0^2} \quad (4.4.2)$$

Because of the limited effect of the centrifugal force, it was concluded that the empirical expression by Landhal and Herrmand (1949) can be used for calculation of single target capturing efficiency. This was then used to calculate the overall capturing efficiency, where a new modified expression was derived

$$\eta_{CT} = 1 - \exp\left(-\frac{2 \eta_{ST} S_{mesh} h \left(1 + \frac{1}{u_z} \left[\omega \frac{R_w}{2} - \frac{1}{R_w} \int_0^{R_w} u_\theta(r) dr\right]\right)}{\pi}\right) \quad (4.4.3)$$

The derivation of this expression is an extension of the original model for the overall droplet capture. Equation (4.4.3) takes into account a difference in tangential velocity between the

spinning mesh and the gas flow. In the case of the flow following the forced vortex characteristics, the droplet capture is the same as for fixed mesh demisters.

Based on the time of flight model for cyclonic separation, an expression for droplet separation by centrifugal forces in the NNGLseparator was proposed:

$$\eta_c = \frac{1}{1 - \left\{ \exp \left[\frac{D_p \beta (\rho_l - \rho_g) \omega^2 h \varepsilon}{18 \mu_g U_{sup}} \right] \right\}} \quad (4.4.4)$$

Here the mesh porosity (ε) is included in the model, as well as an β - factor. The β - factor relates to the mesh structure and to have a value between 0.7 and 1.0. The factor was shown to have a small impact on the separation performance. Hence, it was argued that this factor might be difficult to measure in experiments.

Comparison of equation (4.4.4) and (4.4.3) showed that for spin frequency above 4 Hz cyclonic separation is the mechanism that determines the separation performance of the NNGLseparator.

4.4.2 Pressure Drop

Through literature review, two expressions for pressure drop in porous media were studied. In the case of the meshpad used in the NNGLseparator, the Hazen-Dupuit-Darcy equation was deemed the best model for pressure drop. The decision was based on a comparison between the Blake expression and the Hazen-Dupuit-Darcy Equation, to experimental data (see Figure 63 below).

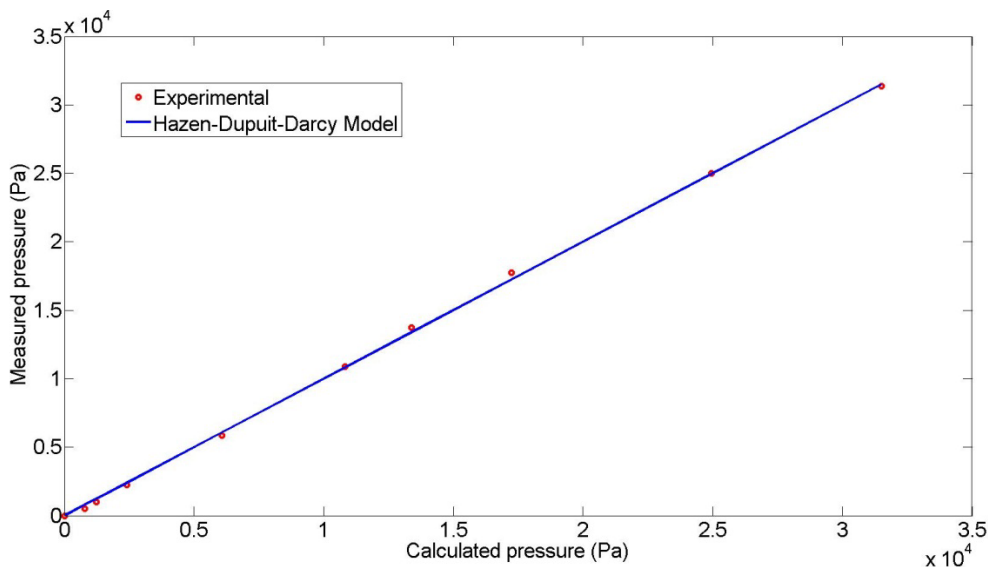


Figure 63 Comparison between the Hazen-Dupuit-Darcy equation and experimental data

Comparisons to the same experiment determined the permeability and the form drag factor as follows:

$$K_p = 9.4 \cdot 10^{-8} \text{ m}^2 \quad \text{and} \quad C_p = 131.3 \text{ m}^{-1}$$

Based on an analysis of two flow scenarios across the spinning mesh, a modification to the Hazen-Dupuit-Darcy equation was proposed in the case of the flow having a different tangential velocity compared to the rotating mesh pad.

$$\Delta P = \left(\frac{\mu}{K_p} U_{sup} + C_p \rho U_{sup}^2 \right) \cdot \left(h + \frac{\frac{R_w}{2} \omega - \frac{1}{R_w} \int_0^{R_w} u_\theta dr}{u_z} \right) \quad (4.4.5)$$

This equation was then analyzed by simulating a simplified combined vortex flow. Here it was shown that even with small deviation from the forced flow characteristics the pressure drop gets a significant and measurable increase (see Figure 64 below).

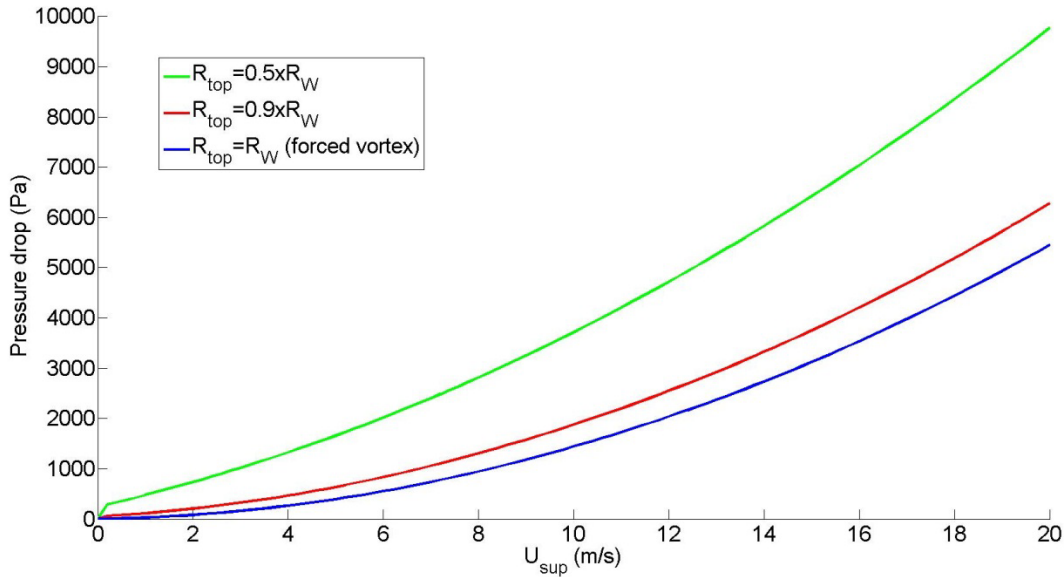


Figure 64 Comparison of different swirl flow characteristics on the pressure drop.

The result in Figure 64 was then compared to previous experimental observations. Here the experiments showed that the pressure drop is not affected by the mesh spin. Hence, it was concluded that the forced vortex flow is the most likely flow characteristics occurring inside the meshpad.

For pressure drop across a wet meshpad, a model proposed by Helsør (2006) was suggested. The model is based on a relation between liquid holdup and an effective porosity. However there is no

proper model capable of describing the amount of liquid accumulating in the mesh. Instead an analysis comparing conventional meshpad demisters to the spinning meshpad was given. Here it was shown that the increased drainage area together with the centrifugal forces make the NNGLseparator less prone to flooding compared to conventional fixed meshpad demisters.

5 Conclusion

In this thesis, a first model of the NNGL separator for gas-liquid flows has been developed. The proposed model was then used to perform a parametric study of the separator performance, focusing on pressure drop and separation efficiency.

The proposed model is one-dimensional, based on the geometry design of the first prototype of the separator. Annular flow was assumed as the flow pattern entering the separator, with a forced vortex flow in the rotating part of the separator. The possibility of the gas flowing around the separator was neglected. Flow and droplet size distribution entering the separator was assumed uniform.

For the pressure drop across the separator, two existing models for pressure drop across a porous media were considered, namely the Blake expression and the Hazen-Dupuit-Darcy equation. By comparing with available experimental data, it was determined that the Hazen-Dupuit-Darcy equation was the more appropriate model to describe pressure drop in the NNGL separator. The model was further extended in order to include the effect of a spinning mesh pad. However, the effect of the spinning mesh pad was seen to be negligible.

For the separation efficiency, existing models for droplet capture efficiency in a standard mesh pad demister and separation efficiency in a centrifuge were combined and modified in order to be able to describe the effect of a spinning mesh. The centrifugal force was included in the droplet capture model, where it was observed to be negligible for $\bar{a}_c < 10^{-3}$, where \bar{a}_c is a number for a nondimensionalized centrifugal acceleration. The mesh porosity and an empirical β -factor was included in the cyclonic separation model in order to take into account the obstructing mesh effect on the droplet track. A comparison between the droplet capture and cyclonic model showed that separation efficiency is determined by cyclonic separation above 4 Hz.

The proposed model was used to perform a parametric study of the separator performance. Three different fluids at three different pressure and three different mesh geometries were considered. Different flow conditions were also considered, with flow (or K factor) ranging up to 5 m/s for the efficiency study and 20 m/s for pressure drop. Rotation frequencies were simulated up to 100 Hz, droplet diameter up to 100 μm , mesh relative density from 4% to 8% and mesh height from 1 to 25 cm.

The separation efficiency was observed to increase quadratic with the spinning frequency and linearly with the mesh height, while it reduces with the square root of the K factor. It was further shown to be independent of the mesh diameter, and the porosity was shown to have very small effect. In terms of fluid properties, the efficiency was shown to reduce for flows with high gas viscosity and flows with small difference between liquid and gas density.

The pressure drop increases linearly with the mesh height, and is independent of the mesh diameter. The pressure drop dependence on the flow was observed to be linear for very viscous fluids and quadratic at high pressure.

In all, the proposed model was able to describe the performance of the NNGL separator in terms of pressure drop and separation efficiency. This model needs to be validated with further experimental data for the different flow conditions involved. In addition, assumptions in the model should also be reviewed, in particular the effect of the spinning mesh on the separation efficiency.

5.1 Suggestions for further Work

The pressure drop model proposed in this paper consists of two coefficients, which needs to be determined through experiments. To further validate these coefficients; more experiments involving different fluid components should therefore be performed.

Further studies on the flow characteristics inside the mesh should be performed. Here the hypothesis of an increased pressure drop when the flow slips from the mesh should be studied further.

Experiments have shown that the pressure drop is affected by the liquid hold up (Helsør, 2006). At present time, there exists no model for the liquid hold up. Therefore, more study of liquid hold-up should be performed. Here we suggest a correlation between liquid load, mesh spin and drainage area and liquid holdup to be studied further.

Appendix A

Example of a MATLAB code used to calculate pressure drop and efficiency of a given droplet size

Runner

```
%-----  
%Fluid Properties  
%-----  
%1ATM  
%-----  
viscG=0.00001797408913;%kg/(m-sec),Air  
%viscG=0.00001063102081;%kg/(m-sec), Natural Gas  
%viscG=0.00001458889437;%kg/(m-sec),SF6  
rhoL=998.8027344;%kg/m3 ,Water  
%rhoL=756.9100342;%kg/m3 ,Oil  
%rhoL=796;%kg/m3 ,Exxol D80  
rhoG=1.224846482;%kg/m3 , Air  
%rhoG=0.7396171093;%kg/m3 , Natural Gas  
%rhoG=6.256990433;%kg/m3 , SF6  
%-----  
%6 Bar  
%-----  
%viscG=0.00001797408913;%kg/(m-sec),Air  
%viscG=0.00001063102081;%kg/(m-sec), Natural Gas  
%rhoL=998.7849731;%kg/m3 ,Water  
%rhoL=757.2796631;%kg/m3 ,Oil  
%rhoG=7.283519745;%kg/m3 , Air  
%rhoG=4.448032379;%kg/m3 , Natural Gas  
%-----  
%80 Bar  
%-----  
%viscG=0.00001797408913;%kg/(m-sec),Air  
%viscG=0.00001063102081;%kg/(m-sec), Natural Gas  
%rhoL=998.7980347;%kg/m3 ,Water  
%rhoL=762.6702881;%kg/m3 ,Oil  
%rhoG=100.6383209;%kg/m3 , Air  
%rhoG=73.5552597;%kg/m3 , Natural Gas  
%-----  
%Mesh properties  
%-----  
RELrho=10; %relative density in percent  
height=0.08; % Meshpad height in meters  
radius=0.0415; % radius of meshpad in meters  
K=0.5; % K-factor in m/s  
Cp=131.3089; %From factor, Found by curvefitting  
Kp=9.4017*(10^-8); %Permeability,Found by curvefitting  
f=20; %mesh spin in Hz  
Dp=1*10^(-6); %droplet diameter for calculation of efficiency in meters  
[eff,deltaP,X]=Body(viscG,rhoL,rhoG,K,Dp,RELrho,Cp,Kp,radius,height,f);
```

Body

```
function
[eff,deltaP,X]=Body(viscG,rhoL,rhoG,K,Dp,RELRho,Cp,Kp,radius,height,f)
por=(100-RELRho)/100;% porosity
Smesh=(10.4+1.1*(100-por*100))*(64.52/1.639);% Mesh surface area
Dw=(4*(1-por))/Smesh;%Mesh fiber diameter
Usup=K*sqrt((rhoL-rhoG)/rhoG);
Qg=Usup*(3600*pi*(radius^2));
omega=2*pi*f;
beta=1;%slowdown factor. To ignore this factor set beta=1
alfa=0;%setting this to equal zero assumes forced vortex flow
%-----
%Dry pressuredrop
%-----
HagenDup=Cp*rhoG*((Usup)^2)+(viscG/Kp)*Usup;
ReM=(rhoG*Usup)/(viscG*Smesh);%turbulent when Re>2 from fundamentals of
particle technology
MeshfricTur=(5/ReM+0.4/(ReM^0.1));%The carman correlation the last term is a
turbulence correction
MeshfricLam=5/ReM;
if ReM>4
    Blake=(MeshfricTur*rhoG*(Usup^2)*Smesh)/(por^3);
else
    Blake=(MeshfricLam*rhoG*(Usup^2)*Smesh)/(por^3);
end
deltaP=HagenDup*height*(1+alfa*(radius*omega));
%-----
%Efficiency
%-----
ac=radius*(omega^2)*(Dw/(2*(Usup^2)));%non dimensionlized centrifugal acc
psil=(1*(rhoL)*(Dp^2)*Usup)/(18*viscG*Dw);%must be larger then 0.125 /Ranz and
Wong)
if ac<(10^(-3))
    psi2=(1*(rhoL-rhoG)*(Dp^2)*Usup)/(18*viscG*Dw);
    Fc=2*psi2*ac;
    etaEmp=(psil^3)/((psil^3)+0.77*(psil^2)+0.22);
    Q=sqrt((1/(2*psil))+((1/(4*psil))^2));
    Tmark=(1/Q)*atan((4*psil*Q)/(4*psil-1));
    S1=-((1/(4*psil))+sqrt(((1/(4*psil))^2)+(1/(2*psil))));
    S2=-((1/(4*psil))-sqrt(((1/(4*psil))^2)+(1/(2*psil))));
    etaCent=(Fc*S2*exp(Tmark*S1)-Fc*S1*exp(Tmark*S1)+Fc*S1-Fc*S2+S2-
S1)/(S2*exp(S1*Tmark)-S1*exp(S2*Tmark));
else
    etaEmp=(psil^3)/((psil^3)+0.77*(psil^2)+0.22);
end
effCapt=1-exp((-
2/3)*((etaEmp*Smesh*height*(1+alfa*((radius*omega)/(2*Usup))))/pi));
effTOF=1-((1/(exp(((Dp^2)*beta*(rhoL-
rhoG)*(omega^2)*height*por)/(18*viscG*Usup))))^2);
eff=max(effTOF,effCapt);
X=ac;
end
```

Appendix B

Momentum equation (Navier-Stoke) (White, 2007)

$$\rho \left(\frac{\partial U}{\partial t} + U \cdot \nabla U \right) = -\nabla P + \mu \nabla^2 U + f$$

X-momentum equation (White, 2007)

$$\rho \left(\frac{\partial u_x}{\partial t} + u_x \frac{\partial u_x}{\partial x} + u_y \frac{\partial u_x}{\partial y} + u_z \frac{\partial u_x}{\partial z} \right) = -\frac{\partial p}{\partial x} + \mu \left[\frac{\partial^2 u_x}{\partial x^2} + \frac{\partial^2 u_x}{\partial y^2} + \frac{\partial^2 u_x}{\partial z^2} \right] + \rho g_x$$

Momentum cylindrical coordinates (White, 2007)

$$r: \quad \rho \left(\frac{\partial u_r}{\partial t} + u_r \frac{\partial u_r}{\partial r} + \frac{u_\theta}{r} \frac{\partial u_r}{\partial \theta} + u_z \frac{\partial u_r}{\partial z} - \frac{u_\theta^2}{r} \right) = -\frac{\partial p}{\partial r} + \mu \left[\frac{1}{r} \frac{\partial}{\partial r} \left(r \frac{\partial u_r}{\partial r} \right) + \frac{1}{r^2} \frac{\partial^2 u_r}{\partial \theta^2} + \frac{\partial^2 u_r}{\partial z^2} - \frac{u_r}{r^2} - \frac{2}{r^2} \frac{\partial u_\theta}{\partial \theta} \right] + \rho g_r$$

$$\theta: \quad \rho \left(\frac{\partial u_\theta}{\partial t} + u_r \frac{\partial u_\theta}{\partial r} + \frac{u_\theta}{r} \frac{\partial u_\theta}{\partial \theta} + u_z \frac{\partial u_\theta}{\partial z} - \frac{u_\theta u_r}{r} \right) = -\frac{1}{r} \frac{\partial p}{\partial \theta} + \mu \left[\frac{1}{r} \frac{\partial}{\partial r} \left(r \frac{\partial u_\theta}{\partial r} \right) + \frac{1}{r^2} \frac{\partial^2 u_\theta}{\partial \theta^2} + \frac{\partial^2 u_\theta}{\partial z^2} - \frac{u_\theta}{r^2} + \frac{2}{r^2} \frac{\partial u_r}{\partial \theta} \right] + \rho g_\theta$$

$$z: \quad \rho \left(\frac{\partial u_z}{\partial t} + \langle u_r \rangle \frac{\partial u_z}{\partial r} + \frac{\langle u_\theta \rangle}{r} \frac{\partial u_z}{\partial \theta} + \langle u_z \rangle \frac{\partial u_z}{\partial z} \right) = -\frac{\partial p}{\partial z} + \mu \left[\frac{1}{r} \frac{\partial}{\partial r} \left(r \frac{\partial u_z}{\partial r} \right) + \frac{1}{r^2} \frac{\partial^2 u_z}{\partial \theta^2} + \frac{\partial^2 u_z}{\partial z^2} + \frac{1}{r^2} \frac{\partial u_z}{\partial \theta} \right] + \rho g_z$$

Continuum equations

$$\nabla \cdot v = 0$$

$$\rho_f \left(\frac{\partial v}{\partial t} + (v \cdot \nabla) v \right) = -\nabla p + \mu \nabla^2 v + \rho_f g \beta (T - T_c) \mathbf{j}$$

Porous continuum equations (Lage & Merrikh, 2005)

$$\nabla \cdot \langle v \rangle = 0$$

$$\begin{aligned} \rho_f \left(\frac{\partial \langle v \rangle}{\partial t} + (\langle v \rangle \cdot \nabla) \langle v \rangle \right) \\ = -\nabla \langle p \rangle + \mu_{eff} \nabla^2 \langle v \rangle + \rho_f g \beta (\langle T \rangle - T_c) \mathbf{j} - \frac{\mu}{k} \boldsymbol{\varepsilon} \langle v \rangle - \rho_f C \boldsymbol{\varepsilon}^2 |\langle v \rangle| \langle v \rangle \end{aligned}$$

$\langle v \rangle$ =pore velocity. β =isentropic coefficient

Coefficient estimates (Lage & Merrikh, 2005): $\mu_{eff} = \mu$, $k = \frac{d^2\phi^3}{b(1-\phi)^2}$ $C = 0.55/K^{1/2}$

Porous continuum equations in cylindrical coordinates:

The porous continuum equations are taken from the article by Lage and Merrikh (2005). Any complete derivation of these equations was not given, only a statement that the equations are a result of modeling through volume averaging. The conversion of the general porous continuum equation to cylindrical coordinates is therefore purely build on the similarities between the continuum equation and the porous continuum equation.

$$r: \quad \rho \left(\frac{\partial \langle u_r \rangle}{\partial t} + \langle u_r \rangle \frac{\partial \langle u_r \rangle}{\partial r} + \frac{\langle u_\theta \rangle}{r} \frac{\partial \langle u_r \rangle}{\partial \theta} + \langle u_z \rangle \frac{\partial \langle u_r \rangle}{\partial z} - \frac{\langle u_\theta \rangle^2}{r} \right) = -\frac{\partial \langle p \rangle}{\partial r} + \mu \left[\frac{1}{r} \frac{\partial}{\partial r} \left(r \frac{\partial \langle u_r \rangle}{\partial r} \right) + \frac{1}{r^2} \frac{\partial^2 \langle u_r \rangle}{\partial \theta^2} + \frac{\partial^2 \langle u_r \rangle}{\partial z^2} - \frac{\langle u_r \rangle}{r^2} - \frac{2}{r^2} \frac{\partial \langle u_\theta \rangle}{\partial \theta} \right] + \rho g_r \beta (\langle T \rangle - T_c) - \frac{\mu}{k} \boldsymbol{\varepsilon} \langle u_r \rangle - \rho C \varepsilon^2 |\langle u_r \rangle| \langle u_r \rangle$$

$$\theta: \quad \rho \left(\frac{\partial \langle u_\theta \rangle}{\partial t} + \langle u_r \rangle \frac{\partial \langle u_\theta \rangle}{\partial r} + \frac{\langle u_\theta \rangle}{r} \frac{\partial \langle u_\theta \rangle}{\partial \theta} + \langle u_z \rangle \frac{\partial \langle u_\theta \rangle}{\partial z} - \frac{\langle u_\theta \rangle \langle u_r \rangle}{r} \right) = -\frac{1}{r} \frac{\partial \langle p \rangle}{\partial r} + \mu \left[\frac{1}{r} \frac{\partial}{\partial r} \left(r \frac{\partial \langle u_\theta \rangle}{\partial r} \right) + \frac{1}{r^2} \frac{\partial^2 \langle u_\theta \rangle}{\partial \theta^2} + \frac{\partial^2 \langle u_\theta \rangle}{\partial z^2} - \frac{\langle u_\theta \rangle}{r^2} + \frac{2}{r^2} \frac{\partial \langle u_r \rangle}{\partial \theta} \right] + \rho g_\theta \beta (\langle T \rangle - T_c) - \frac{\mu}{k} \boldsymbol{\varepsilon} \langle u_\theta \rangle - \rho C \varepsilon^2 |\langle u_\theta \rangle| \langle u_\theta \rangle$$

$$z: \quad \rho \left(\frac{\partial \langle u_z \rangle}{\partial t} + \langle u_r \rangle \frac{\partial \langle u_z \rangle}{\partial r} + \frac{\langle u_\theta \rangle}{r} \frac{\partial \langle u_z \rangle}{\partial \theta} + \langle u_z \rangle \frac{\partial \langle u_z \rangle}{\partial z} \right) = -\frac{\partial \langle p \rangle}{\partial z} + \mu \left[\frac{1}{r} \frac{\partial}{\partial r} \left(r \frac{\partial \langle u_z \rangle}{\partial r} \right) + \frac{1}{r^2} \frac{\partial^2 \langle u_z \rangle}{\partial \theta^2} + \frac{\partial^2 \langle u_z \rangle}{\partial z^2} + \frac{1}{r^2} \frac{\partial \langle u_z \rangle}{\partial \theta} \right] + \rho g_z \beta (\langle T \rangle - T_c) - \frac{\mu}{k} \boldsymbol{\varepsilon} \langle u_z \rangle - \rho C \varepsilon^2 |\langle u_z \rangle| \langle u_z \rangle$$

Where these estimates are used:

$$\langle u_r \rangle = \frac{u_r}{\varepsilon}, \quad \langle u_\theta \rangle = \frac{u_\theta}{\varepsilon}, \quad \langle u_z \rangle = \frac{u_z}{\varepsilon} \quad \text{and} \quad \beta (\langle T \rangle - T_c) = 1$$

Appendix C

Starting with the equation of motion for a droplet including the centrifugal force:

$$\frac{d(m\vec{u})}{dt} = \vec{F}_E + \vec{F}_D \quad (\text{C.1.1})$$

In the derivation given by Chen(1955) he assume the flow to follow Stokes' law, and neglected all external forces. In this derivation however, we will include the centrifugal force.

$$\frac{\rho_p D_p^2}{18\mu_g} \frac{d(\vec{u})}{dt} = \frac{\rho_p D_p^2}{18\mu_g} \vec{a}_c - (\vec{u} - \vec{v}) \quad (\text{C.1.2})$$

Equation (C.1.2) can be written in rectangular coordinates as follows

$$\frac{\rho_p D_p^2}{18\mu_g} \frac{d^2(x)}{dt^2} + \frac{dx}{dt} + v_x = 0 \quad (\text{C.1.3})$$

$$\frac{\rho_p D_p^2}{18\mu_g} \frac{d^2(y)}{dt^2} + \frac{dy}{dt} + v_x - \frac{\rho_p D_p^2}{18\mu_g} \vec{a}_c = 0 \quad (\text{C.1.4})$$

In Figure 65 the particle trajectory described by equation (C.1.3) and (C.1.4) is illustrated to get a sense of how to calculate the capture efficiency. Here a droplet that has enough inertia to hit the target when entering just in sight of the target can be reviewed as 100% captured (marked as blue in Figure 65). Droplets that do not have enough inertia to be captured, even when entering straight in front of the target, (marked as red in Figure 65) have a capturing efficiency of 0%.

Therefore, by nondimensionalizing equation (C.1.3) and (C.1.4) by the half the target diameter ($d_f/2$) and the inlet velocity (U_{sup}) one can calculate how efficient a certain droplet size is captured by the cylinder.

Thus, applying the following notation for the dimensionless variables:

$$\bar{x} = \frac{2x}{d_f} \quad \bar{y} = \frac{2y}{d_f} \quad \bar{u}_x = \frac{u_x}{V_0} \quad \bar{u}_y = \frac{u_y}{U_0} \quad \bar{t} = \frac{2U_0 t}{d_f} \quad \bar{a}_c = \frac{a_c d_f}{2u_0^2}$$

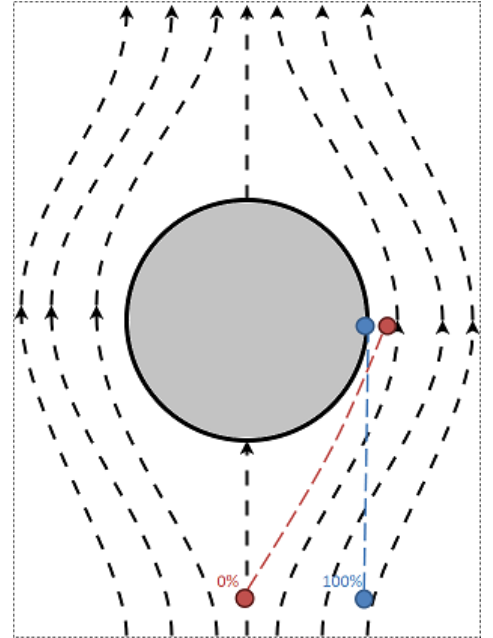


Figure 65 Illustration of the particle trajectory for droplet capture 0% and 100% efficiency

Gives:

$$\frac{dx}{dt} = \frac{dx}{d\bar{x}} \cdot \frac{d\bar{t}}{dt} \cdot \frac{d\bar{x}}{d\bar{t}} = \frac{d_f 2u_0}{2} \frac{d\bar{x}}{d\bar{t}} = u_0 \frac{d\bar{x}}{d\bar{t}} \quad \frac{dy}{dt} = \frac{dy}{d\bar{y}} \cdot \frac{d\bar{t}}{dt} \cdot \frac{d\bar{y}}{d\bar{t}} = \frac{d_f 2u_0}{2} \frac{d\bar{y}}{d\bar{t}} = u_0 \frac{d\bar{y}}{d\bar{t}}$$

$$\frac{d^2x}{dt^2} = u_0 \frac{d^2\bar{x}}{d\bar{t}^2} \cdot \frac{d\bar{t}}{dt} = \frac{2u_0^2}{d_f} \frac{d^2\bar{x}}{d\bar{t}^2} \quad \frac{d^2y}{dt^2} = u_0 \frac{d^2\bar{y}}{d\bar{t}^2} \cdot \frac{d\bar{t}}{dt} = \frac{2u_0^2}{d_f} \frac{d^2\bar{y}}{d\bar{t}^2}$$

Thus, equation (C.1.3) and (C.1.4) becomes

$$2\psi_{I-1} \frac{d^2\bar{x}}{d\bar{t}^2} + \frac{d\bar{x}}{d\bar{t}} - \bar{v}_x = 0 \quad (C.1.5)$$

$$2\psi_{I-1} \frac{d^2\bar{y}}{d\bar{t}^2} + \frac{d\bar{y}}{d\bar{t}} - \bar{v}_y + 2\psi_{I-2}\bar{a}_c = 0 \quad (C.1.6)$$

Where

$$\psi_{I-1} = \frac{\rho_g d_p^2 U_0}{18\mu_g d_f} \quad \text{and} \quad \psi_{I-2} = \frac{(\rho_l - \rho_g) d_p^2 U_0}{18\mu_g d_f}$$

Ranz and Wong (1952) used the following flow field approximation:

$$\left. \begin{array}{l} \bar{v}_x = -\bar{x} \\ \bar{v}_y = \bar{y} \end{array} \right\} \text{for region } \left\{ \begin{array}{l} -1 < \bar{x} < 0 \\ -1 < \bar{y} < 1 \end{array} \right.$$

With this flow field approximation, the equation becomes

$$2\psi_{I-1} \frac{d^2\bar{x}}{d\bar{t}^2} + \frac{d\bar{x}}{d\bar{t}} + \bar{x} = 0 \quad (C.1.7)$$

$$2\psi_{I-1} \frac{d^2\bar{y}}{d\bar{t}^2} + \frac{d\bar{y}}{d\bar{t}} - \bar{y} = -2\psi_{I-2}\bar{a}_c \quad (C.1.8)$$

And the initial conditions are, at $t = 0$

$$x = -1 \quad (C.1.9)$$

$$\bar{u}_x = 1$$

$$\bar{u}_y = 0$$

Since there is only one initial condition for the y-equation solution to the x-equation is used as boundary condition for the y-equation. Here the x-equation is a linear differential equation with constant coefficients, and can be written in a general form as follows:

$$mp'' + cp' + kp = 0 \quad (\text{C.1.10})$$

The form of the solution for equation (C.1.10) depends on the following relationships

Case I: $4mk < 1$ Distinct real roots

Case II: $4mk = 1$ A real double root

Case III: $4mk > 1$ Complex conjugate roots

The coefficients in the x-equation are

$$m = 2\psi_{I-1}, \quad c = 1, \quad k = 1$$

Thus

$$8\psi_{I-1} \begin{cases} > 1 \text{ for } \psi_{I-1} > 1/8 \\ = 1 \text{ for } \psi_{I-1} = 1/8 \\ < 1 \text{ for } \psi_{I-1} < 1/8 \end{cases}$$

The minimum value of ψ_{I-1} for finite impaction efficiencies can be taken as the theoretical value of 1/8 (Ranz & Wong, 1952). It is thus the case where $\psi_{I-1} > 1/8$ with complex conjugate roots that applies the x-equation. These roots are given by Kreyszig (2006) as

$$\lambda_{1,2} = -\alpha \pm i\gamma$$

Where

$$\alpha = \frac{c}{2m}, \quad \gamma = \frac{1}{2m} \sqrt{4mk - c^2}$$

And the general solution is

$$\bar{x}(t) = \exp^{-\alpha t} (A \cos \gamma t + B \sin \gamma t) \quad (\text{C.1.11})$$

Using the initial conditions

$$\bar{x}(\bar{t}) = \exp^{-\alpha \bar{t}} (A \cos \gamma \bar{t} + B \sin \gamma \bar{t}) \Big|_{\bar{t}=0} = -1$$

$$\rightarrow A = -1$$

$$\bar{x}(\bar{t}) = -\alpha \exp^{-\alpha \bar{t}} (A \cos \gamma \bar{t} + B \sin \gamma \bar{t}) + \exp^{-\alpha \bar{t}} (-A\gamma \cos \gamma \bar{t} + B\gamma \sin \gamma \bar{t}) \Big|_{\bar{t}=0} =$$

$$\rightarrow -\alpha A + B\gamma = 1$$

Solving for A and B

$$A = -1, \quad B = \frac{1 - \alpha}{\gamma}$$

Inserting this into equation (C.1.11)

$$\bar{x}(\bar{t}) = \exp^{-\alpha\bar{t}} \left(-\cos \gamma t + \frac{1-\alpha}{\gamma} \sin \gamma t \right) \quad (\text{C.1.12})$$

The goal is to find the trajectory that gives us the capture efficiency. Solving equation (C.1.12) for $\bar{x}(\bar{t}') = 0$ gives a boundary condition for the y-equation. The capture efficiency is then the initial condition for y-equation that gives the trajectory through $\bar{x} = 0, \bar{y} = 1$

$$\begin{aligned} \left(\frac{1-\alpha}{\gamma} \right) \sin \gamma \bar{t}' - \cos \gamma \bar{t}' &= 0 \\ \left(\frac{1-\alpha}{\gamma} \right) \tan \gamma \bar{t}' &= 1 \\ \bar{t}' &= \frac{1}{\gamma} \tan^{-1} \left(\frac{\gamma}{1-\alpha} \right) \\ \bar{t}' &= \frac{1}{\frac{1}{4\psi_{l-1}} \sqrt{8\psi_{l-1}}} \tan^{-1} \left(\frac{\frac{1}{4\psi_{l-1}} \sqrt{8\psi_{l-1}}}{1 - \frac{1}{4\psi_{l-1}}} \right) \\ \bar{t}' &= \frac{1}{\sqrt{\left(\frac{1}{2\psi_{l-1}} \right) - \left(\frac{1}{4\psi_{l-1}} \right)^2}} \tan^{-1} \left(\frac{\sqrt{\left(\frac{1}{2\psi_{l-1}} \right) - \left(\frac{1}{4\psi_{l-1}} \right)^2}}{1 - \frac{1}{4\psi_{l-1}}} \right) \end{aligned} \quad (\text{C.1.13})$$

Thus a boundary condition to solve the y-equation is obtained. The y-equation is non-homogenous and its solution is the sum of the homogenous part and a particular solution

$$\bar{y} = \bar{y}^{(h)} + \bar{y}^{(p)} \quad (\text{C.1.14})$$

The homogenous part of y-equation is

$$\bar{y}^{(h)}: \quad 2\psi_{l-1} \frac{d^2 \bar{y}}{d\bar{t}^2} + \frac{d\bar{y}}{d\bar{t}} - \bar{y} = 0 \quad (\text{C.1.15})$$

And the coefficients in equation (C.1.15) are

$$m = 2\psi_{l-1}, \quad c = 1, \quad k = -1$$

Thus

$$8\psi_{I-1} \begin{cases} < 1 \text{ for } \psi_{I-1} > 1/8 \\ = 1 \text{ for } \psi_{I-1} = 1/8 \\ > 1 \text{ for } \psi_{I-1} < 1/8 \end{cases}$$

Here Case I with distinct real roots applies:

$$\lambda_{1,2} = -\alpha \pm \beta$$

Where

$$\alpha = \frac{c}{2m}, \quad \beta = \frac{1}{2m} \sqrt{c^2 - 4mk}$$

Thus the homogenous solution is of the form

$$\bar{y}^{(h)}(\bar{t}) = C_1 e^{\lambda_1 \bar{t}} + C_2 e^{\lambda_2 \bar{t}} \quad (\text{C.1.16})$$

The particular solution is just a constant ($-2\psi_{I-2}\bar{a}_c$), and from Kreyszig(2006) we know that it has the solution in the form

$$\bar{y}^{(p)}(\bar{t}) = K_1 = -2\psi_{I-2}\bar{a}_c \quad (\text{C.1.17})$$

Thus the general solution is

$$\bar{y}(\bar{t}) = C_1 e^{\lambda_1 \bar{t}} + C_2 e^{\lambda_2 \bar{t}} - 2\psi_{I-2}\bar{a}_c \quad (\text{C.1.18})$$

Using the initial condition from equation (C.1.9) and the boundary condition from equation (C.1.13)

$$\bar{y}^{(h)}(\bar{t}) = C_1 e^{\lambda_1 \bar{t}} + C_2 e^{\lambda_2 \bar{t}} + 2\psi_{I-2}\bar{a}_c \Big|_{\bar{t}=\bar{t}'} = 1 \rightarrow C_1 e^{\lambda_1 \bar{t}'} + C_2 e^{\lambda_2 \bar{t}'} = 1 - 2\psi_{I-2}\bar{a}_c$$

$$\bar{y}^{(h)'}(\bar{t}) = C_1 \lambda_1 e^{\lambda_1 \bar{t}} + C_2 \lambda_2 e^{\lambda_2 \bar{t}} \Big|_{\bar{t}=0} = 1 \rightarrow C_1 \lambda_1 + C_2 \lambda_2 = 0$$

Solving for C_1 and C_2

$$C_1 = -\frac{\lambda_2}{\lambda_1} \frac{1-2\psi_{I-2}\bar{a}_c}{\exp(\lambda_2 \bar{t}') - \frac{\lambda_2}{\lambda_1} \exp(\lambda_1 \bar{t}')} , \quad C_2 = \frac{1-2\psi_{I-2}\bar{a}_c}{\exp(\lambda_2 \bar{t}') - \frac{\lambda_2}{\lambda_1} \exp(\lambda_1 \bar{t}')}$$

Inserting this into equation (C.1.18) gives

$$\begin{aligned}\bar{y}(\bar{t}) &= -\frac{\lambda_2}{\lambda_1} \frac{1 - 2\psi_{I-2}\bar{a}_c}{\exp(\lambda_2\bar{t}') - \frac{\lambda_2}{\lambda_1}\exp(\lambda_1\bar{t}')} e^{\lambda_1\bar{t}} + \frac{1 - 2\psi_{I-2}\bar{a}_c}{\exp(\lambda_2\bar{t}') - \frac{\lambda_2}{\lambda_1}\exp(\lambda_1\bar{t}')} e^{\lambda_2\bar{t}} \\ &\quad - 2\psi_{I-2}\bar{a}_c \\ \bar{y}(\bar{t}) &= \frac{1 - 2\psi_{I-2}\bar{a}_c}{\exp(\lambda_2\bar{t}') - \frac{\lambda_2}{\lambda_1}\exp(\lambda_1\bar{t}')} \left(\exp(\lambda_2\bar{t}) - \frac{\lambda_2}{\lambda_1}\exp(\lambda_1\bar{t}) \right) \\ &\quad - 2\psi_{I-2}\bar{a}_c\end{aligned}\quad (C.1.19)$$

The capture efficiency can be found by letting \bar{t}' in equation (C.1.19) be 0

$$\bar{y}(0) = \frac{(1 - 2\psi_{I-2}\bar{a}_c) \left(1 - \frac{\lambda_2}{\lambda_1}\right) - 2\psi_{I-2}\bar{a}_c \left(\exp(\lambda_2\bar{t}') - \frac{\lambda_2}{\lambda_1}\exp(\lambda_1\bar{t}')\right)}{\exp(\lambda_2\bar{t}') - \frac{\lambda_2}{\lambda_1}\exp(\lambda_1\bar{t}')} \quad (C.1.20)$$

With some rearrangement and the following expression for the capture efficiency is obtained

$$\begin{aligned}\eta_{I-c} &= \frac{\lambda_2 - \lambda_1 + 2\bar{a}_c\psi_{I-2}\lambda_1 - 2\bar{a}_c\psi_{I-2}\lambda_2 + 2\bar{a}_c\psi_{I-2}\lambda_2 \exp(\lambda_1 t') - 2\bar{a}_c\psi_{I-2}\lambda_1 \exp(\lambda_2 t')}{\lambda_2 \exp(\lambda_1 t') - \lambda_1 \exp(\lambda_2 t')} \quad (C.1.21)\end{aligned}$$

Where

$$\begin{aligned}\lambda_{1,2} &= -(1/4\psi_{I-1}) \pm \sqrt{(1/4\psi_{I-1})^2 + (1/2\psi_{I-1})} \\ \bar{t}' &= \frac{1}{\sqrt{\left(\frac{1}{2\psi_{I-1}}\right) - \left(\frac{1}{4\psi_{I-1}}\right)^2}} \tan^{-1} \left(\frac{\sqrt{\left(\frac{1}{2\psi_{I-1}}\right) - \left(\frac{1}{4\psi_{I-1}}\right)^2}}{1 - \frac{1}{4\psi_{I-1}}}\right)\end{aligned}$$

Bibliography

- Amistco. (2004). *Mesh and Vane Eliminators*. Retrieved December 3, 2011, from Amistco.com: http://www.amistco.com/PRODUCTS/ELIMINATORS/msh_vne.html
- Brouwers. (2012). *prof. dr ir J.J.H (Bert) Brouwers*. Retrieved April 26, 2012, from TU/e: <http://www.wtb.tue.nl/woc/ptc/brouwers/highlights.html>
- Brouwers, J. (1997). Particle collection efficiency of the rotational particle separator. *PowderTechnology* 92, 89-99.
- Coalessense. (2011). *CLSR datasheet*. Retrieved April 26, 2012, from Coalessense: <http://www.coalessense.com/documenten/CLSR%20datasheet%20okt%202011.pdf>
- ERG Aerospace. (2011). *ERG Duocel® - Foam Surface Area*. Retrieved March 23, 2012, from ERG Duocel®: <http://www.ergaerospace.com/surface-area.html>
- Eur. Patent 0286160. (1988, October 12). *Rotational particle separator*. Retrieved February 20, 2012, from Ip.com - Intellectual property library: <http://ip.com/patapp/EP0286160A1>
- Fredheim, A. (2011). Equipment in gas processing. In D. o. EPT, *Industrial Process and Energy Technology* (p. Part II). Trondheim: Norwegian University of Science and Technology.
- Førde, M., & Nørstrud, H. (1984). On frictional pressure gradient in annular flow. *International journal multiphase flow* vol. 10, 115-119.
- GPSA, G. P. (2004). *Engineering Data Book*. Tulsa.
- Helsør, T. (2006). *Experimental Characterization of Wire Mesh Demisters*. Trondheim: Doktoravhandling ved NTNU.
- Hewitt, G. F., & Whalley, P. B. (1989). *Multiphase Science and Technology*. Oxford: University of Oxford.
- Holdich, R. (2002). *Fundamentals of particle technology*. Loughborough: Midland Information Technology & Publishing.
- Ishii, M., & Grolmes, M. A. (1975). *Inception criteria for droplet entrainment in two-phase concurrent film flow*. Argonne, Illinois: AIChE Journal, 21: 308–318. doi: 10.1002/aic.690210212.
- Lage, J. L. (1998). The fundamental theory of flow through permeable media from darcy to turbulence. In D. B. Ingham, & I. Pop, *TRanport phenomena in porous media* (pp. 1-30). Dallas: Elsevier Science Ltd.

- Lage, J. L., & Merrikh, A. A. (2005). From continuum to porous-continuum: The visual resolution impact on modeling natural convection in heterogeneous media. In D. B. Ingham, & I. Pop, *Transport phenomena in porous media ed. 3* (pp. 60-96). Dalla: Elvisier.
- Medici, M. (1974). *The Natural Gas Industry*. London: Butterworth & Co.
- Mondt, E. (2005). *Compact Centrifugal Separator of Dispersed Phases*. Eindhoven: Eindhoven University Press.
- Ranz, W. E., & Wong, J. B. (1952). Impaction of Dust and Smoke Particles on Surface and Body Collectors. *Industrial and Engineering Chemistry*, 1371-1381.
- Schlumberger. (2011). *Oilfield glossary*. Retrieved February 2, 2012, from Schlumberger: <http://www.glossary.oilfield.slb.com/default.cfm>
- Straub, D. J., & Collett Jr., J. L. (2004). *Straub, Derek J*. Colorado: Straub, Derek J.
- Sulzer. (2011). Retrieved December 3, 2011, from http://www.sulzerchemtech.com/portaldata/11/Resources//brochures/mtt/Gas_Liquid_Separation_Technology.pdf
- Swanborn, R. (1988). *A new approach to the design of gas-liquid separators for the oil industry*. Delft: Technische Universiteit Delft.
- Twister BV. (2012). *Twister® Supersonic Separator - Twister BV*. Retrieved February 20, 2012, from Twister BV - Breaking Barriers in Gas Processing: <http://twisterbv.com/products-services/twister-supersonic-separator/>
- van Wissen, R. J. (2006). *Centrifugal separation for cleaning well gas streams: from concept to prototype*. Eindhoven: Eindhoven University Press.
- White, F. M. (2007). *Fluid Mechanics*. Rhode Island: McGraw-Hill.